# Resistive magnetohydrodynamic jets from protostellar accretion disks

Dissertation zur Erlangung des akademischen Grades
Doktor der Naturwissenschaften (Dr. rer. nat.)
in der Wissenschaftsdisziplin Astrophysik

eingereicht an der
Mathematisch–Naturwissenschaftlichen Fakultät
der Universität Potsdam

von

**Miljenko Čemeljić**

Potsdam, im Mai 2004

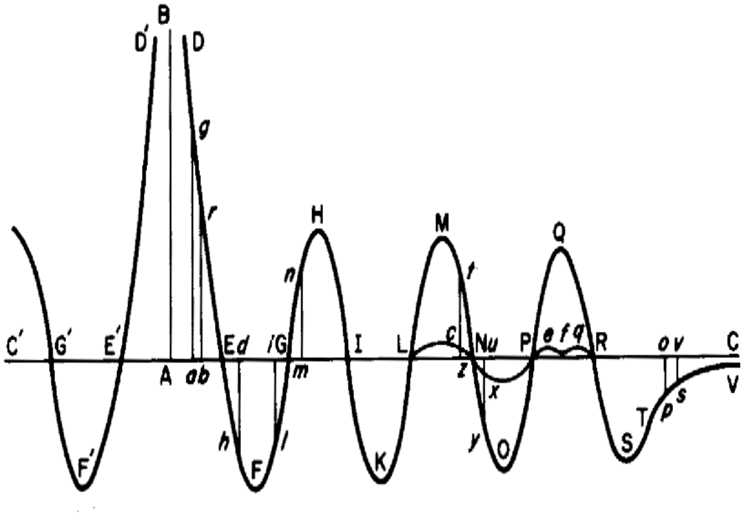

Bošković's curve from the book ”A Theory of Natural Philosophy”, Venice 1763, Roger Joseph Boscovich, S.J.

”Now the law of forces is of this kind; the forces are repulsive at very small distances, & become indefinitely greater & greater, as the distances are diminished indefinitely, in such a manner that they are capable of destroying any velocity, no matter how large it may be, with which one point may approach another, before ever the distance between them vanishes. When the distance between them is increased, they are diminished in such a way that at a certain distance, which is extremely small, the force becomes nothing. Then as the distance is still further increased, the forces are changed to attractive forces; these at first increase, then diminish, vanish, & become repulsive forces, which in the same way first increase, then diminish, vanish, & become once more attractive; & so on, in turn, for a very great number of distances, which are all still very minute: until, finally, when we get to comparatively great distances, they begin to be continually attractive & approximately inversely proportional to the squares of the distances. This holds good as the distances are increased indefinitely to any extent, or at any rate until we get to distances that are far greater than all the distances of the planets and comets [see Fig].”

# Contents

# Introduction

Astrophysical jets are extended and collimated energetic outflows of matter from various astronomical objects. The first naked eye observations of the object today associated with the protostellar jets were made at the end of XIX century by Burnham, who observed the nebula (today called *Burnham's nebula*) near the T Tauri star (Burnham 1890, 1894). After the works of G.H. Herbig (1950, 1951) and G. Haro (1952, 1953), Mundt (1985) recognized these objects as jet-like outflows. Stellar outflows, or more precisely *young stellar objects* (YSOs) jets are today considered essential for the stellar birth process.

On a much larger, galactic scale, an optical jet was discovered by H. Curtis in 1918 as a straight ray, connected with the nucleus of the giant elliptical galaxy M87 by a thin line of matter (Curtis 1918). Through to the early 1970's it remained the unique example, until a great number of radio-galaxies revealed the presence of the radio jets.

At the end of the XX century, with the development of observational methods, more systems were included into a class of jet sources. These are, in addition to the already mentioned young stellar objects (YSOs) and active galactic nuclei (AGN), high- and low-mass binaries (HMXBs and LMXBs) and black hole X-ray transients, all presumably associated with an accreting neutron star or a black hole. In these sources, the jets are rather sporadically observed, and not as a rule. Also, in some symbiotic systems (containing an accreting white dwarf), the presence of a jet is indicated after some recent discoveries (Bond & Livio 1990; Pollaco & Bell 1996), and Livio (1999) suggests the inclusion of the planetary nebulae jets into the class. In the 1990's the supersoft X-ray sources (SSS) were added to the list, as they are supposed to contain a white dwarf accreting the matter from a subgiant companion (Hasinger 1994; Kahabka & Trumper 1996).

Both observational techniques and theoretical modelling have considerably improved in the last few decades. Presently, we are able to test certain physical constraints of the models. The relative stationarity of the astrophysical jets makes it possible to compare the observed jets with the results of the analytical studies, which usually can be done only in a stationarity approximation.

One fact following from the observations is that, up to now, all the objects which exhibit jets are those for which an accreting central object, and therefore the accretion disk, is assumed. The presence of the magnetic field is also ubiquitous.

The paradigm arising from this observation that the formation of the jet requires the presence of an accretion disk will be investigated in this thesis.

A launching of the jet from the surface of a star, or the explanation of its high degree of collimation through oblique shocks, when the accretion process is not the main underlying machine (Canto et al. 1988; Frank & Mellema 1996) has the main disadvantage that, for the different classes of the objects, the models substantially differ. As the jet launching mechanisms are rather similar for the very different underlying objects, it is tempting to try to find some unifying scheme.

The unifying mechanism for collimation and acceleration of jets proposed in this thesis is the hydro-magnetic one, i.e. the jet is magnetically-driven. The numerical simulations have been performed within a non-relativistic scheme, with the ZEUS-3D code, and the results are relevant for the protostellar jets. However, to some extent, it is possible to also scale the conclusions to AGN jets.

This thesis is organised as follows. After the observational data and their implications for the models, in the second chapter a theoretical basis of resistive magnetohydrodynamics is given, and the ZEUS-3D magneto-hydrodynamics code introduced. In the third chapter we present stationary and time-dependent models from the literature and summarize important theoretical concepts. The numerical simulations of a jet formation with the initial and boundary conditions are presented in the final chapters. In the Summary the main results are collected, and their discussion outlined. In the Appendix, our tests for the resistive ZEUS-3D code are presented.

# Chapter 1

# Astrophysical outflows: The disk-jet paradigm

## 1.1 Protostellar jets

It is possible to follow a history of young stellar jets back to 1890, when Burnham (1890, 1894), through the Lick Observatory 90-cm refractor observed the faint nebula near the T Tauri star. This object later became known as Burnham's Nebula, and today it is assigned HH 255.

Half a century later, G.H. Herbig and G. Haro independently discovered curious "semi-stellar" objects in Orion constellation and described the basic properties of these objects (Herbig 1950, 1951; Haro 1952, 1953). Herbig (1951) noted the spectral similarity of these objects to Burnham's Nebula, with peculiar, strong emission lines of [S II] and [O II].

Ambartsumian (1954,1957), relying on the co-existence of these objects with nearby nebulous or emission-line stars, suggested that these objects (called *Herbig-Haro* or HH objects by him) are the early stages of young T Tauri stars. An enlargement of the plate published in Herbig (1951) is presented in Fig. 1.1.

In the next 25 years more than 40 Herbig-Haro objects were found and studied (Herbig 1974), but their nature and origin remained a mistery, until Schwartz (1975) suggested that the spectral properties of these objects might be a result of the shock-excited gas. The shock was supposed to be excited by supersonic wind from the young star. Together with the discussion of the possible shock mechanism, came the discovery of the high proper motions in HH objects, of the order of several hundreds km/s (Cudworth & Herbig 1979). The prototype HH-objects HH1 and HH2 appear to move in opposite directions, and one natural possibility was that they could move away from

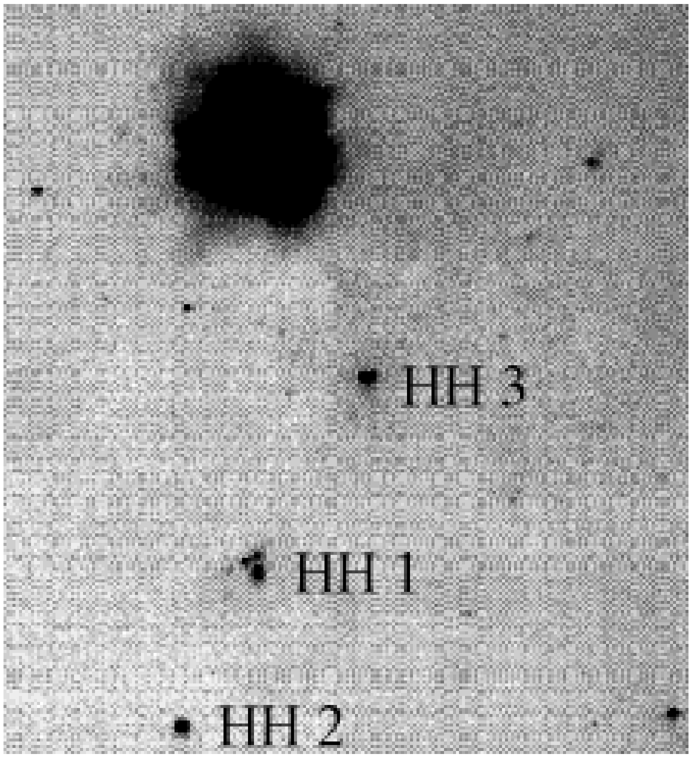

Figure 1.1: HH 1, 2 and 3 as seen in an enlargement of the plate published in Herbig (1951). HH 1, 2, and 3 are three star-like objects in line exactly below the biggest object, which is NGC 1999. The plate was taken in the blue spectral region with the Crossley reflector at Lick Observatory in Jan 20, 1947. Adopted from Reipurth & Heathcote (1997).

a common source (Herbig & Jones 1981). Today the accepted picture is what Dopita et al. (1982) concluded for the HH 46/47 system: HH objects result from bipolar, well collimated flows, "jets" from a young, embedded star. Images taken in the following years showed that HH objects are not independent objects, but shock fronts of the jets driven by young stellar objects (Mundt 1985).

In Mundt et al. (1987) the typical length of the HH jet was estimated to be 0.01 pc to 0.2 pc. Later, even longer jets were discovered (Poetzel et al. 1989; Martí et al. 1993; Ogura 1995) with lenghts of the order of few parsecs. Also, Bally & Devine (1994) and López et al. (1995) re-estimated the jet lenghts of HH34, HL Tau and HH30 to be of the order of few pc's. Measurements of the radial velocities also support this prolongation of the jet lenghts (see Eislöffel & Mundt 1997).

It turned out that multiple working surfaces are present in larger flows than was earlier thought to be associated with single jets (e.g. Stanke et al. 1999). This suggests that the jet feeding mechanism is nonsteady on the timescale of 1000 to 2000 years.

With the Hubble Space Telescope (HST) the direct observation of the dust disk around the source of the jet became possible. Currently, one of the best examples is that of HH30 which shows not only the edge-on seen dust disk, but also the motion of the ejecta, i.e. a sub-structure of the jet (see Fig. 1.2).

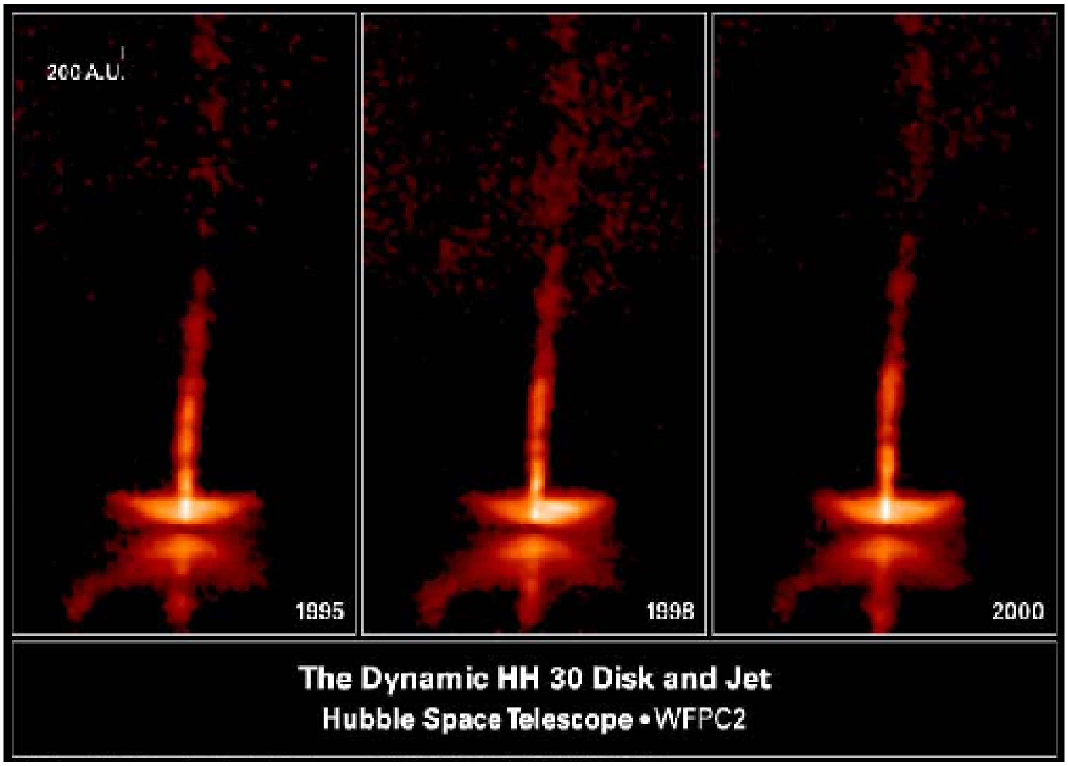

Figure 1.2: The pictures of HH30 taken between 1995 and 2000 with the Wide Field Planetary Camera 2, aboard HST. The dust disk diameter is 450 AU. The reflection nebulae above and below the equatorial plane of the disk are illuminated by the central star. The changing pattern of the shadows on the disk can be caused by bright spots on the star, or variations of the disk structure near the star. Credits: NASA, A. Watson, K. Stapelfeldt, J. Krist and C. Burrows.

That the jet origin is in the vicinity of the central object follows from one more observational fact: the protostellar jet emerges well collimated from the dust disk. A collimated jet is visible, e.g. in the case of DG Tau, at the distance of approximately 40 AU from a center of the dust disk (Kepner et al. 1993).

## 1.2 Jets in other astronomical objects

Collimated bipolar jets are also observed in other classes of astronomical objects and on different scales. In Table 1 are listed the classes and the supposed corresponding physical systems. Some of them are traditionally not connected with the jets. However, the criterion of inclusion is the existence of collimated outflows, not the ubiquitous appearance of the jets in these systems. The table is not very restrictive, a single (possible) observation of the jet was considered to be enough to include the corresponding objects.

Weakly collimated outflows are observed in many other objects as outbursts of novae, giant stars or post-asymptotic giant branch stars, but we will concentrate on the inves-

Table 1.1: Systems with collimated outflows. Adopted from Livio 1999.

| Object | | Physical system |
|---|---|---|
| Young stellar objects | S | Accreting young star |
| Massive X-ray binaries | T | Accreting neutron star or black hole |
| Black hole X-ray transients | E | Accreting black hole |
| Low mass X-ray binaries | L | Accreting neutron star |
| Symbiotic stars | L | Accreting white dwarf |
| Planetary nebulae nuclei | A | Accreting nucleus |
| Supersoft X-ray sources | R | Accreting white dwarf |
| Active galactic nuclei | EXTRAGALACTIC | Accreting supermassive black hole |

tigation of the objects which show *well* collimated *high velocity* outflows (the jets).

In Table 1, the objects such as AGN (see Fig. 1.3 for one example), YSOs, some HMXBs (e.g. SS 433 - Margon 1984; Cyg X-3 - Strom et al. 1989) and black hole X-ray transients are the “standard” jet-containing objects.

The planetary nebulae (PN) are usually not mentioned in a jet context, but after the direct observation of the jets in the planetary nebula K1-2 near a binary star VW Pyx (Bond & Livio 1990), and a bipolar proto-planetary nebula M1-92 (Trammell & Goodrich 1996), it became possible to include the planetary nebulae in such a table. Also, some planetary nebulae seem to be directly connected to the precessing jets in the *point symmetric* PN (Livio & Pringle 1996).

Supersoft X-ray sources entered the list after the works of Pakull (1994), Crampton et al. (1996) and Southwell et al. (1996). In the case of LMXBs, there exists only one single observational detection of a jet up to now: Cir X-1 (Stewart et al. 1993), with the degree of collimation of the jet unknown. Similarly for the symbiotic systems, the jet is observed only in R Aqr (Burgarella & Paresce 1992).

All of the objects mentioned above are supposed to be the objects with an accretion disk, and the most important question about the astrophysical jets is then: Is the presence of the accretion disk required for the jet formation? More should be known about the mechanisms which can result in a jet, to answer this. If true, the model would apply for more than just explaining some exotic astronomical objects.

Another observational result is the terminal velocity of jets. This velocity is in *all* cases of the order of the escape velocity of the central object. For the protostellar jets it is a few hundreds of km/sec, and for the relativistic jets from accreting neutron stars or black holes it is higher than 0.9 $c$. The immediate conclusion following from this is that the inner part of the accretion disk is the origin of the jet.

Similar to YSOs jets, the relativistic jet emerges well collimated from the disk. For AGN, the VLBI results for the Virgo A (3C274) in M87 shows the origin of the jet is at 70 gravitational radii (Junor & Biretta, 1995). In the case of the microquasar (i.e. the

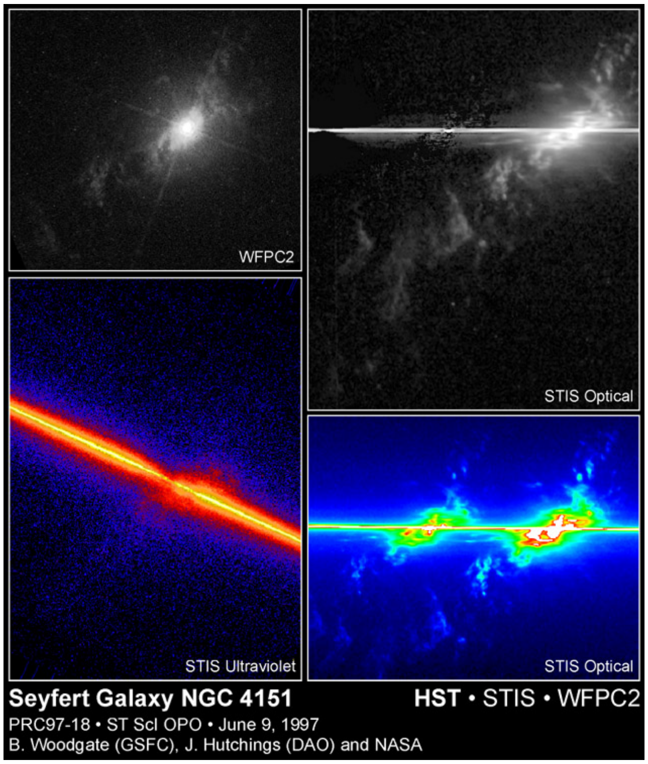

Figure 1.3: Seyfert galaxy NGC 4152. The Space Telescope Imaging Spectrograph (STIS) simultaneous records show the velocities of hundreds of gas knots streaming from the nucleus, which is thought to be a supermassive black hole. *Upper left* is a HST Wide Field Planetary Camera 2 image of the oxygen emission (5007 Å). There is no information about the motion of the oxygen gas. In STIS spectral image of the oxygen gas-*upper right*- the velocities of the knots are determined by comparing the knots of gas in the stationary image to the horizontal location of the knots. *Lower left* image is the velocity distribution of the carbon emission, which requires more energy to glow than for ionization of the oxygen gas, and is therefore probably closer to the energy source. In the *lower right* image, which is the false color image of the two emission lines of oxygen gas 4959 and 5007 Å), the line passing through the image originates probably from the powerful black hole in the center.

black hole X-ray transient, in present opinion) GRS 1915+105, the multiwavelength observations have demonstrated a correlation between the X-ray and IR flares, suggesting that the cause for the X-ray triggering and IR peaks is the same (Fender et al. 1997; Pooley & Fender 1997; Greiner et al. 1996; Eikenberry et al. 1998).

If it shows to be persistent, one observational fact (or rather one non-detection), can provide some clue to the jet formation mechanism: the cataclysmic variables (CVs) does not show the jets. Taking into account that they involve accretion disk, as SSSs and the symbiotic stars, the difference in a jet forming conditions could provide some constraints on the theoretical models (Livio 1997).

## 1.3 Jet formation - a magnetohydrodynamical process

Model in which the jet is launched from the disk-jet system, with a dipolar magnetic field of a central star, is similar to the well investigated solar wind. Except for the correlation between the disk mass and outflow energetics (Cabrit et al. 1990), it is supported mostly because of the theoretical reasons (see e.g. Küker et al. 2003). However, before the measurements of the magnetic field are available, it can be also convincingly criticized (Safier 1998, 1999).

High degrees of collimation and large velocity of the jets can so far simultaneously be explained only within the MHD model (e.g. Blandford 1993; Königl & Ruden 1993, Ray et al. 1997).

The direct evidence for the importance of the magnetic field for the acceleration is available only for extragalactic jets. Polarized synchrotron emission at radio wavelengths in radio galaxies, and in the optical band (for M87) do not have equally significant counterpart in the stellar jets.

The jet is, therefore, understood as a stream of plasma accelerated and collimated by magnetic forces. Origin of the ejected matter is the immediate vicinity of the central object, which includes an accretion disk.

The theoretical explanations of the jet formation can be divided into three classes:

**I)** Hydrodynamic models, where the collimation can be achieved by De Laval nozzle (Blandford & Rees 1974), by vortices around a black hole (Lynden-Bell 1978), or by self-similar thick disks (Gilham 1981; Narayan & Yi 1995).

**II)** Wind models, where the local magnetic field of the rotating source collimates the outflow (Mestel 1968; Blandford & Znajek 1977; Sakurai 1985; Li et al. 2001).

**III)** Models where the outflow is collimated by a *disk* magnetic field, being or large-scale magnetic field advected inwards from interstellar/intergalactic space (Lovelace 1976; Blandord & Payne 1982, hereafter BP82; Uchida & Shibata 1985; Bell & Lucek 1995; Ouyed & Pudritz 1997a, hereafter OP97) or the field produced locally in the disk (or in the central object) by some dynamo process (Tout & Pringle 1996).

A well established fact is that in the case of YSOs such powerful bipolar outflows as are jets, could not be thermally or radiation pressure driven winds (DeCampli 1981; Königl 1986). The reason is that the observed fluxes exceed those which the protostar could provide.

The acceleration and collimation of the initial disk (or stellar) wind is then assumed to be a result of the magnetic field. Two such models were investigated.

### Winds that originate at the surface of the disk

The BP82 model of the centrifugally driven wind, and the Uchida & Shibata (1985) model with the "uncoiling spring" are models developed in this approach.

BP82 model requires that the magnetic field lines thread the disk at an angle of 30° or more with respect to the jet axis, for the matter to be centrifugally ejected from the surface of the underlying Keplerian disk (see §3.1.1 here).

In the latter model the twisting of a large-scale magnetic field, because of the rotation of a radially collapsing non-Keplerian accretion disk, relaxes through the emission of the torsional Alfvén waves that propagate in both directions along the magnetic field lines. Matter is then transported to the surface of the disk, from where it is being ejected in the bipolar outflows.

### The X-wind model

In the X-wind model (Shu et al. 1994), a partial opening of the magnetosphere connecting the central star and the accretion disk is assumed. The corrotation point of the disk and the central magnetized star is the origin of the outflow. Magneto-centifugally driven winds from the inner edge of the disk extract the excess angular momentum along the open magnetic field lines. Such mechanism could be plausible in the case of YSOs, but fail in the case of accreting black holes.

## 1.4 Magnetic driven outflows

The observed correlation between the disk mass and outflow energetics supports the disk wind scenario (Cabrit & André 1991; Edwards et al. 1993). Its main advantage is the generality: detailed nature of the central object is not essential for the description of the physics of the outflow.

Self-similar models following BP82 approach (Königl 1989; Wardle & Königl 1993; Li 1995; Ferreira 1997) resulted in the consensus that it is possible to describe a jet launching from the accreting disk in a pure magnetic scheme. The result by Ferreira (1997) was the jet in smooth transition from a resistive disk, with the Lorentz force lifting the gas vertically.

Time-dependent MHD simulations of the jet formation were undertaken in two ways.

### Accretion disk as a boundary condition only

In the scheme with the accretion disk as a boundary condition it is possible to obtain numerically stable, long-lasting solutions, but it is intrinsically incomplete. The jet formation *must* include the process of accretion in a disk, as the accreted matter should feed the jet. However, evolution of the disk together with the jet is numerically difficult, because of the different characteristic time-scales involved.

The first simulations of the jet with the rotating accretion disk taken as a boundary condition have been done with the softened gravitational potential and non-equilibrium initial conditions (Ustyugova et al. 1995; Romanova et al. 1997). The simulations resulted in collimated, non-stationary outflows.

In OP97 simulations, where they studied a disk corona initially in hydrostatic equilibrium and pressure balance with the underlying disk (given as a boundary condition only), a stationary collimated flow emerged after 400 rotations of the inner disk boundary.

In Krasnopolsky et al. (1999) the steady state of the outflow is also reached. The disk boundary condition in their simulations included a thin, axial jet from the region near the origin, to limit the influence of the prescribed mass inflow from the disk surface on the forming outflow.

After these ideal-MHD simulations, a further step towards the inclusion of the disk in the simulations was to perform the *resistive* MHD computations following the OP97 setup (Fendt & Čemeljić 2002). The motivation was that the Alfvén waves from the highly turbulent accretion disk are expected to propagate into the disk corona. Therefore, these waves would provide the perturbations for some degree of turbulent motion also in the jet.

There exists an alternative approach, concerning the mechanism of jet collimation. Spruit et al. (1997) argue that the role of the toroidal magnetic field in the jet collimation cannot be crucial. Instead, the poloidal magnetic field of the disk is considered, and the collimation depends on the ratio of the outer to inner disk radius. In Chapter 5 we present our simulations in this approach, with the disk given as a boundary condition only. Here we only note that the jet collimation and acceleration by sole poloidal magnetic field showed to be possible if there exists some additional source of the energy in a system.

### Simulations of the disk+jet system

In Uchida & Shibata (1985), Shibata & Uchida (1985, 1986), Stone & Norman (1994a), Hayashi et al. (1996), Goodson et al. (1997), authors in general confirm that action of the Lorentz force ejects the material from the disk surface. A sub-Keplerian disk rotation may result as an outcome of the magnetic braking, because of the back-reaction of the magnetic field on the disk.

The interaction of a stellar (dipole) magnetosphere and the disk structure was investigated in simulations by Miler & Stone (1997), which carried out 2D *resistive* MHD simulations of protostellar jets.

However, such simulations could be performed only up to a few tens of the Keplerian rotations at the innermost radius of the disk, because of the numerical reasons and approximations of the ideal MHD, or the resistivity being assumed uniform in the computations. Only with imposing the initial and boundary conditions which omitted the rebounding of the accretted matter on the boundary (Casse & Keppens 2002), the longer simulations became possible. Our simulations in Chapter 6 here follow a similar idea.

## 1.5 Origin of magnetic field

The magnetic field in the vicinity of YSOs is of the order of kG (André et al. 1991). In the case of AGN, it is of the order of mG (Ferrari et al. 1997) in the developed jet, and close to the source, which is supposed to be the accretion disk around a supermassive black hole, it might be a few kG at the disk surface (Camenzind 1990).

For the sources, which include a neutron star or stellar mass black hole, the magnetic fields are very large, up to $10^{13}$ Gauss, and the field strength in the eventual accretion disk or the jet itself is still not known.

In the hydro-magnetic models of the jet acceleration and collimation, some large scale magnetic field is assumed to thread the disk. Which is the origin of this magnetic field? It could be an already existing (large scale) magnetic field, or one produced locally.

### 1.5.1 External field

For the case when the magnetic field is advected inwards from the interstellar (intergalactic) space, the existence of a strong poloidal component of the magnetic field is supposed. This field is twisted by the rotation of the disk, which becomes slower because of the resulting torque. The jet is a kind of by-product of the twist. It removes the excess angular momentum from the system. The problem with this picture is that the origin of the poloidal field is not clear. In the case of YSOs it might be a preexisting interstellar magnetic field, amplified during the accretion in the collapsing molecular cloud. In the case of AGN, the inner region of the disk is fully ionized and, because of the differential rotation of the disk, the toroidal, and not the poloidal component, is amplified. In both cases, the accreting matter in the disk advects the field inwards from the interstellar (intergalactic) space (BP82, Pudritz & Norman 1983; Lovelace et al. 1986, Königl 1989).

### 1.5.2 Field produced locally

Here, some dynamo process is evoked in the accretion disk or in the central object (Tout & Pringle 1996; von Rekowski et al. 2000). The feedback of the induced magnetic field on the matter limits the field strength. Locally, Keplerian shear flows are linearly stable (Stewart 1975), but magnetic onset of the turbulence is possible even with a linear MHD instability (Balbus & Hawley 1991). The dynamo is supported by the motions resulting from the instability. Naturally, the nonlinear instabilities could take place, too.

Even if the field is generated locally, the origin of the field on the length scale of order of the disk radius is unknown. The field strengths generated by the eventual dynamo are proportional to the height of the disk (Hawley et al. 1995; Matsumoto & Tajima, 1995).

## 1.6 Jet propagation

The theory of optical emission from HH objects via the heating and excitation mechanism was introduced by McKee & Hollenbach (1980). They explained the shocks by a sudden change of density, pressure, temperature, velocity and a number of other quantities in a gas. Behind a shock, the gas cools and its density continues to increase.

When it became clear that most of the Herbig-Haro objects were not independent objects, but rather shock fronts of the well collimated jets driven by YSOs (Mundt 1985; Mundt et al. 1987), the extent of such jets, reaching a parsec scale, showed to be enormous. Furthermore: the leading surfaces of some jets, thought to be the terminating surfaces of the outflows, showed not to be the ultimate ones. They are encountering the gas which is already fast moving away from the driving source of the jet, i.e. the flows are much longer than visible at the time (Heathcote & Reipurth 1992; Morse et al. 1992, 1994). Recent observations show that many HH flows extend over several parsecs (Bally & Devine 1994; Eislöffel & Mundt 1997; Reipurth et al. 1997; Stanke et al. 1999).

The existence of the series of internal working surfaces in the flow leads to the conclusion that the ejection of matter into the jet is nonsteady. When this substructure in the jet is intense in the region between the origin and the terminating jet lobe, it is referred to as “knots”. Interesting is to note that the timescale of these ejections is of the order of 1000 years, and therefore could be related to events similar to the episodic strong accretion phase of FU Orionis, where the outbursts take place (Dopita 1978; Reipurth & Heathcote 1992).

The interaction of a stellar wind and the surrounding medium (*working surface*) results in two shocks:

**i)** The ambient shock - A shock in which the ambient medium is accelerated to the

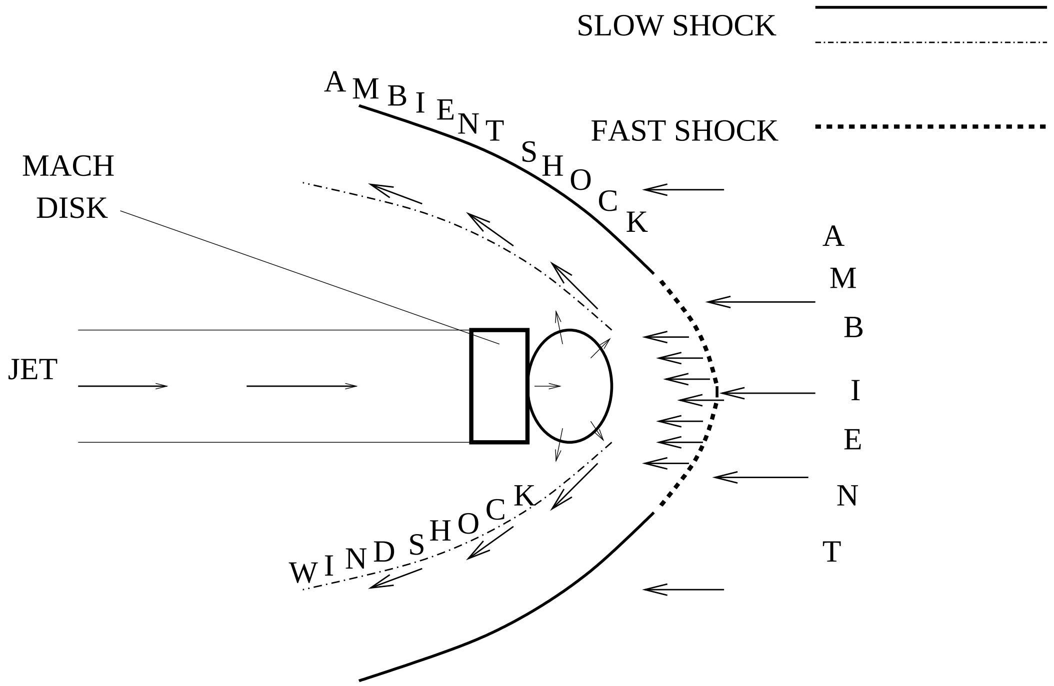

Figure 1.4: The bow shock working surface. A layer of dense gas between the leading part of the bow shock and the Mach disk interacts with the ambient gas and forms the sideways parts of the bow shock.

propagation speed of the interaction region.

**ii)** The inner shock (the *Mach disk*) - Here the material in the flow is decelerated to the speed of the interaction region.

Between these two shocks, a layer of dense gas is located (Hollenbach 1997). This gas can be subject to fragmentation into clumps and filaments (Blondin et al. 1989; Stone & Norman 1994a; Suttner et al. 1997), which could be an explanation for the “knotty” structure of the jets.

One special case of the shock is frequently called a *bow shock* (Blandford & Rees 1974; Norman et al. 1982; Hollenbach 1997; Raga et al. 1998). It explains the shape and width of emission lines, the spatial distribution of emission in different lines, and the position–velocity diagrams. In a bow shock the head of the jet is surrounded by an envelope similar to a rotation paraboloid (Fig. 1.4). It is formed by the material expelled sidewards of the region between the Mach disk and leading shock.

# Chapter 2

# Theoretical conjecture

From the observations it is possible to conclude that the astrophysical jets are magnetically driven (e.g. Mundt et al.1990; Mirabel & Rodriguez 1995; Ray et al. 1996). Thus, in order to model the jet formation process we need to solve the MHD equations under astrophysical boundary conditions (BP82; Pudritz & Norman 1983; Sakurai 1985; Uchida & Shibata 1985; Lovelace et al. 1986, 1991; Shu et al. 1994). In the following sections given is a brief introduction to the MHD theory and the MHD code ZEUS-3D, which we used for the numerical simulations.

## 2.1 Resistive magnetohydrodynamics

The MHD equations are a combination of the hydrodynamic equations, Maxwell's equations and the thermodynamic equation of state. We will consider the non-relativistic approximation. The equations are written in the cgs system of units, $c$ in the equations is the speed of light.

The hydrodynamic equations are the (mass) continuity equation,

$$\frac{\partial \rho}{\partial t} + \nabla \cdot (\rho \boldsymbol{u}) = 0 \tag{2.1}$$

and the force equation (the equation of motion),

$$\rho \frac{\partial \boldsymbol{u}}{\partial t} + \rho (\boldsymbol{u} \cdot \nabla) \boldsymbol{u} = -\nabla p - \rho \nabla \Phi + \frac{1}{c} (\boldsymbol{j} \times \boldsymbol{B}) + \boldsymbol{F}_{\nu} \, . \tag{2.2}$$

Here, $\rho$ is the mass density, $\boldsymbol{u}$ is the velocity, $p$ is the hydrodynamic pressure, $\Phi$ is the gravitational potential, $\boldsymbol{B}$ is the magnetic induction, and $\boldsymbol{F}_{\nu}$ is the viscous force. In our work we do not consider viscous fluid, so the last term will be ommited further.

The electric current density $\boldsymbol{j}$ is given by Ampère's law,

$$\boldsymbol{j} = \frac{c}{4\pi} \nabla \times \boldsymbol{B} \, . \tag{2.3}$$

Neglecting the displacement current, we can describe the electromagnetic fields by Ampère's law (2.3), Faraday's law,

$$\nabla \times \boldsymbol{E} + \frac{1}{c}\frac{\partial \boldsymbol{B}}{\partial t} = 0 \tag{2.4}$$

and the equation stating the non-existence of the magnetic monopoles

$$\nabla \cdot \boldsymbol{B} = 0\ . \tag{2.5}$$

The energy equation is

$$\rho\left[\frac{\partial e}{\partial t} + (\boldsymbol{u}\cdot\nabla)\, e\right] + p(\nabla\cdot\boldsymbol{u}) - \frac{c^2}{4\pi\sigma}\boldsymbol{j}^2 = 0\ , \tag{2.6}$$

where $e$ is the internal energy, and the last term is the Ohmic heating. The thermodynamic equation of state, i.e. the specification of the gas pressure, closes the set of MHD equations.

### 2.1.1 Ohm's law

In the magnetohydrodynamics, an approximated equation of Ohm's law is used for a low frequency perturbations and in appropriate length scale (when the thermal motions are much smaller than a characteristic length scale), and for the dense enough plasma:

$$\boldsymbol{j} = \sigma(\boldsymbol{E} + \frac{1}{c}\boldsymbol{u}\times\boldsymbol{B})\ . \tag{2.7}$$

A scalar function $\sigma$ is the electrical conductivity.

For the MHD driven jets, the jet can change the magnetic field through the reconnection or through the diffusion and advection of the magnetic field. The dynamical time scale for YSOs jets is $t_{\rm dyn}$=$10^4$-$10^5$ yr (Reipurth et al. 1997; Eislöffel & Mundt 1997). This means that even the slow diffusive processes could affect the jet propagation. In general, an assumption is that the magnetic field (which launched the jet) remains in the jet and travels with it.

In a moderately ionized plasma of YSOs jets (relativistic jets are more ionized, see Dopita et al. 2002), the ionization fractions are $\chi = n_{\rm ionized}/n_{\rm neutral}$=0.5-0.01 (Hartigan et al. 1994). These fractions decrease with a propagation of the plasma beyond the internal shocks. In the optically invisible part of the jet this ratio could be very low.

Otherwise, if the plasma is not fully ionized, also the ambipolar diffusion may rearrange the field. As the jets are very extended (in length) and narrow objects, the ambipolar diffusion could strongly affect the MHD equilibrium after the jet launching (Frank et al. 1999). For the dynamical time scale comparable with the ambipolar diffusion timescale, the magnetic forces could no longer confine the jet.

In Ferreira & Pelletier (1993) it is shown that, with a good accuracy, the ambipolar diffusion and viscosity can be described by an effective resistivity. Therefore, in our simulations we neglected viscous effects and worked with the magnetic resistivity.

### 2.1.2 Induction equation

Faraday's law, if we express the electric field $\boldsymbol{E}$ from Ohm's law, becomes,

$$\frac{\partial \boldsymbol{B}}{\partial t} = \nabla \times (\boldsymbol{u} \times \boldsymbol{B}) - \frac{c^2}{4\pi}\nabla \times (\frac{1}{\sigma}\nabla \times \boldsymbol{B}) \ . \tag{2.8}$$

We entered $\boldsymbol{j}$ from Ampère's law, Eq. (2.3). The obtained equation, describing evolution of the magnetic field, is often referred to as the "induction equation".

In the case of constant electrical conductivity $\sigma$, and introducing $c^2/(4\pi\sigma) \equiv \eta$, the induction equation becomes

$$\frac{\partial \boldsymbol{B}}{\partial t} = \nabla \times (\boldsymbol{u} \times \boldsymbol{B}) + \eta \nabla^2 \boldsymbol{B} \ . \tag{2.9}$$

The variable $\eta$ is called the *magnetic diffusivity*.

The ratio of the first to the second terms in the brackets is the *magnetic Reynolds number* $R_{\rm m} = UL/\eta$, where L and U are the typical length scale and velocity, respectively. This ratio describes the importance of the diffusive term for the evolution of the magnetic field. The astrophysical length scales are very large, implying also a large $R_{\rm m}$. For example, in a completely ionized hydrogen plasma the microscopic diffusivity is $\eta_\mu \sim r_{\rm e} c (u_{\rm th}/c)^{-3}$, where $r_{\rm e} = e^2/(m_{\rm e}c^2)$ is the classical electron radius, and $u_{\rm th} = \sqrt{k_{\rm B}T/m_{\rm e}}$ is the electron thermal speed.

In a typical protostellar case $T = 10^4$K, $U = 100$km/s, and $L = 100$ AU, the magnetic Reynolds number is $R_{\rm m} = U\,L/\eta_\mu \approx 10^{15}$. Similar is for the galactic jets and accretion disks. A microscopic diffusivity alone leads to nonsignificant magnetic Reynolds numbers in astrophysical applications.

For an infinite conductivity, (the *ideal* MHD assumption), we can neglect the diffusive part in the induction equation, which becomes,

$$\frac{\partial \boldsymbol{B}}{\partial t} = \nabla \times (\boldsymbol{u} \times \boldsymbol{B}) \ . \tag{2.10}$$

This equation describes the motion of magnetic field lines as coupled to the fluid motion. It is described as the "freezing in" of the magnetic field in a fluid.

### 2.1.3 Equation of motion

The magnetic force (the Lorentz force) in the equation of motion becomes

$$\frac{1}{c}\boldsymbol{j} \times \boldsymbol{B} = -\frac{1}{4\pi}\boldsymbol{B} \times (\nabla \times \boldsymbol{B}) \ .$$

This, as $\frac{1}{2}\nabla(\boldsymbol{B}\cdot\boldsymbol{B})$=$(\boldsymbol{B}\cdot\nabla)\boldsymbol{B} + \boldsymbol{B}\times(\nabla\times\boldsymbol{B})$, we can rewrite as

$$\begin{aligned}\frac{1}{c}\boldsymbol{j} \times \boldsymbol{B} &= -\frac{1}{4\pi}[\frac{1}{2}\nabla(\boldsymbol{B}\cdot\boldsymbol{B}) - (\boldsymbol{B}\cdot\nabla)\boldsymbol{B}] = \\ &= -\nabla\left(\frac{\boldsymbol{B}^2}{8\pi}\right) + \frac{1}{4\pi}(\boldsymbol{B}\cdot\nabla)\boldsymbol{B} \ . \end{aligned} \tag{2.11}$$

The magnetic force can be understood as consisting of a “magnetic hydrostatic pressure” $p_M = B^2/(8\pi)$ and an additional part which describes the tension due to the curved lines of force. The equation of motion becomes

$$\rho\frac{d\boldsymbol{u}}{dt} = -\nabla(p + p_M + \rho\Phi) + \frac{1}{4\pi}(\boldsymbol{B}\cdot\nabla)\boldsymbol{B}\ . \tag{2.12}$$

### 2.1.4 Turbulent magnetic diffusion

As discussed in §2.1.2, because of the large length scales, in all astrophysical applications the magnetic Reynolds number following from the microscopic magnetic diffusivity alone is very large. If there exists any magnetic diffusivity in astrophysical systems, it is most probably “anomalous”, described by *macroscopic* MHD instabilities, i.e. the turbulence.

The accretion disk is highly turbulent, and it seems natural to expect the turbulence is advected by the jet/wind high above the disk. The coronal magnetic loops are winded-up and the reconnection occurs (Miller & Stone 2000). Aditionally, an interaction with the surrounding medium increases the turbulence of the jet.

The anomalous magnetic turbulence results in a much smaller magnetic Reynolds number. The parametrization – the same way as in a Shakura-Sunyaev model in the case of a hydrodynamical viscosity – gives

$$\eta_T = \alpha_m U L\ ,\ (\alpha_M \leq 1)\ .$$

One choice for the characteristic velocity $U$ is the poloidal Alfvén speed, $u_A = B_p/\sqrt{4\pi\rho}$. With $\alpha_m = 0.1$ and for the unit typical velocity and length, we obtain $R_\mathrm{m} \approx 10$.

In the terms of the time scales, it is possible to define the local magnetic Reynolds number as the ratio of the diffusive and dynamical time scale, $R_\mathrm{m} = \tau_\mathrm{diff}/\tau_\mathrm{dyn}$. In the numerical simulations with numerical grid cells of the size $l$, $\tau_\mathrm{diff} \equiv min(l^2/\eta)$, and $\tau_\mathrm{dyn} \equiv min(l/u_A)$.

## 2.2 Conservation laws of stationary ideal MHD

The axisymmetry of the astrophysical jets on the big scales, and their relative stationarity, leads to the stationary MHD in theoretical considerations. We derived here some conservation laws for a *stationary* ($\partial/\partial t = 0$) and *axisymmetric* ($\partial/\partial\phi = 0$) case in cylindrical coordinates ($R$,$\phi$,$z$) with the unit vectors ($\boldsymbol{e}_\mathrm{R}, \boldsymbol{e}_\phi, \boldsymbol{e}_\mathrm{z}$). These laws will be referred to in the next chapters.

Lüst & Schlüter (1954), Chandrasekhar (1956) and Mestel (1961) provided the first derivations for the axisymmetric ideal MHD in the case of incompressible and non-viscous fluid.

The induction equation (2.8) is then simplified to

$$\nabla \times (\boldsymbol{u} \times \boldsymbol{B}) = 0\ . \tag{2.13}$$

There are two special directions in which vector fields can be decomposed: the *poloidal*, marked by the subscript p, which is the components in the meridional ($R$,$z$) plane; and the *toroidal*, marked by the subscript $\phi$, in the $\phi$ direction.

For a decomposed velocity and magnetic field: $\boldsymbol{u} = \boldsymbol{u}_\mathrm{p} + \boldsymbol{u}_\phi = \boldsymbol{u}_\mathrm{p} + \boldsymbol{\omega} \times \boldsymbol{R}$ and $\boldsymbol{B} = \boldsymbol{B}_\mathrm{p} + \boldsymbol{B}_\phi$. We can write, from the simplified induction equation:

$$\nabla \times [(\boldsymbol{u}_\mathrm{p} + \boldsymbol{u}_\phi) \times (\boldsymbol{B}_\mathrm{p} + \boldsymbol{B}_\phi)] = 0\ .$$

The *poloidal* component of this, which is the toroidal component of the expression in the square brackets[1] is

$$\nabla \times (\boldsymbol{u}_\mathrm{p} \times \boldsymbol{B}_\mathrm{p} + \boldsymbol{u}_\phi \times \boldsymbol{B}_\phi) = 0\ ,$$

where $\boldsymbol{u}_\phi \times \boldsymbol{B}_\phi = 0$, as $\boldsymbol{u}_\phi || \boldsymbol{B}_\phi$.
The *toroidal* component, which is the polodal component of the expression in the square brackets above, is

$$\nabla \times (\boldsymbol{u}_\mathrm{p} \times \boldsymbol{B}_\phi + \boldsymbol{u}_\phi \times \boldsymbol{B}_\mathrm{p}) = 0\ .$$

As the axisymmetry is supposed, the toroidal vector field $\boldsymbol{u}_\mathrm{p} \times \boldsymbol{B}_\mathrm{p}$ from the poloidal component could not be a gradient of some single-valued electrostatic potential and we can write, for the parallel vector fields $\boldsymbol{u}_\mathrm{p}$ and $\boldsymbol{B}_\mathrm{p}$[2]

$$\boldsymbol{u}_\mathrm{p} = \kappa \boldsymbol{B}_\mathrm{p}\ . \tag{2.14}$$

Here, $\kappa = \kappa(R, z)$ is a scalar function, constant for the surface of a constant magnetic flux. The equation for the toroidal component consists only of the toroidal part, and when we insert the Eq. (2.14) and $\boldsymbol{u} = \boldsymbol{u}_\mathrm{p} + \boldsymbol{\omega} \times \boldsymbol{R}$, we obtain, after performing the rotation operation and using $\nabla \cdot \boldsymbol{B} = 0$:

$$R(B_\mathrm{R}\frac{\partial}{\partial R} + B_\mathrm{z}\frac{\partial}{\partial z})(\omega - \frac{\kappa B_\phi}{R}) = 0\ ,$$

for $\boldsymbol{B} = B_\mathrm{R}\boldsymbol{e}_\mathrm{R} + B_\phi \boldsymbol{e}_\phi + B_\mathrm{z}\boldsymbol{e}_\mathrm{z}$. From this equation follows, for the axisymmetry case,

$$\boldsymbol{B} \cdot \nabla(\omega - \frac{\kappa B_\phi}{R}) = 0\ ,$$

and along the magnetic field line $a$:

$$\omega - \frac{\kappa B_\phi}{R} = \Omega(R, z) = \Omega(a) = const\ . \tag{2.15}$$

---

[1] The rotation of the poloidal vector field gives the toroidal vector field, and vice versa.

[2] Note that the total velocity $\boldsymbol{u}$ is *not* parallel to the total magnetic field $\boldsymbol{B}$; because of a toroidal field component the plasma can slide along the field in toroidal direction.

For the axisymmetry case it is $\nabla \cdot \boldsymbol{B} = \nabla \cdot \boldsymbol{B}_{\rm p} = 0$, and we can write, along the magnetic field line $a$:

$$\nabla \cdot (\rho \boldsymbol{u}) = \nabla \cdot (\rho\kappa \boldsymbol{B}_{\rm p}) \ \Rightarrow \rho\kappa \equiv \xi(a) = const \ .$$

We can define a *magnetic flux* function

$$\Psi(R,z) = \frac{1}{2\pi} \int \boldsymbol{B}_{\rm p} \cdot d\boldsymbol{A} \tag{2.16}$$

which is the magnetic flux through a circle of radius $R$, centered at the axis of symmetry. Here, $d\boldsymbol{A}$ is the surface element.

As the magnetic field lines of the axisymmetric magnetic field enclose the flux surfaces, $\xi(\Psi) \equiv \rho\kappa$ is constant along the corresponding flux surface. If we enter it in the toroidal component of Ampère's law (2.3), we obtain

$$\frac{1}{R}(\omega R - \frac{\xi}{\rho} B_\phi) = \Omega_F(a) = \Omega_F \ .$$

It is Ferraro's law of isorotation (Ferraro 1937), where $\Omega_F = \Omega_F(\Psi)$ is the *isorotation parameter*, which can be interpreted, for illustration, as the angular velocity of the foot points of the field lines in the disk.

The following two important conserved quantities are the total angular momentum and energy per unit density, which are conserved along each magnetic field line.

In the stationary, axisymmetric case, the equation of motion (2.2) becomes

$$\frac{1}{4\pi\rho}(\nabla \times \boldsymbol{B}) \times \boldsymbol{B} - (\nabla \times \boldsymbol{u}) \times \boldsymbol{u} = \nabla(\frac{p}{\rho} + \frac{1}{2}|\boldsymbol{u}|^2 + \Phi), \tag{2.17}$$

with the toroidal component

$$[\frac{1}{4\pi\rho}(\nabla \times \boldsymbol{B}) \times \boldsymbol{B}]_\phi = \frac{1}{R} \boldsymbol{u} \cdot \nabla(\omega R^2) \ .$$

This equation we can write as

$$\boldsymbol{B}_{\rm p} \cdot \nabla(\frac{R B_\phi}{4\pi} - \rho\kappa\omega R^2) = 0 \ .$$

It follows that

$$\ell(a) = R u_\phi - \frac{R B_\phi}{4\pi\xi} \ , \tag{2.18}$$

where $\ell(a)$ is the specific (per unit density) angular momentum, conserved along the magnetic field line.

The poloidal component of the equation of motion (2.17) will provide the conservation law for the specific energy:

$$[\frac{1}{4\pi\rho}(\nabla \times \boldsymbol{B}) \times \boldsymbol{B}]_{\rm p} = [\nabla(\frac{p}{\rho} + \frac{1}{2}|\boldsymbol{u}|^2 + \Phi)]_{\rm p} \ .$$

When we multiply this equation by $\boldsymbol{B}_{\rm p}$, we obtain Bernoulli equation:

$$e(a) = \frac{1}{2}u^2 + \frac{p}{\rho} + \Phi - \frac{\Omega_F R B_\phi}{4\pi\xi} \tag{2.19}$$

along the magnetic field line.

## 2.3 The code: ZEUS-3D

In order to solve the MHD equations for a jet formation we use the non-relativistic ZEUS-3D code (Clarke et al. 1994). It is a three-dimensional, non-relativistic, ideal MHD *fluid* equation solver. Assumed is a fluid with a coupling of the matter to the magnetic field via collisions with an ionized component in which a charge separation never occurs. Magnetic fields are evolved using the constrained transport method (Evans & Hawley 1988), which guarantees, within the machine numerical precision, that no monopoles will be generated. For the calculation of the electromotive force and the transverse Lorentz force, an advanced method of characteristics (MOCCT, Hawley & Stone 1995) is used. The accuracy and stability of the code, when an effective pressure is introduced, is ensured by taking in account the effective sound wave propagation by Courant & Friedrichs (1948).

The equations which original ZEUS-3D is solving are:

$$\frac{\partial \rho}{\partial t} + \nabla \cdot (\rho \boldsymbol{u}) = 0 \tag{2.20}$$

$$\frac{\partial (\rho \boldsymbol{u})}{\partial t} + \rho(\boldsymbol{u} \cdot \nabla)\boldsymbol{u} + \nabla p + \rho \nabla \Phi - \frac{\boldsymbol{j} \times \boldsymbol{B}}{c} = 0 \tag{2.21}$$

$$\frac{\partial \boldsymbol{B}}{\partial t} - \nabla \times (\boldsymbol{u} \times \boldsymbol{B}) = 0 \tag{2.22}$$

$$\rho \left[ \frac{\partial e}{\partial t} + (\boldsymbol{u} \cdot \nabla)\, e \right] + p(\nabla \cdot \boldsymbol{u}) = 0 \tag{2.23}$$

For the gas law we applied a polytropic equation of state

$$p = K\rho^\gamma \;,\; \gamma = \frac{5}{3}$$

i.e. the internal energy (per unit volume) of a system in our simulations is not solved by the energy equation (2.23), but defined by the internal energy

$$e = \frac{p}{\gamma - 1} \;. \tag{2.24}$$

For jets it is appropriate to use the 2D-axisymmetry option for cylindrical cordinates (R,$\phi$,z). The gravitational potential is that of a point mass $\Phi = -GM/\sqrt{R^2+z^2}$ located at the origin.

In ZEUS-3D there is used a *staggered* mesh, i.e. different physical quantities are defined in a different grid positions. There are three intertwined grids: scalars (e.g. density, pressure) are located at the zone center, the magnetic fields and velocities at the zone faces, and electromotive forces (EMFs) along the zone edges of the computational grid cells.

This scheme gives the possibility to solve the equations involving gravity exactly, without softening of the gravitational potential, which could have a significant effect on the results (Bell & Lucek 1995; OP97). Also, the number of interpolations required at the zone faces is reduced. The interpolations are performed with the second-order accurate scheme proposed by van Leer (1974).

### Numerical boundary conditions

The computational grid of the ZEUS-3D code consist of the *active* zones, where the equations are solved and, at the boundaries of the grid, the *ghost* zones, where boundary conditions are prescribed (Stone & Norman 1992a,b; Hawley & Stone 1995; OP97; Fendt & Elstner 2000, hereafter FE00). These boundary conditions are explicit equations which give the values of the dependent variables in the ghost zones from the values in the active zones of the grid.

An “inflow” boundary condition means that the values of all the variables in the ghost zones are predetermined and do not change in time.

A “reflecting” boundary condition is set when all the variables except the normal components of velocity are set equal to the corresponding values of their images along the active zones. For the velocity there are two ghost zones, and the normal component of velocity is set to zero in the first, and reflected in the second ghost zone. This boundary condition is used e.g. for setting the symmetry axis in cylindrical coordinates.

An “outflow” condition is set when the flow is extrapolated beyond the boundary. All the values of variables in the ghost zones are set equal to the values in the corresponding active zones. To handle the outgoing Alfvén waves properly, the angular velocity and toroidal magnetic field are projected.

For the symmetry planes, such as equatorial plane, implemented is a condition in which the velocity is reflected, while the normal component of the magnetic field is continuous and the tangential component is reflected. The toroidal magnetic field is antireflected at such a plane.

# Chapter 3

# Model of MHD jet formation

One of the critical problems in the theory of star formation is that the gas from which a star forms has an angular momentum (per unit mass) up to a million times larger than that of a finally formed star. This problem also emerges in the theory of the formation of the rotating black holes.

The presence of an accretion disk in most of these systems leads to the conclusion that the excess angular momentum is shed through the disk by a disk wind.

The viscous disk theory (Shakura & Sunyaev 1973; Lynden-Bell & Pringle 1974) is unable to provide a reason for the outflows. If we include the magnetic field in the model, the wind mass-loss rate need only be a small fraction of the accretion rate of the disk for the transport of the angular momentum through the disk surfaces. The gravitational energy that also must be released in accretion, transports outwards as a mechanical energy of a disk wind.

The model evolution of a disk wind into a collimated jet must concern the interplay between the accretion in the disk, the ejection of matter in the jet, the acceleration of matter to high poloidal velocities, and the collimation of the wind into a narrow beam. A number of studies of magnetized jets initiated by the paper of Blandford & Payne (1982) (e.g. Camenzind 1986; Lovelace et al. 1987; Heyvaerts & Norman 1989; Chiueh et al. 1991; Pelletier & Pudritz 1992; Li et al. 1992; Contopoulos 1995a), focused mostly on the jet acceleration and collimation. However, the question which are the requirements for the accretion disk to be a boundary condition for the jet ejection, was not answered. All self-similar solutions before Ferreira (1997) included substantially limiting approximations.

In Ferreira's paper the jet is constructed in a self-consistent *stationary* approach, taking into account the feedback of the underlying disk. This was further developed in Casse & Ferreira (2000a,b). Essential was the inclusion of a dissipative mechanism – the magnetic diffusivity – in the disk, so that the matter could cross the magnetic field surfaces and be ejected outwards.

## 3.1 Self-similar models of jet launching

The time-dependent MHD equations are too complicated to be solved either analytically or numerically without some simplifying assumptions.

The toroidal component of Ampère's law (2.3) is

$$(\nabla \times \boldsymbol{B})_\phi = \frac{4\pi}{c}\boldsymbol{j}_\phi \, .$$

The magnetic flux function (2.16) is, for the axisymmetric magnetic field ($\partial/\partial\phi = 0$), a scalar potential which labels the surfaces of constant magnetic flux. From this scalar potential we can write, in cylindrical coordinates, the poloidal magnetic field $\boldsymbol{B}_\mathrm{p} = \frac{1}{R}\nabla\Psi \times \boldsymbol{e}_\phi$. The toroidal component of Ampère's law we can now re-write as

$$R\nabla \cdot \left(\frac{1}{R^2}\nabla\Psi\right) = -\frac{4\pi}{c}j_\phi \, .$$

This is the *Grad-Shafranov* equation and it is a partial differential equation of the second order. With the self-similarity assumption[1] we can reduce it to a set of ordinary differential equations, and so find the force balance.

In the MHD of jet formation, the hydromagnetic equations are solved with such self-similar ansatz for the magnetic field: $B(R,\phi,0) \propto r^{-5/4}$ is set for axisymmetric flow from a thin, magnetized Keplerian disk around a central object of mass M. This assumption reduces the mathematical problems considerably.

### 3.1.1 Blandford & Payne solution

In the BP82 model, a centrifugally driven outflow of matter from the disk is possible for the angles of the poloidal component of the magnetic field to the disk axis of at least 30°. BP82 demonstrated numerically that it is possible for an outflow to pass smoothly through the corona, nearby the disk surface, and be still considered cold (i.e. without the pressure) and injected from rest.

There is a mechanical analogy (Henriksen & Rayburn 1971), describing this model. The magnetic field lines are frozen into and convected by the disk. Because of the constant angular velocity on a field line, the gas elements on the field lines behave like beads on a rigid wire. The equipotential surfaces of such "beads", released from rest at $R_0$ and corotating with the Keplerian angular velocity $\Omega_\mathrm{K} = \sqrt{(GM/R_0^3)}$ are, in cylindrical coordinates (see Fig. 3.1)

$$\Phi(R,z) = -\frac{GM}{R_0}\left[\frac{1}{2}\left(\frac{R}{R_0}\right)^2 + \frac{R_0}{\sqrt{R^2+z^2}}\right] = const \, .$$

The critical angle of the BP82 can be derived analytically (see, e.g. Campbell 1997,

---

[1] Self-similarity implies that all the quantities are given by a power law of spherical (or cylindrical) radius along a given direction.

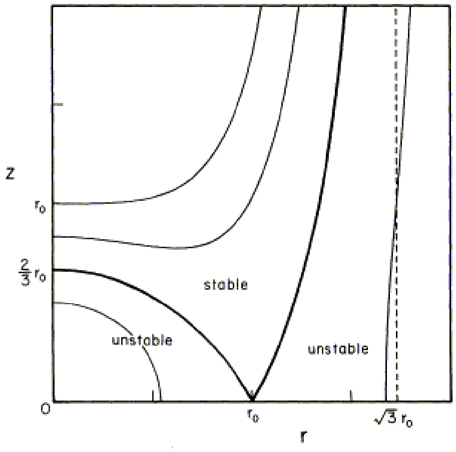

Figure 3.1: Equipotential surfaces for a "bead on a wire" model (adopted from BP82). The dashed line marks the asymptote for the surface of marginal stability.

§12). The equation of the line making an angle $i$ with the disk equatorial plane is

$$z = \tan i(R - R_0) \ . \tag{3.1}$$

For a unit vector along the magnetic field $\boldsymbol{s}_0 = \cos i\boldsymbol{R}_0 + \sin i\boldsymbol{z}_0$ the force per unit mass along the poloidal magnetic field is

$$\frac{d\psi}{ds} = \frac{GM}{(R^2+z^2)^{3/2}}(R\cos i + z\sin i) - \frac{GM}{R_0^3}R\cos i \ .$$

A force balance along the field is achieved when

$$\frac{R\cos i + z\sin i}{(R^2+z^2)^{3/2}} = \frac{R\cos i}{R_0^3}$$

In the disk equatorial plane, where $R$=$R_0$ and $z$=0, this condition is satisfied, but the stability of the balance is dependent on $i$. If we assume $z/R_0 \ll$1 and expand the last equation above and Eq. (3.1) to the second order in $z/R_0$, we obtain

$$\frac{z}{R_0}\left[(\tan^2 i + 3)(\frac{z}{R_0}) - \tan i(\tan^2 i - 3)\right] = 0 \ .$$

The solution in the equatorial plane $z$=0, and the solution

$$\frac{z}{R_0} = \frac{\tan i(\tan^2 i - 3)}{\tan^2 i + 3}$$

shows that for $i$>0 the field line points have $z \geq 0$, and that there exists a critical angle $\tan^{-1}\sqrt{3} = 60°$ for a validity of the solution. If $i$ is less or equal to this critical angle, the equilibrium solution at $z$=0 is the only one, and for the larger $i$'s, a force balance could also occur above the disk equatorial plane.

The sign of $d^2\psi/ds^2$ determines the stability of the equilibrium points. It turns out that for $i$>60°, because of the potential barrier, the material in the disk equatorial plane requires sufficient thermal energy to exit the potential well.

The toroidal component of the magnetic field, prevailing at large distances from the disk, collimates the outflow perpendicular to the disk. Far from the disk, the centrifugal forces are not important, and a balance between the (inwards) hoop stress and the (outwards) magnetic pressure determines the shape of the field lines.

Pudritz (1985) proposed that a magnetic wind of Blandford & Payne could extract *all* the angular momentum of the accreted matter, instead of turbulent viscosity (Pelletier & Pudritz 1992).

## 3.2 Disk-jet connection: Stationary solutions

Königl (1989), connected the jet and disk dynamics for the first time for both AGN and YSOs, matching the BP82 jet solutions with inviscid MHD accretion flow solutions. However, the disk vertical equilibrium was treated only partially (by setting $\partial u_\phi/\partial z = 0$ and $u_z = 0$), and the heating and radiation were neglected. Similarly, based on the induction equation of magnetic field alone, was the case in Lovelace et al. (1987) and Wang et al. (1990, 1992). They discussed the electrodynamics of *viscous* resistive accretion disk around a black hole, with a self-collimated electromagnetic (relativistic) jet.

Wardle & Königl (1993), Ferreira & Pelletier (1993, 1995) and Li (1995) also directly matched their solutions to BP82 solutions, incompletely treating the disk vertical equilibrium. This prevented the description of the change of radial motion of the plasma (the accretion) in the disk into a vertical motion (the ejection).

The solution with all the dynamical terms was given in Ferreira & Pelletier (1995), and the final proof that these solutions can produce the super-Alfvénic jets was given in Ferreira (1997). In this approach, the turbulent underlying disk and the anomalous transport coefficients are assumed. The matter crosses the magnetic field lines because of the turbulent magnetic diffusivity, and then lifts above the disk.

The equations governing the behavior of such system are a stationary ($\partial/\partial t$=0) continuity equation (2.1), the equation of motion (2.2), the toroidal component of Faraday's law (2.4) and the diffusion equation (2.9).

We will derive the last two equations required above. For a stationary case, from the magnetic diffusion equation (2.8),

$$\frac{\partial \boldsymbol{B}}{\partial t} = 0 = \nabla \times [\boldsymbol{u} \times \boldsymbol{B} - \eta \nabla \times \boldsymbol{B}] \Rightarrow \eta \boldsymbol{j} = \frac{c}{4\pi} \boldsymbol{u} \times \boldsymbol{B} \ ,$$

with use of Ampère's law (2.3). The toroidal component of this equation is

$$\eta \boldsymbol{j}_\phi = \frac{c}{4\pi} \boldsymbol{u}_{\rm p} \times \boldsymbol{B}_{\rm p} \ . \tag{3.2}$$

The toroidal component of the stationary diffusion equation is

$$\nabla \times (\boldsymbol{u}_{\rm p} \times \boldsymbol{B}_\phi + \boldsymbol{u}_\phi \times \boldsymbol{B}_{\rm p}) = \eta \nabla \times (\nabla \times \boldsymbol{B}_\phi) \ ,$$

and it is possible to rewrite it as

$$\nabla \cdot \left[ \frac{\eta'}{R^2} \nabla (R B_\phi) \right] = \nabla \cdot \left[ \frac{1}{R} (B_\phi \boldsymbol{u}_{\rm p} - \boldsymbol{B}_{\rm p} u_\phi) \right] \ . \qquad (3.3)$$

A "toroidal" magnetic diffusivity $\eta'$ is introduced here, to account for a possible anisotropy with respect to a "poloidal" diffusivity $\eta$ (Ferreira & Pelletier 1993, 1995). The parametrization of $\eta$ is taken to be due to Alfvénic turbulence of typical correlation length of order of the disk height scale $h$: $\eta = \alpha u_{A,z} h$, where $u_{A,z} \equiv B_z / \sqrt{\rho}$ and $\alpha \lesssim 1$.

The hydrostatic equilibrium in the disk is maintained by the magnetic torque

$$F_\phi = j_z B_R - j_R B_z \ ,$$

and the Lorentz force is responsible for the lifting of the plasma above the disk surface. In Ferreira & Pelletier (1993b) it is shown that the ejection of the matter from the disk is only possible for the Keplerian disk if the radial current density $j_R$ decreases vertically on a disk scale height. The reason is that the torque $F_\phi$ is negative inside the disk, and it has to become positive at the disk surface if it is to provide a magnetic acceleration. In conclusion, the matter is accreted across the magnetic field lines of the diffusive disk, and then ejected as a disk wind – see Fig. 3.2.

The jets are governed by the *ejection index* parameter, which measures local efficiency of the conversion of the accretion stream into the jet ejection. The disk vertical structure and the angular momentum transfer are found to constrain the injection index, and it lies in a very narrow range.

Another important result in Ferreira (1997) is that the disk vertical equilibrium implies a minimum mass of the ejected jet. Also, the jet flow asymptotic behavior depends on the ratio (which has to be $\gtrsim$1) of the isorotation parameter to the poloidal Alfvén speed at the Alfvén surface.

## 3.3 Critical surfaces in the outflow

The equation for the conservation of total energy per unit mass of the MHD flow on each magnetic surface (or along the field line) can be derived from the equation of motion. After the scalar product of Eq. (2.2) with $\boldsymbol{B}_{\rm p}$, Bernoulli equation (2.19) is obtained. In this context it is referred to as the *wind* equation.

The constant specific angular momentum (2.18) can be written as

$$\ell(a) = \omega R^2 - \frac{R B_\phi}{4\pi\xi} = const \equiv \Omega_* R_{\rm A}(a)^2 \ , \qquad (3.4)$$

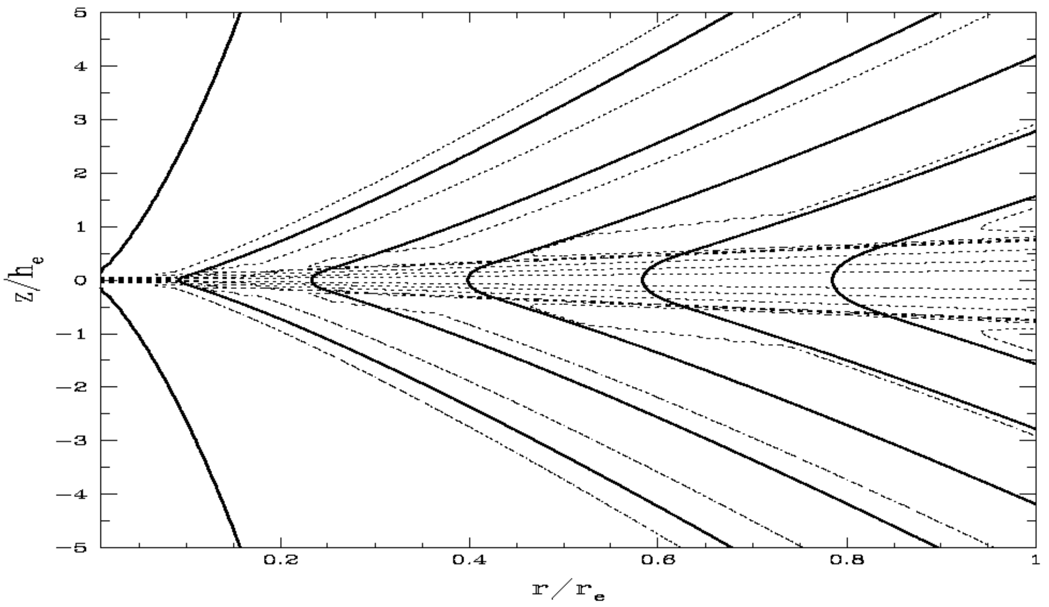

Figure 3.2: The solution for a magnetized accretion disk driving jet (adopted from Ferreira 1997). The plasma (*dotted* lines) enters at the disk outer edge and is accreted through the magnetic field (*solid* lines). The diffusion enables transition between the accretion disk and the ideal MHD jet. This occurs up to one disk height scale above the disk. Higher above the disk, the plasma becomes “frozen” in a magnetic field and the Lorentz force accelerates it.

where $R_{\rm A}$ is the *Alfvén radius*, the lever arm for the torque acting at the foot point of the jet. From this equation we see that, as a corrotation with the rotor increases the angular momentum of the gas, the toroidal magnetic field must increase, for $\ell(a)$ to remain constant. The wind (or the jet) can remove the angular momentum very efficiently due to large lever arm.

Now, with $h$ for the enthalpy, Bernoulli equation can be written as

$$\frac{1}{2}u^2 + h + \Phi + \Omega_*(\Omega_* R_{\rm A}^2 - Ru_\phi) = e(a) = const\ . \tag{3.5}$$

The contribution due to the magnetic field is $\Omega_*(\Omega_* R_{\rm A}^2 - Ru_\phi)$.

There is an important result, first obtained by Michel (1969), following from the Eq. (3.5). For outflowing gas at large distances from the source, we can neglect the gravitation, and find the terminal speed of the outflow:

$$u_\infty \simeq \sqrt{2}\Omega_*(a) R_{\rm A}(a)\ . \tag{3.6}$$

What happens with the portion of a gas lifted from the surface of the thin, Keplerian accretion disk by the centrifugal force? The velocity of the matter is not high, but it is then accelerated by a magnetic forces. The propagating matter reaches, and exceeds, the speed of the slow magnetosonic, the Alfvén, and the fast magnetosonic waves. Note that the MHD waves in the super magnetosonic jets can not travel faster than the

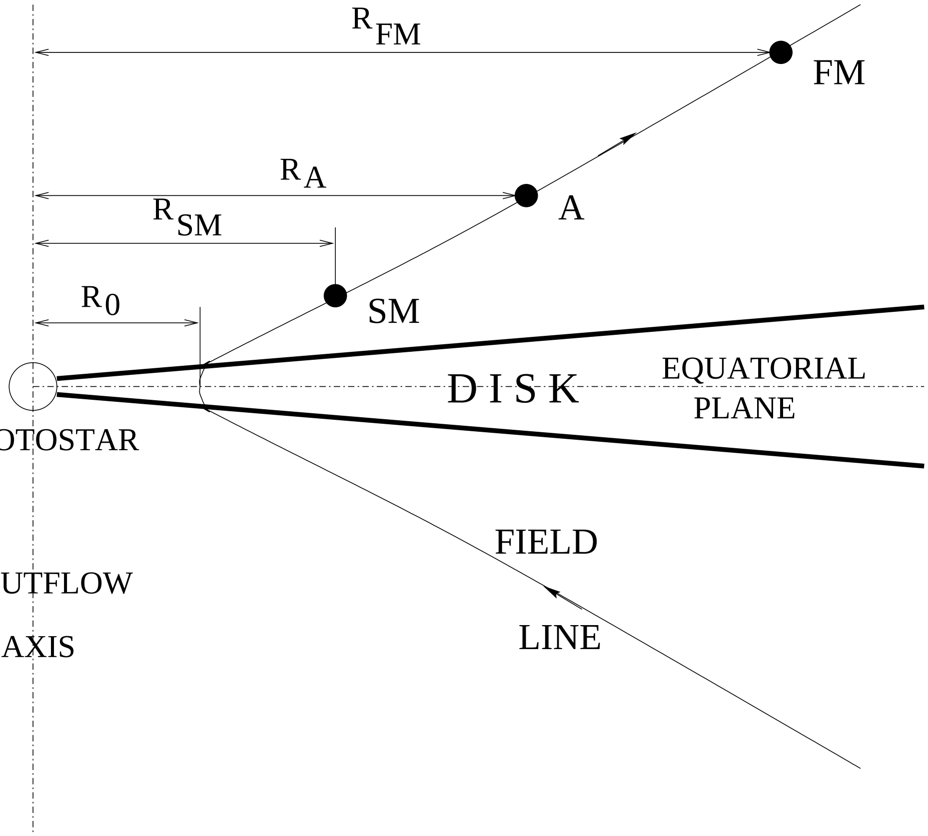

Figure 3.3: Three critical points of the flow. The slow and fast magnetosonic points SM and FM are depicted, and the point at the Alfvén surface A.

fast magnetosonic waves. This implies that any disturbance from the interaction of the jet with the ambient medium can not influence the foot point of such a jet.

For a polytropic gas law Bernoulli equation, often referred to as the wind equation, can be rewritten as

$$e = \frac{u_p^2}{2} - \frac{GM}{\sqrt{R^2+z^2}} + \frac{\Omega_F^2}{2R^2}\left(\frac{M_{\rm A}^2 R_{\rm A}^2 - R^2}{M_{\rm A}^2 - 1}\right)^2 - \Omega_F^2 \frac{R_{\rm A}^2 - R^2}{M_{\rm A}^2 - 1} + \frac{c_{\rm s,0}^2}{\gamma - 1}\left(\frac{M_{\rm A,0}}{M_{\rm A}}\right)^{2(\gamma-1)} ,$$

where M is the mass of the central object, $M_{\rm A}$ is the Alfvén Mach number, $\gamma$ is the polytropic index, and subscript 0 denotes values at the foot point of a given magnetic field line. Three critical points for the flow are shown in Fig. 3.3. For all the points where $M_{\rm A} \equiv u_{\rm p}\sqrt{4\pi\rho}/B_{\rm p}$=1 (the Alfvén points), for $R$=$R_{\rm A}$ there is no singularity. This determines the angular momentum $\ell = \Omega_{\rm F} R_{\rm A}^2$ at the *Alfvén surface*. For the slow and fast magnetosonic point some additional constraints for the flow are required for a regular solutions (Pelletier & Pudritz 1992, their §2.2).

Near to the disk, in the disk *cold* corona, in which the centrifugal force dominates the gas pressure, located is the slow magnetosonic (SM) point. This is the MHD analog of the sonic point in the hydrodynamics. The magnetic pressure highly exceeds the gas pressure and far enough from the central object, the effective gravity vanishes. The gas is then accelerated by the centrifugal and magnetic forces.

The fast magnetosonic (FM) speed is the speed of a wave in the total magnetic field, not only its poloidal component, as was in the case of the Alfvén speed. At the FM point a toroidal magnetic field becomes strong enough to collimate the outflow.

In Fig. 3.3 denoted are the slow and fast magnetosonic points, with the corresponding radii $R_{\rm SM}$ and $R_{\rm FM}$.

Projections of the Lorentz force from the Eq. (2.11) parallel and perpendicular to the poloidal magnetic surfaces are helpful to describe the outflow dynamics. The total poloidal current flowing within the surfaces is equal to $I(R,z) = \int \boldsymbol{j}_{\rm p} \cdot d\boldsymbol{A} = -cRB_\phi/2$ and the components are (Ferreira 1997):

$$\begin{aligned} \boldsymbol{F}_{\rm L||} &\equiv \boldsymbol{j}_\perp \times \boldsymbol{B}_\phi = -\frac{B_\phi}{2\pi R}\nabla_{||} I \ , \\ \boldsymbol{F}_{\rm L\perp} &\equiv \boldsymbol{j}_{||} \times \boldsymbol{B} = B_{\rm p} j_\phi - \frac{B_\phi}{2\pi R}\nabla_\perp I \ , \\ \boldsymbol{F}_{\rm L\phi} &= \frac{B_{\rm p}}{2\pi R}\nabla_{||} I \ . \end{aligned} \tag{3.7}$$

In these equations, $\boldsymbol{j}_{\rm p} = c\nabla(RB_\phi)/(4\pi R) \times \boldsymbol{e}_\phi$ is the poloidal electric current, $\nabla_{||} \equiv (\boldsymbol{B}_{\rm p} \cdot \nabla)/B_{\rm p}$ and $\nabla_\perp \equiv (\nabla\Psi \cdot \nabla)/|\nabla\Psi|$. Crossing of the current through the poloidal magnetic surface accelerates the plasma ($\nabla_{||} I > 0$). In a consequence, a poloidal $F_{||}$ magnetic force is produced, and a centrifugal force is produced via the toroidal magnetic field.

For a vanishing current $I$, there is no magnetic acceleration. The same is for the current flow parallel to the magnetic surface.

## 3.4 Mass flow rates in jet-disk system

What are the mass accretion rates in the disk and in the outflow, and how much of the disk angular momentum is extracted?

The wind mass flow rate through a circle of radius R we can obtain, for the surfaces of the constant magnetic flux $\Psi(R,z)$ defined in Eq. (2.16):

$$\begin{aligned} \dot{M}_{\rm W}(R) &= \int_0^R \rho u_{\rm z} 2\pi R' dR' = \left(\rho \boldsymbol{u}_{\rm p} = \frac{\xi(\Psi)}{4\pi}\boldsymbol{B}_{\rm p} \Rightarrow \rho u_{\rm z} = \frac{\xi(\Psi)}{4\pi}\frac{1}{R}\frac{\partial\Psi}{\partial R}\right) \\ &= \int_0^R \frac{\xi(\Psi)}{4\pi}\frac{1}{R'}\frac{\partial\Psi}{\partial R'} 2\pi R' dR' = \int_0^R \frac{\xi(\Psi)}{2}\frac{\partial\Psi}{\partial R'} dR' \Rightarrow \frac{d\dot{M}_{\rm W}}{dR} = \frac{\xi(\Psi)}{2}\frac{\partial\Psi}{\partial R} \\ &\text{i.e. } \ \xi(\Psi) = 2\frac{\partial\dot{M}_{\rm W}}{\partial\Psi} \ . \end{aligned} \tag{3.8}$$

If the disk contains sufficient magnetic flux for the viscosity to become unimportant in the angular momentum equation

$$\nabla \cdot \left( \rho \boldsymbol{u}_{\mathrm{p}} \omega R^2 - \frac{R B_\phi \boldsymbol{B}_p}{4\pi} \right) = \nabla \tau_{\mathrm{visc}} \ ,$$

where $\tau_{\mathrm{visc}}$ is the viscous torque in the disk (the $(R, \phi)$ component of the stress-energy tensor), we can integrate it vertically over $z$:

$$\frac{1}{R}\frac{d}{dR}(R\Sigma u_{\mathrm{R}} \omega R^2) = \frac{h}{4\pi R}\frac{d}{dR}(R^2 B_{\mathrm{R}} B_\phi)|_{z=0} + \frac{R}{2\pi} B_{\mathrm{z}}(R,h) B_\phi(R,h) \ . \tag{3.9}$$

It is the angular momentum equation for the disk under a wind torque. The height above the disk equator is $h$, and $\Sigma$ is the disk surface density. At the disk equator, there is no radial angular momentum transport, and we can ignore the first term on the right hand side.

For the accretion rate through the disk $\dot{M}_{\mathrm{a}} = -2\pi R \Sigma u_{\mathrm{R}}$ we obtain

$$\dot{M}_{\mathrm{a}} \frac{d(\omega R_0^2)}{dR_0} + 2\frac{d\dot{M}_{\mathrm{W}}}{dR_0} \left( 2\omega R_0^2 - \ell(\Psi) \right) = 0 \ . \tag{3.10}$$

For the Alfvén surface far from the disk, $R_{\mathrm{A}}(R_0) \gg R_0$ and $\ell(\Psi) \gg \omega R_0^2$.

From this equation we see the intrinsic linking of the wind mass loss and the disk accretion rate.

The accretion process means the transport of the angular momentum from the system. In the disk-jet paradigm, this transport is accomplished through fast and well collimated outflows (the jets). The idea, stated by BP82; Pudritz & Norman (1986); Königl (1989) is simple: The rate at which the angular momentum is removed from the disk is

$$\dot{J}_{\mathrm{acc}} = \frac{1}{2} \omega R^2 \dot{M}_{\mathrm{acc}} \ , \tag{3.11}$$

where $\dot{M}_{\mathrm{acc}}$ is the accretion rate through the disk. The angular momentum carried away by a disk wind is

$$\dot{J}_{\mathrm{W}} = \dot{M}_{\mathrm{W}} \omega R_{\mathrm{A}}^2 \ , \tag{3.12}$$

where $\dot{M}_{\mathrm{W}}$ is the mass loss rate in the wind, $\omega$ is the local angular velocity, and $R_{\mathrm{A}}$ is the local Alfvén radius.

For all the angular momentum removed by the wind, we would obtain

$$\frac{\dot{M}_{\mathrm{W}}}{\dot{M}_{\mathrm{acc}}} = \frac{1}{2} \left( \frac{R}{R_{\mathrm{A}}} \right)^2 \ . \tag{3.13}$$

From this equation it follows that for $R_{\mathrm{A}} \sim 10R$ only less than 1% of the accreted mass is enough for the accretion process to be effective enough for removal of the excess of the angular momentum from the system. Such mass loss complies with the observed ones.

## 3.5 MHD of jet formation

Astrophysical jets are definitely *not* stationary objects. Although the large-scale appearance of a jet is static, the jet propagation is fast. And there are fast moving *knots* inside, co-moving with the jet. Also, if the dynamics during the initiation of the outflow is to be investigated, the time-dependent equations must be solved. Because of the complexity of the MHD equations, the only currently effective tool are numerical MHD simulations.

In general, numerical simulations of magnetized axisymmetric outflows from the accretion disks can be devided into two approaches. The first includes the disk dynamics, and the second does not.

### 3.5.1 MHD simulations of disk *and* jet

Uchida & Shibata (1985) and Shibata & Uchida (1985, 1986) performed the first numerical simulations of the rotating gaseous disk in a large-scale magnetic field. In their “sweeping magnetic twist mechanism”, twisting of the magnetic field lines because of the disk rotation accelerates the outflow (by the Lorentz force) perpendicular to the disk planes. In difference to the BP82 mechanism, the acceleration is not magneto-centrifugal, but caused mainly by the magnetic pressure gradient (Contopoulos 1994).

Their results were confirmed by computations using the ZEUS code by Stone & Norman (1994b). They also discussed the relation between the magnetic braking and magnetorotational instability (MRI, Balbus & Hawley, 1991).

The diffusive accretion disk in interaction with a stellar dipolar atmosphere was investigated in the simulations by Hayashi et al. (1996); Miller & Stone (1997); Goodson et al. (1997); Kuwabara et al. (2000). As a general feature, all showed that the inner disk collapses after a few rotations, and that from the outer parts of the disk wind the plasmoids are episodically ejected.

The outflows were collimated perpendicular to the disk, but the numerical reasons prevented performing of the simulations for longer than few tens of Keplerian periods at the inner disk radius. Therefore, the collimation could be influenced by the initial and boundary conditions. The failures of the disk simulations were caused by the simplifying assumptions of the models, e.g. an assumption of a constant diffusivity in a disk and its corona is probably not very realistic.

In Casse & Keppens (2002) the diffusivity is only effective inside the disk, and the constant, quasi-stationary ejection of matter is reached within the several tens of dynamical disk timescales.

### 3.5.2 The accretion disk as a boundary condition

A highly instructive approach came from Ustyugova et al. (1995). It is suggested that for the MHD simulations of a jet formation it is sufficient to treat the accretion disk as a boundary condition. With this boundary condition, the magnetic flux distribution and the mass inflow into the disk corona are defined, without inclusion of the disk into the computations.

This simplification, when the disk evolution is not computed, makes long-lasting numerical simulations possible, up to hundreds of Keplerian periods of the disk, after which a steady state solutions could appear. In Romanova et al. (1997) the stationary state of a collimated flow has been reached after hundred Keplerian periods.

Ouyed & Pudritz (OP97) simulations with a potential field and a hydrostatic density distribution as the initial conditions, resulted in a collimated disk wind after 400 disk rotations. The gas is accelerated, and then collimated due to the pinch force generated by the outflow. Resulting stationary outflows have many similarities to a stationary disk wind models. A similar result is obtained also in Krasnopolsky et al. (1999), where the magnetic field direction is not conserved any more during the simulation, but only the disk magnetic flux (also the case in Ustyugova et al. 1995).

The jet stability in three-dimensional simulations is investigated in Ouyed et al. (2003). In the same paper previous two-dimensional simulations (OP97, Ouyed & Pudritz 1997b) are verified. The mechanism of jet acceleration shows to be identical in both sets of simulations, but only up to the Alfvén surface of the outflow, after which non-axisymmetric Kelvin-Helmholz instability takes place. However, the jet maintains long-term stability through a self-limiting process in which the average Alfvénic Mach number within the jet remains of the order of unity.

Present observations still fail to provide us informations about the interior of the disk around the young stellar objects. Numerical simulations are, therefore, still the only way to try to understand the processes which form the jets. However, in our present simulations we can investigate only the small portion of the whole system (Fig. 3.4).

## 3.6 Collimation by poloidal magnetic field

The toroidal component of the magnetic field is essential for a collimation and acceleration of the jets described above. The “hoop stress” (the tension of the part of the flow which stops corrotating with the disk, and adds loops of the toroidal field to the flow for each rotation of the foot point of the field line anchored in the disk) collimates the flow.

Spruit et al. (1997) argue the toroidal fields developing in a magnetically accelerated jet are sufficiently unstable not to be able to contribute much to the collimation. As noticed e.g. in the plasma confinement devices (Bateman 1980), the toroidal fields are

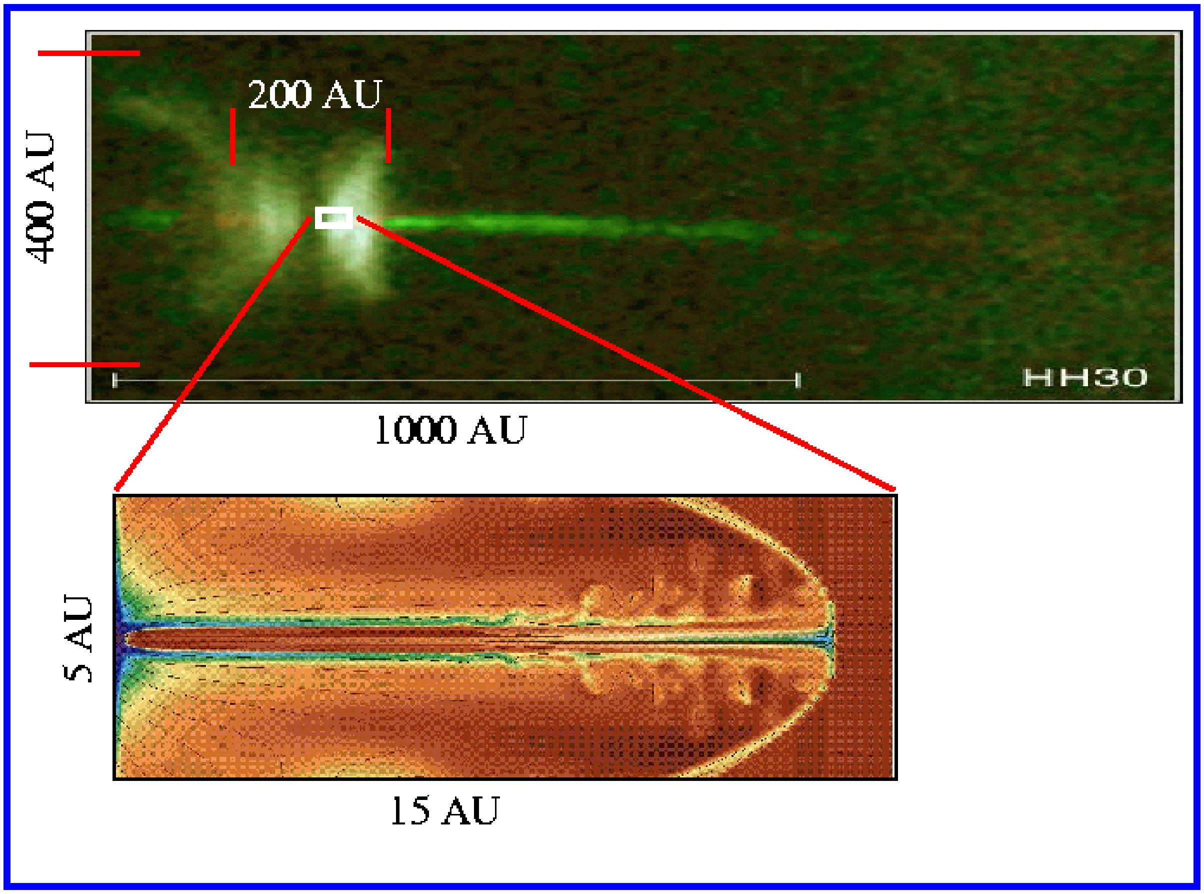

Figure 3.4: The scales of numerical simulations and observations. Still only the very interior part of the system, hidden from us in present observations, could be simulated. The small white box is the region inside the dust disk around the young stellar object HH30 which we can investigate in our simulations. Credits for the top panel image: C. Burrows, the WFPC2 Investigation Definition Team and NASA.

highly unstable to non-axisymmetric instabilities (kink instability). These instabilities are the result of the free energy $B_\phi^2$ in the toroidal field (Tayler 1980; Pitts & Tayler 1985). If the jet collimation is due to the toroidal field, this instability directly affects it (Eichler 1993). The toroidal magnetic field decay and the internal pressure build-up due to the kink instability could decollimate the outflow.

The collimation of the jet is then due to the magnetic pressure because of the poloidal field of the disk, and is dependent on the ratio of the outer to inner disk radius. This ratio introduces the characteristic distance, called the *collimation distance*, which is of the order of the disk radius or less, and beyond which the jet is fully ballistic and only weakly magnetic.

The initial field of the disk should be $B \approx R^{-\mu}$, with $\mu \lesssim 1.3$ (Spruit et al. 1997). It could be the field internally generated by some dynamo process or captured interstellar magnetic field, and its strength is likely to decrease outwards from the centre of the disk. In the case of the dynamo-generated field, the energy density of the field saturates at some fraction of the gas pressure (Brandenburg et al. 1995, Gammie & Balbus 1994). In another case, a compression by the accretion flow increases the field towards the centre of the disk.

In Chapter 5 we tested this alternative model by numerical simulations with the disk as a boundary condition. We found that launching of the jet occurs indeed, if access to some additional source of energy is assumed (i.e. for a *hot* corona). For the simulations with a *cold* disk corona, the outflows were always dispersed in a radial direction, in our setup.

# Chapter 4

# Resistive MHD simulations of astrophysical jet formation

Observations clearly show that astrophysical jets are not stationary features. However, the knots inside the jet move in the otherwise stable large-scale jet structure, and the formation of knots is not necessarily directly related to the jet formation. Also, a global solution for the magnetic jet, with the magnetic field distribution from the very origin of the outflow (a star or disk) to the asymptotic jet, is at present possible only in *stationary* MHD models.

Such models, however, include substantially simplifying assumptions to avoid the mathematical complications of MHD, connected with the interaction between the magnetic field and matter. Therefore, with the present computational power and its fast advance, a time-dependent approach provides the most promising method for studying the MHD outflows. Some of the problems, as the question of a self-collimation of MHD jets, may be answered by axisymmetric simulations, and some may require three-dimensional simulations for the complete answer, e.g. the jet launching from the turbulent accretion disk. A caveat is that the spatial scale investigated in numerical simulations is still far below the observed global jet scale.

Protostellar jets most probably originate in the turbulent accretion disk surrounding young stellar objects. In our approach we assume that the turbulent pattern in the disk also enters the disk corona and the jet, and we model the turbulence by the magnetic diffusivity.

The project of this thesis has been solving the jet formation problem in two steps: to perform a *resistive* MHD simulations of the jet formation, propagation and collimation with a disk as a boundary condition (Fendt & Čemeljić 2002; present chapter), and then to include a resistive disk in the computational box (Čemeljić & Fendt 2004; Chapter 6 here).

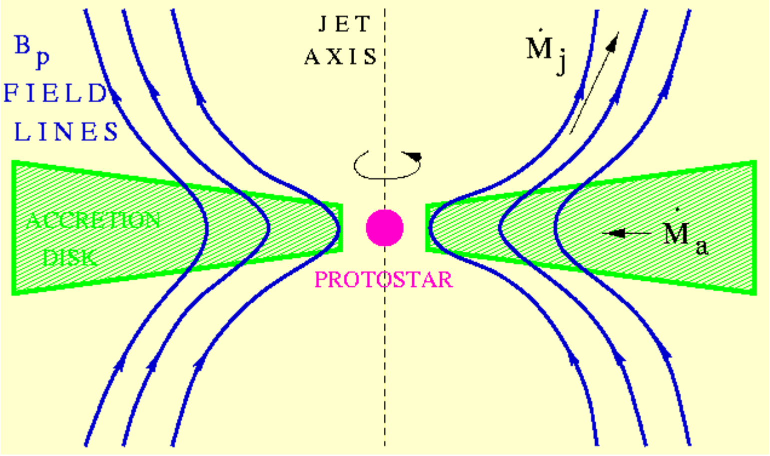

Figure 4.1: Schematic view of the model. Above and under the disk is a disk corona, with the jet propagating in both directions along the magnetic field lines.

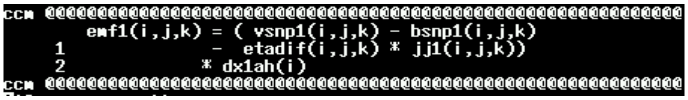

```
ccm @@@@@@@@@@@@@@@@@@@@@@@@@@@@@@@@@@@@@@@@@@@@@@@@@@@@@@@@@@@@@
          emf1(i,j,k) = ( vsnp1(i,j,k) - bsnp1(i,j,k)
     1                     -   etadif(i,j,k) * jj1(i,j,k))
     2                 * dx1ah(i)
ccm @@@@@@@@@@@@@@@@@@@@@@@@@@@@@@@@@@@@@@@@@@@@@@@@@@@@@@@@@@@@@
```

Figure 4.2: Lines in the ZEUS-3D code where the appropriate component of the $\eta \boldsymbol{j}$ is subtracted from the EMF1.

## 4.1 Magnetic jet from accretion disk

We investigated the jet launched from a resistive, turbulent accretion disk around a young stellar object. One may expect that the turbulence pattern in the disk may also enter the disk corona, and that the jet flow itself is subject to a turbulent diffusion. A sketch of the model is given in Fig. 4.1. In this chapter the accretion disk is taken as a boundary condition. i.e. the disk evolution is not considered. This model setup is similar to the models in OP97 and FE00, with the difference that here the effect of magnetic diffusion for the jet formation is taken into account. The equations of the resistive MHD are solved using the ZEUS-3D code in the axisymmetry option.

### 4.1.1 Resistive MHD simulations

In the original version of ZEUS-3D the magnetic diffusivity is not included, so we included it and performed the tests - these are presented in the Appendix of Fendt & Čemeljić (2002), which is copied in the Appendix of this thesis.

As noted in Hawley & Stone (1995), addition of a magnetic diffusivity $\eta$ in ZEUS-3D can be accomplished by subtracting $\eta \boldsymbol{j}$ from the appropriate EMFs. The resistive timescale also must be properly included in the code (Fleming et al. 2000). In Fig.4.2 shown is the part of the code with the changed component of the EMF. This means that instead of equations (2.21), (2.22) and (2.23) we have:

$$\rho\left[\frac{\partial \boldsymbol{u}}{\partial t}+(\boldsymbol{u}\cdot\nabla)\,\boldsymbol{u}\right]+\nabla(p+p_A)+\rho\nabla\Phi-\frac{\boldsymbol{j}\times\boldsymbol{B}}{c}=0 \tag{4.1}$$

$$\frac{\partial \boldsymbol{B}}{\partial t}-\nabla\times\left(\boldsymbol{u}\times\boldsymbol{B}-\frac{4\pi}{c}\eta\boldsymbol{j}\right)=0 \tag{4.2}$$

$$\rho\left[\frac{\partial e}{\partial t}+(\boldsymbol{u}\cdot\nabla)\,e\right]+(p+p_A)(\nabla\cdot\boldsymbol{u})-\frac{4\pi}{c^2}\eta\boldsymbol{j}^2=0\,. \tag{4.3}$$

As pointed out in §2.3, we do not solve the energy equation, but prescribe the internal energy by the Eq.(2.24). The simplification of not-solving the energy equation is not expected to affect the results, as the resistive term in the energy equation enters with the factor $1/c^2$ (see also Miller & Stone 1997), and is negligible.

Additional to the hydrostatic pressure $p$, an Alfvénic turbulent pressure

$$p_{\mathrm{A}}\equiv p/\beta_{\mathrm{T}},\ \text{with}\ \beta_{\mathrm{T}}=\mathrm{const}$$

is included in the equations for our simulations (see OP97, FE00, Fendt & Čemeljić 2002). Here $\beta_{\mathrm{T}}$ is the beta plasma parameter for the turbulent fluid. The Alfvénic turbulent pressure $p_{\mathrm{A}}=|\delta\boldsymbol{B}|^2/8\pi$ can be estimated from the time-average of a fluctuating Lorentz force $(\nabla\times\delta\boldsymbol{B})\times\delta\boldsymbol{B}/4\pi$. Such disturbances propagate adiabatically, conserving the wave action (Dewar 1970). A radiation stress on the background fluid behaves as an isotropic wave pressure $p_{\mathrm{A}}$.

The Alfvén waves from the highly turbulent accretion disk are expected to propagate into the disk corona, providing the perturbations for turbulent motion also in the jet. Additional Alfvénic turbulent pressure could support the *cold* corona above a protostellar accretion disk, as suggested by the observations (OP97).

## Normalization in the code

The ZEUS-3D code solves the MHD equations in a dimensionless form. The variables normalize the system of equations and boundary conditions to their value measured at the inner disk radius $R_{\mathrm{i}}$. Therefore, $R'=R/R_{\mathrm{i}}$, $z'=z/R_{\mathrm{i}}$, and the time is measured in units of a Keplerian rotation at the inner disk radius. This gives $t_{\mathrm{i}}=R_{\mathrm{i}}/u_{\mathrm{K,i}}$, with a dimensionless time $\tau=t/t_{\mathrm{i}}=tu_{\mathrm{K,i}}/R_{\mathrm{i}}$. Here $u_{\mathrm{K,i}}=\sqrt{GM/R_{\mathrm{i}}}$ is the Keplerian speed at the inner boundary of the disk. The number of rotations of the disk also refers to the disk inner radius. As we choose $R_{\mathrm{i}}$=1 and $u_{\mathrm{K,i}}$=1, in our normalization $GM$=1.

The dimensionless equation of motion is

$$\frac{\partial \boldsymbol{u}'}{\partial\tau}+(\boldsymbol{u}'\cdot\nabla')\,\boldsymbol{u}'=\frac{2\,\boldsymbol{j}'\times\boldsymbol{B}'}{\delta_{\mathrm{i}}\,\beta_{\mathrm{i}}\,\rho'}-\frac{\nabla'(p'+p'_{\mathrm{A}})}{\delta_{\mathrm{i}}\,\rho'}-\nabla'\Phi'\,, \tag{4.4}$$

with $\nabla'=R_{\mathrm{i}}\nabla$, $\rho'=\rho/\rho_{\mathrm{i}}$, $\boldsymbol{B}'=\boldsymbol{B}/\boldsymbol{B}_{\mathrm{i}}$ and $\Phi'=-1/\sqrt{R'^2+z'^2}$.

Table 4.1: The scaling units for the jets. Adopted from OP97.

| OBJECT | $R_{\rm i}$ | $u_{\rm K,i}$ km/s | $t_{\rm i} \equiv \frac{1}{\Omega_{\rm K,i}}$ (days) |
|---|---|---|---|
| YSOs | $3R_*$ | $104\sqrt{\frac{M/0.5M_\odot}{R_{\rm i}/0.05AU}}$ | $0.86\frac{(R_{\rm i}/0.05AU)^{3/2}}{\sqrt{M/0.5M_\odot}}$ |
| AGN (pc) | $10R_{\rm g}$=$10^{-4} * M/(10^8 M_\odot)$ | $6.7 \times 10^4\sqrt{\frac{10R_{\rm g}}{R_{\rm i}}}$ | $0.53 \times \left(\frac{M}{10^8 M_\odot}\right)\left(\frac{10R_{\rm g}}{R_{\rm i}}\right)^{3/2}$ |

Table 4.2: An example of usual values. Adopted from OP97.

| OBJECT | Mass ($M_\odot$) | $R_{\rm i}$ (AU) | $u_{\rm K,i}$ (km/s) | t (days) |
|---|---|---|---|---|
| Protostar | 0.5 | 0.04 | 120 | 0.6 |
| Black hole | $10^8$ | 20.6 | $6.7\times 10^4$ | 0.53 |

Further in this chapter primes will be omitted when we refer to the equations actually solved in numerical simulations.

The free parameter $\beta_{\rm i} \equiv 8\pi p_{\rm i}/B_{\rm i}^2$ is the plasma-$\beta$ of the rotating gas, and the gas Mach number $\delta_{\rm i} \equiv \rho_{\rm i} u_{\rm K,i}^2/p_{\rm i}$ is also a free parameter in the simulations.

As we use a dimensionless form of the MHD equations, the physical quantities are given in units of their values at the inner radius of the accretion disk $R_{\rm i}$, and we may scale our results to a central object of any mass. The table 4.1 presents the table of units for the case of protostellar (YSOs) objects and active galactic nuclei (AGN). $R_{\rm g} = 2GM/c^2$ is the Schwarzschild radius, and within the fiducial radius $10R_{\rm g}$ relativistic effects can be neglected. In the Table 4.2 presented is an example.

### 4.1.2 Initial and boundary conditions

In Fig. 4.3 shown is the computational box in our simulations. The disk is prescribed as a fixed, time-independent boundary condition for the jet. It is in the centrifugal balance and penetrated by a force-free magnetic field, defined by the current-free potential field configuration of the $\phi$-component of the vector potential,

$$A_\phi = \frac{\sqrt{R^2 + (z_{\rm d} + z)^2} - (z_{\rm d} + z)}{R} \; .$$

For this vector potential it is

$$B_R = -\frac{\partial A_\phi}{\partial z} = \frac{1}{R}\left(1 - \frac{z_d + z}{\sqrt{R^2 + (z_d + z)^2}}\right)^{1/2}$$

$$B_z = \frac{1}{R}\frac{\partial(RA_\phi)}{\partial z} = \frac{1}{\sqrt{R^2 + (z_d + z)^2}} \; .$$

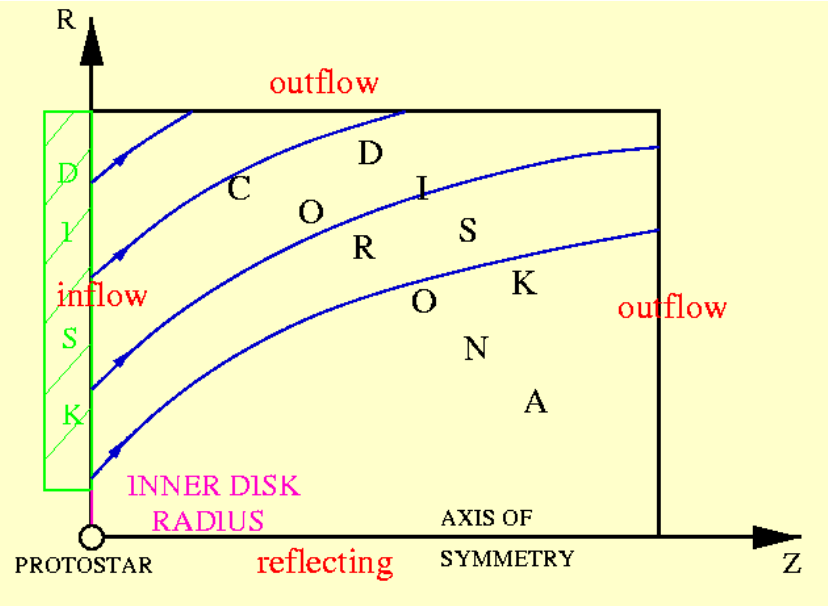

Figure 4.3: Computational box in the simulations. An initial poloidal magnetic field threads the disk corona. The disk is a boundary condition, with the “inflow” boundary condition defined at its surface.

The dimensionless disk thickness $z_{\rm d}$ satisfying $(z_{\rm d}+z)>0$ for $z<0$ is introduced. The initial coronal density distribution is in a hydrostatic equilibrium, $\rho=(R^2+z^2)^{-3/4}$. The initial corona is defined by two free parameters, $\delta_{\rm i}$ and $\beta_{\rm i}$. The total pressure we assumed to be composed of the *thermal* and *Alfvénic turbulent* terms,

$$p \rightarrow p + p_{\rm A}\ .$$

For the thermal atmosphere in a hydrostatic equilibrium (see §3.3.1 in OP97), the gravity is balanced by the gas pressure, and the momentum equation (4.1) is, for the force-free configuration in the initial setup, reduced to:

$$\frac{\nabla(p+p_{\rm A})}{\rho}+\nabla\Phi=0\ .$$

With $h=\gamma p/(\gamma-1)\rho$ as the dimensionless enthalpy we can write, now in the dimensionless form, following from the Eq. (4.4):

$$\frac{h}{\delta_{\rm i}}+\Phi=const\ . \qquad (4.5)$$

With $\Phi_\infty=0$ and $\rho=\rho_\infty$

$$\rho=\left[\frac{\gamma-1}{\gamma}\frac{GM\delta_{\rm i}}{\sqrt{R^2+z^2}}+\rho_\infty^{\gamma-1}\right]^{1/(\gamma-1)}$$

and for $\rho=\rho_{\rm i}$ at $R=R_{\rm i}$ and $GM$=1 we obtain the constraint

$$\delta_{\rm i}=\frac{\gamma}{\gamma-1}(1-\rho_\infty^{\gamma-1})\ \Rightarrow\ \delta_{\rm i}=\frac{\gamma}{\gamma-1}=\frac{5}{2}=\frac{u_{\rm K,i}^2}{p_{\rm i}/\rho_{\rm i}}\ ,\ \text{for}\ \gamma=\frac{5}{3}\ . \qquad (4.6)$$

This value is too small for the *cold* corona case (OP97), and besides the thermal pressure an additional term is needed to provide the equilibrium (see §4.1.1 here). The *effective* enthalpy is, with $\beta_{\rm T} = c_{\rm s}^2/u_{\rm T}^2$,

$$h_{\rm eff} = (c_{\rm s}^2 + u_{\rm T}^2) = \left(1 + \frac{1}{\beta_{\rm T}}\right) c_{\rm s}^2 \ ,$$

and the equilibrium equation is the same as Eg. (4.5) with $h = h_{\rm eff}$. The corresponding Alfvén turbulence velocity $u_{\rm T} = \delta \boldsymbol{B}/\sqrt{4\pi\rho}$. The solution is

$$\rho = \left[\frac{\gamma - 1}{\gamma} \frac{GM}{\sqrt{R^2 + z^2}} \frac{\delta_{\rm i}}{1 + \frac{1}{\beta_{\rm T}}} + \rho_\infty^{\gamma-1}\right]^{1/(\gamma-1)} .$$

For $\rho_\infty = 0$ and $GM$=1 we obtain

$$\beta_{\rm T} = \left(\frac{\gamma - 1}{\gamma}\delta_{\rm i} - 1\right)^{-1} . \qquad (4.7)$$

The disk as a boundary condition is time-independent, i.e. the initial potential field magnetic flux from the disk is considered. The toroidal component of the magnetic field in the ghost zones ($z < 0$) is chosen as $B_\phi(z < 0) = \mu_{\rm i}/R$, where $\mu_{\rm i}$ is another free parameter. The mass flow rate from the disk surface into the corona is defined by the injection velocity and the density of the injected material. With the launching angle $\Theta_0(R, z = 0)$, which is measured from the jet axis (see Fig. 4.4), the velocity field in the ghost zone is $\boldsymbol{u} = (u_R, u_\phi, u_z) = u_{\rm inj}(u_{\rm p}\sin\Theta_0, u_{\rm K}, u_{\rm p}\cos\Theta_0)$ for $R \geq 1$, with $u_{\rm inj}$ as a free parameter.

In the second part of §3.1.1 is given an analytical derivation for the Blandford & Payne critical angle at which the matter could leave the disk surface by action of the centrifugal force. Our setup for the launching angle is chosen to match it.

For $R \leq 1$ the inflow velocity is set to zero; this defines the inner edge of the disk. The inflow density is given as $\rho_{\rm d} = \kappa_{\rm i} R^{-3/2}$, with $\kappa_{\rm i}$ as a free parameter. The disk in our setup is an "inflow"boundary condition (see §2.3 for the definitions of the boundary conditions). In the ghost zones, which do not change in time, the values of all the variables are prescribed.

The symmetry axis is set with a "reflecting" boundary condition, and along two remaining boundaries an "outflow" condition is set. The flow is extrapolated beyond the boundary i.e. in the ghost zones all the variables are set equal to the values in the corresponding active zones.

Fig. 4.5 shows the initial setup of a hydrostatic density distribution together with the potential magnetic field for the part of the computational box close to the origin (the region of the "inner jet"). The free parameters in the simulations are: $\delta_{\rm i}$=100, $\kappa_{\rm i}$=100, $\mu_{\rm i}$=-1.0, and $u_{\rm inj}$=0.001. The choice is by OP97 and FE00 for reasons of comparison. For the plasma-$\beta$ we chose $\beta_{\rm i}$=0.282 (similar to OP97[1]) or a lower value $\beta_{\rm i}$=0.141

---

[1] See also Appendix A in FE00. The factor $\sqrt{4\pi}$ appears because of the choice of $B_{\rm i}'$=$B_{\rm i}\sqrt{4\pi}$, which is necessary if we are to write $\beta_{\rm i}$ in a form corresponding to the plasma $\beta$.

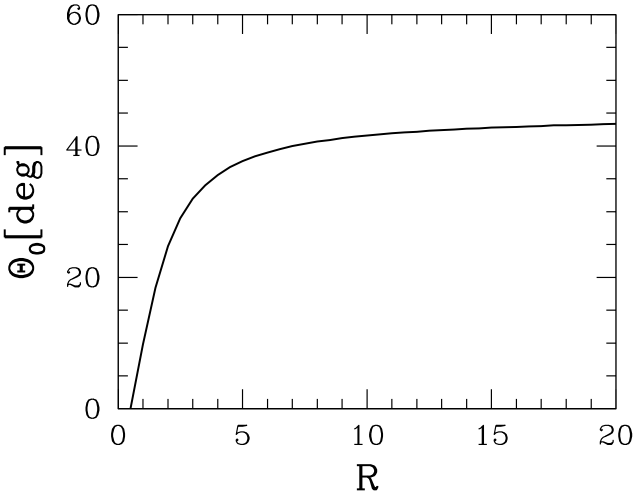

Figure 4.4: The launching angle at the disk surface, measured from the jet axis.

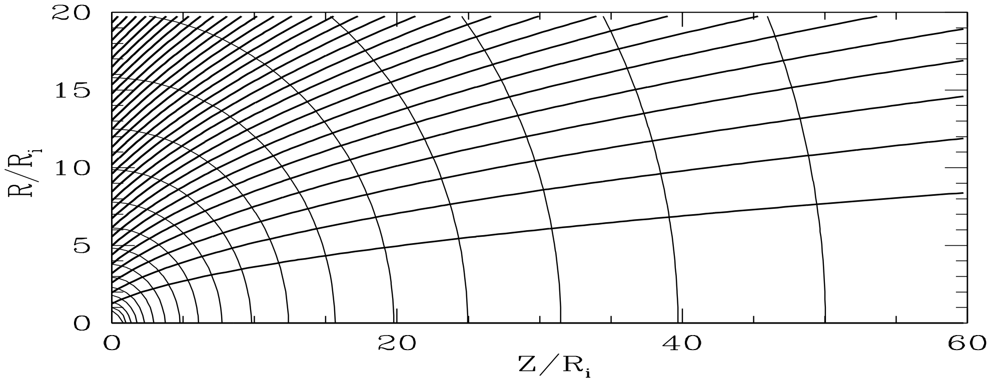

Figure 4.5: Initial setup for the jet simulation. Shown is the part of the computational box close to the origin (the "inner jet"). The initial hydrostatic density distribution is indicated by *thin* concentric isocontours. *Thick* lines denote the initial poloidal field lines of a force-free potential field.

which has some numerical advantages. The lower $\beta_\mathrm{i}$ does not change the general behavior of the jet. The jet evolution is faster and the Alfvén surface is slightly shifted in the $z$-direction, but the jet structure remains similar. For a constant parameter $\beta_\mathrm{T}$, which measures the ratio of the thermal to the MHD turbulent velocities in the corona (see above), $p_\mathrm{A}$ scales with the gas pressure. Solution of the equilibrium equation implies Eq. (4.7), i.e. $\beta_\mathrm{T}$=0.03.

### 4.1.3 Turbulent magnetic diffusivity

If we chose the turbulent velocity field $u_{\rm T}$ instead of the local Alfvén speed as a typical velocity for the turbulent diffusivity, it is possible to define a turbulent magnetic diffusivity $\eta_{\rm T}$,

$$\eta_{\rm T} = \alpha_{\rm m} u_{\rm T} L \; . \tag{4.8}$$

With $\beta_{\rm T} \equiv (c_{\rm s}/u_{\rm T})^2$ and $c_{\rm s}^2 = \gamma p/\rho$ for an adiabatic or polytropic gas law, we can write

$$u_{\rm T}^2 = \frac{\gamma}{\beta_{\rm T}} \frac{p}{\rho}.$$

In the normalized equations it is

$$u'^2_{\rm T} = \frac{p'}{\rho'} \frac{c_{\rm s,i}^2}{u_{\rm K,i}^2} \frac{1}{\beta_{\rm T}}, \qquad \text{or} \qquad u'^2_{\rm T} = \rho'^{\gamma-1} \frac{\gamma}{\delta_{\rm i}\beta_{\rm T}}. \tag{4.9}$$

For our values $\beta_{\rm T}$=0.03 and $\delta_{\rm i}$ $\simeq$100, with a typical value for the normalized density $\rho' \simeq 10^{-2}$, the normalized magnetic diffusivity is

$$\eta' \simeq 0.015 \left(\frac{\alpha_{\rm m}}{0.1}\right) \left(\frac{L'}{1.0}\right) .$$

The diffusivity changes only weakly with the density, $\eta \sim \rho^{1/3}$, and this is a good estimate for the magnetic diffusion.

We introduced and tested the magnetic diffusivity in ZEUS-3D (see §4.1.1). A self-consistent simulation would include a relation between the diffusion and density as in equation (4.9). For simplicity, in the simulations presented here, $\eta = const$. For a comparison, the simulations with $\eta \sim \rho^{1/3}$ setup were run, and no significant difference has been observed.

## 4.2 Computational grid

As already mentioned in §2.3, the numerical mesh of ZEUS-3D is a staggered grid, where different physical quantities are defined in a different grid positions. One reference set of global simulations we performed with the high resolution runs. The numerical mesh was $(900 \times 200)$ grid points, in the domain (z×R)=(280×40)R$_{\rm i}$.

In order to investigate the effects which concern only the gross behavior of the jet flow and not its structure in detail, another set of simulations with lower resolution has been done. There the numerical mesh was (280×80) grid points, in the domain (z×R)=(140×40)R$_{\rm i}$.

These lower resolution simulations (with the computational domain for a factor 2 shorter in the direction of propagation) were much faster to compute, and allowed to follow the jet evolution for a very long time (up to 4000 disk rotations), even in the case of a high magnetic diffusivity. All other parameters were the same as for the high resolution runs.

There were some numerical artifacts (a spurious velocity pattern) in the corners of the grid where the outflow boundary conditions interacts with the other (inflow, reflecting) boundary conditions, but as we mainly concentrate on the inner part of the jet flow, the results are not affected by these effects.

## 4.3 The jet evolution

We performed the simulations with different numerical resolutions, and topics of interest were:

**i)** The “global jet”, in domains of different physical size in order to investigate the influence of boundaries and to obtain an information about the large-scale flow, and

**ii)** The “inner jet”, where we investigated the inner substructure of the global jet, close to the jet axis and the accretion disk.

We were interested in the case of a typical MHD jet flow starting as a sub-Alfvénic (but super-slow magnetosonic) flow from the disk surface, being accelerated to super-Alfvénic and super-fast magnetosonic speed. There exists another case, where matter is injected into the disk corona already with super-Alfvénic speed. It applies for a relatively weak disk poloidal magnetic field, as for example in the case of a central dipolar field with a strong gradient in a radial direction. These winds are initially driven by the (toroidal) magnetic field pressure gradient in a vertical direction (Lovelace et al. 1987; Contopoulos 1994; FE00).

A position of the Alfvén surface changes until the quasi-stationary state (see below) is reached. This surface may advance into the disk for small radii, and the character of the MHD flow is then changed. For a smaller than moderate magnetic diffusivity ($\eta < 0.5$), the location of the Alfvén surface is always within the active zones, well above the accretion disk boundary. The initially super-Alfvénic jets we do not consider here (see Contopoulos 1995b).

The different speed of the large-scale flows with and without the magnetic diffusion included is shown in Fig. 4.6. With increasing diffusivity, the bow shock propagates slower. Before the build-up of the bow shock, the disk corona hydrostatic equilibrium is slightly modified by the propagation of the torsional Alfvén wave from the disk surface. Behind the bow shock, there remains a cavity with dilute density and high velocity. The toroidal magnetic field is initially generated due to the differential rotation between the rotating disk and the static corona, but later it is due to the inertial forces of the matter in the MHD flow. The internal structure of the jet behind the bow

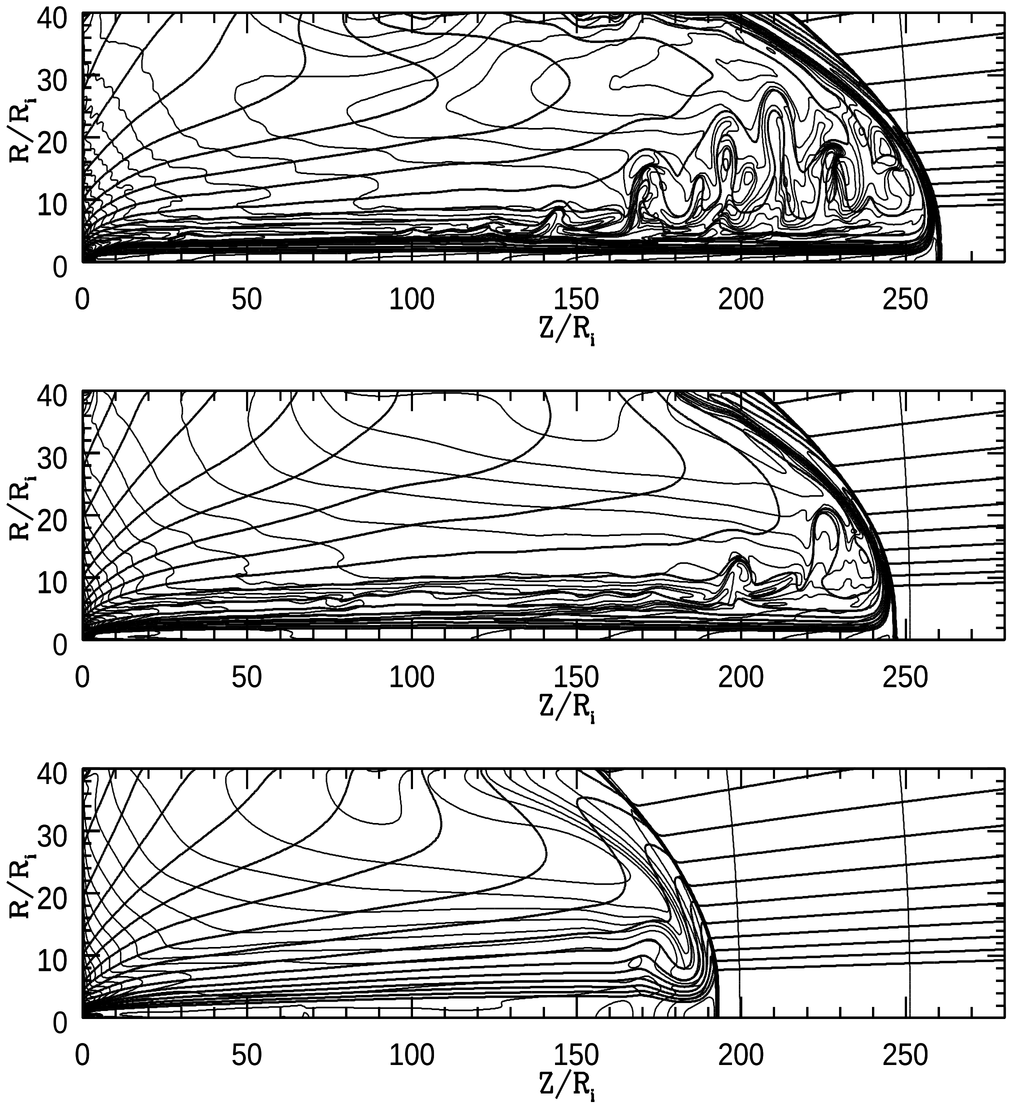

Figure 4.6: Global evolution of the jet in the domain ($Z \times R$)=(280× 40)$R_{\rm i}$ with a resolution of (900×200) grid elements. Shown is the state of evolution after $t$=400 rotations of the disk inner radius for different magnetic diffusivity, $\eta$=0 (*top*), $\eta$=0.01 (*middle*), and $\eta$=0.1 (*bottom*). *Thin* lines denote 30 logarithmically spaced isocontours of density. *Thick* lines denote 20 linearly spaced magnetic flux surfaces (or poloidal field lines). The parameters are $\delta_{\rm i}$=100, $\kappa_{\rm i}$=100, $\mu_{\rm i}$=-1.0, $\beta_{\rm i}$=0.282, and $u_{\rm inj}$=0.001. Note the preserved initial hydrostatic density and force-free field distribution in front of the bow shock. The figure demonstrates that the bow shock advances slower with increasing diffusivity.

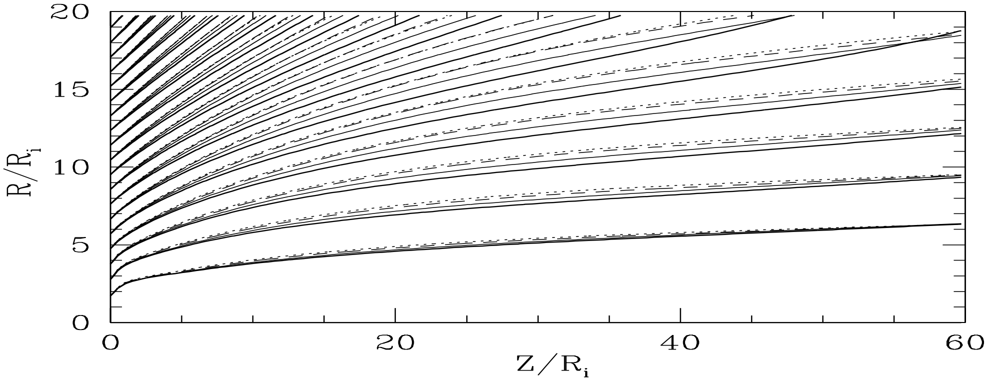

Figure 4.7: The evolution of the inner jet approaches the quasi-stationary state. Shown are poloidal magnetic field lines in the case of $\eta$=0.1 for different time steps, $t$=250,300,350,400 (*thick solid, thin solid, dashed* and *dotted* lines). The same setup as in the simulation in Fig. 4.6, except that now $\beta_\mathrm{i}$=0.141. The grid size is $(280 \times 80)$ grid elements in the domain (140× 40)$R_\mathrm{i}$. The picture shows how the poloidal magnetic field lines diffuse outwards but approach a (quasi)-stationary state after 400 rotations (see the dashed and dotted lines almost coinciding).

shock is smoother for a diffusive jet. The “wiggles”, which seem to be a numerical artifact for $\eta$=0, are also less prominent.

The pattern inside the jet, the blobs or *knots*, which is most prominent in the ideal-MHD jet, is not connected with the jet knots observed in protostellar jets. The size of these “knots” is about the inner disk radius, and depends from the numerical resolution and the mass inflow condition. The time scale of knot formation in our simulations, as it is for similar structures in OP97, Goodson et al. (1997; 1999) and Goodson & Winglee (1999), also supports the conclusion that they are purely numerical effect. For the resistive jets, this structure is significantly smoothed already for a low magnetic diffusivity.

### 4.3.1 Evolution of the inner jet

Now we will discuss the evolution of the inner substructure of the global jet close to the jet axis and the accretion disk. The size of the “inner jet” domain is $(60 \times 20) R_\mathrm{i}$. This part of the jet is chosen as not influenced from any outflow boundary condition or the jet evolution in a global scale. As a major part of the global jet is super fast-magnetosonic, there is no physical way to transport an information from this part in upstream direction into the inner jet.

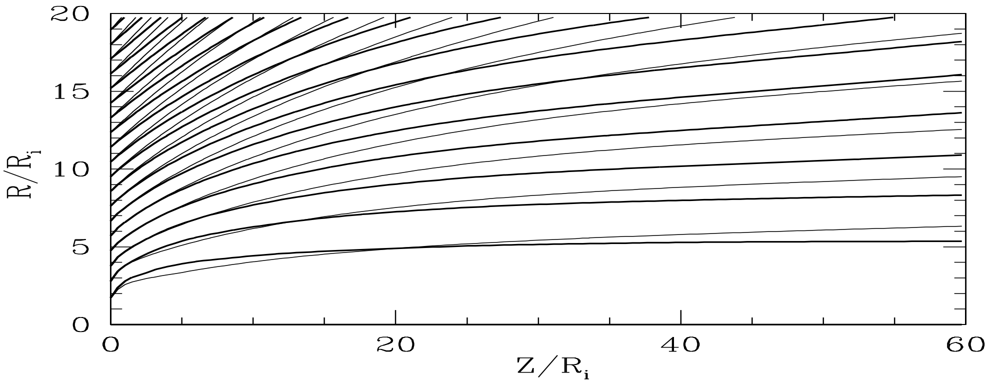

Figure 4.8: The de-collimation of the stationary state poloidal magnetic field due to magnetic diffusivity. The same setup as in Fig. 4.7. The lines represent the poloidal magnetic field line distribution of the inner jet in the state of quasi-stationarity ($t = 400$), for vanishing diffusivity $\eta = 0$ (*thick*) and for $\eta = 0.1$ (*thin*).

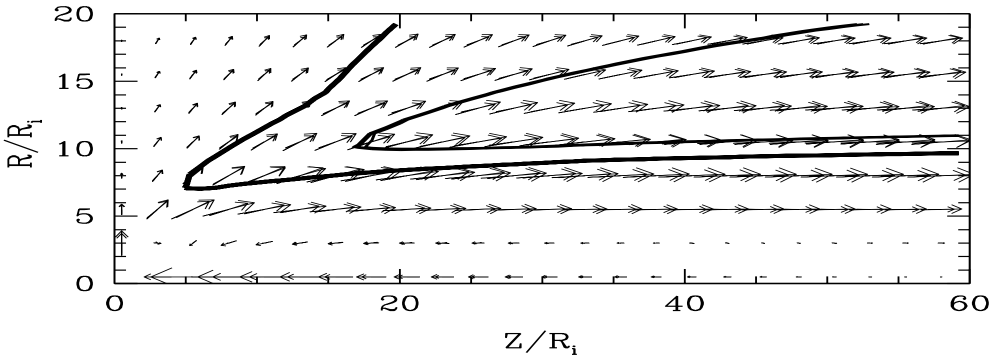

Figure 4.9: Comparison of the poloidal velocity vectors. Shown are the poloidal velocity vectors at the time of quasi-stationarity. Over-plot of the velocity field for the $\eta$=0 simulation at $t$=350 with the $\eta$=0.1 simulation at $t$=400. The de-collimation visible in the poloidal magnetic field lines (see Fig. 4.8) is *not* present here. The *thick* line indicates the Alfvén surface for $\eta$=0.1, and the *thin* line the fast-magnetosonic surface.

### 4.3.2 Quasi-stationarity of inner jet

Fig. 4.8 shows an over-plot of the poloidal magnetic field lines resulting from the simulations at the time steps of $t = 250, 300, 350, 400$ disk rotations, respectively, in the case of relatively large magnetic diffusion $\eta$=0.1. The field lines first diffuse outwards and then, after hundreds of rotations, the field distribution approaches the quasi-stationary state.

The outflow evolved into a stationary state after several hundreds of disk rotations, close to the disk surface. Such a stationary state is denoted as *quasi-stationary* - as the

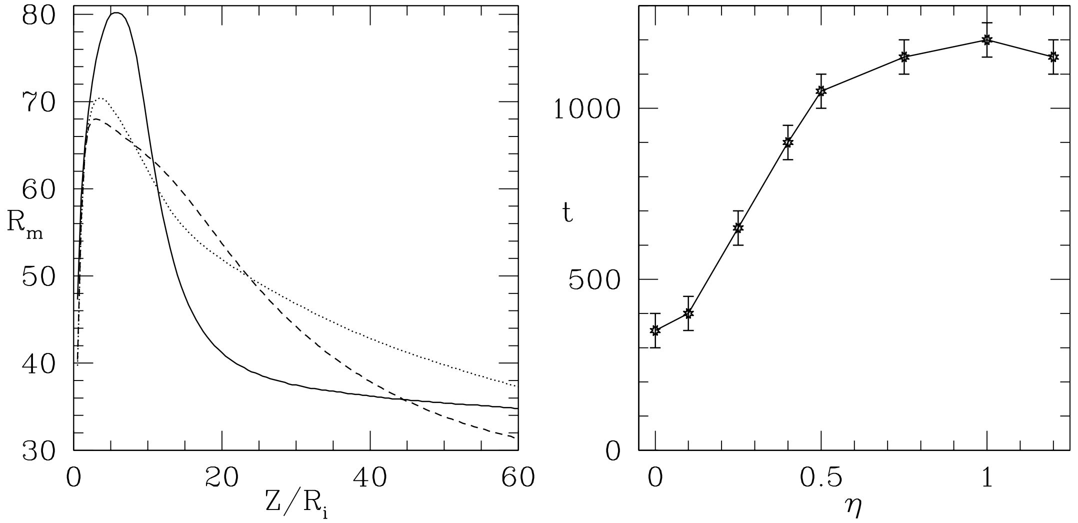

Figure 4.10: Magnetic diffusivity and global time scales. *Left* Global magnetic Reynolds number as defined from the scale of the computational box of the inner jet $L = 20, U = U_A$. Shown is the $R_m$-profile along slices in $z$-direction at $R = 7, 13, 20$ (*solid, dotted, dashed* line, respectively), for the simulation run with $\eta = 0.1$, $\beta_i = 0.141$. The plots basically shows the variation of the typical velocity $U$, for which the local Alfvén speed is chosen. *Right* The time of stationarity. This plot shows, for different magnetic diffusivity, the time period when the inner jet reaches a quasi-stationary state. This time is estimated from the evolution of the poloidal magnetic field lines (see Fig. 4.8) and the error bars indicate our uncertainty.

outer regions surrounding this inner jet flow still evolve in time. Existence of such a state gives the possibility for investigation of the internal forces acting in the jet, since the equations of stationary ideal MHD and its conservation laws may be used for the interpretation of a jet flow.

In the case of an ideal MHD jet a stationary state of the inner jet is reached after approximately $t$=350 disk rotations. For a resistive jet this can be quite different, and it also depends on the plasma-beta parameter $\beta_i$. In fact, the existence of such quasi-stationary state is not necessarily expected in the computations with the magnetic diffusion included. The magnetic field could just decay forever. However, in the setup as presented, for the magnetic diffusion vanishing or not, we have an energy reservoir established constantly by the disk rotation and accretion, and eventually by the gravitational potential of the central star. A loss of magnetic energy in the jet can be replenished by the constant Poynting flux rising from the disk. This mechanism works in the case of an ideal MHD jet (where the jet carries the energy out of the computational box), and the additional effect due to magnetic diffusivity is small compared to the total energy flow in the jet.

In general, our simulations show that with increasing $\eta$ the flow reaches the quasi-stationary state at a *later* time. For a smaller than moderate magnetic diffusivity ($\eta \leq 0.5$), we find an approximately linear relation between this time and the diffusivity (Fig. 4.10).

Table 4.3: The typical numbers for our simulations for a different magnetic diffusivity $\eta$. The diffusive time step $\tau_\eta$, Alfvén time step $\tau_{\rm A}$, the global magnetic Reynolds number $R_{\rm m}$ and the magnetic turbulence parameter $\alpha_{\rm m}$.

| $\eta$ | $\tau_\eta$ | $\tau_{\rm A}$ | $R_{\rm m}$ | $\alpha_m$ |
|---|---|---|---|---|
| 0 | $\infty$ | 0.258 | $\infty$ | 0 |
| 0.1 | 0.625 | 0.293 | 40 | 0.025 |
| 0.15 | 0.417 | 0.084 | 30 | 0.033 |
| 0.25 | 0.25 | 0.136 | 20 | 0.05 |
| 0.5 | 0.125 | 0.080 | 10 | 0.1 |
| 1 | 0.063 | 0.183 | 8 | 0.125 |
| 2.5 | 0.025 | 1.394 | 4 | 0.25 |

For higher diffusivity then $\eta$=0.5, the Alfvén surface has been advanced into the disk for small radii and the MHD flow was already initially super-Alfvénic. However, we showed here the time of quasi-stationary state for these cases too, for completeness. In Fig. 4.10 is plotted the variation of the magnetic Reynolds number $R_{\rm m}$ along the jet in the case $\eta = 0.1$. As $R_{\rm m}$ does not change along the jet by more than a factor of two (this is similar for other diffusivity), this value provides a good estimate for the global jet dynamical behavior.

For the time when the flow reached the quasi-stationary state, we table the local time step of the magnetic diffusion and the Alfvén time step, together with the global $R_{\rm m}$ and the related $\alpha_{\rm m}$. A "typical" value for the Alfvén speed within the grid of the inner jet could be chosen, because of the minor variation in $R_{\rm m}$.

In addition to the diffusive time scale, there are three other important initial timescales at the disk surface: the Kepler time $\tau_{\rm K}$, the Alfvén time $\tau_{\rm A}$ and the magnetic braking time $\tau_{\rm B}$[2].

$$\tau_{\rm K} = \min\left(\frac{R}{u_{\rm K}}\right) \ , \ \tau_{\rm A} = \min\left(\frac{t_{\rm A}}{t_{\rm i}}\right) = \min\left(\frac{R}{u_{\rm A}}\right)$$

$$\tau_{\rm B} = \min\left(\frac{t_{\rm B}}{t_{\rm i}}\right) = \min\left(\eta_{\rm i}\frac{R}{u_{\rm A0}}\right) = \eta_{\rm i} \times \tau_{\rm A} \ .$$

For these timescales in our simulations, with $\min(\tau_{\rm K})$=1 at R=1:

$$(\tau_{\rm K}, \tau_{\rm A}, \tau_{\rm B}) = (1, \sqrt{\delta_{\rm i}\beta_{\rm i}/2}, \eta_{\rm i}\sqrt{\delta_{\rm i}\beta_{\rm i}/2}) \ .$$

### 4.3.3 Jet velocity and collimation

The velocity and degree of collimation of a jet are directly observable quantities, and thus the most interesting.

---

[2] The time a torsional wave propagating into the ambient medium needs to traverse an amount of matter whose moment of inertia equals moment of inertia of the disk (Mouschovias & Paleologou 1980).

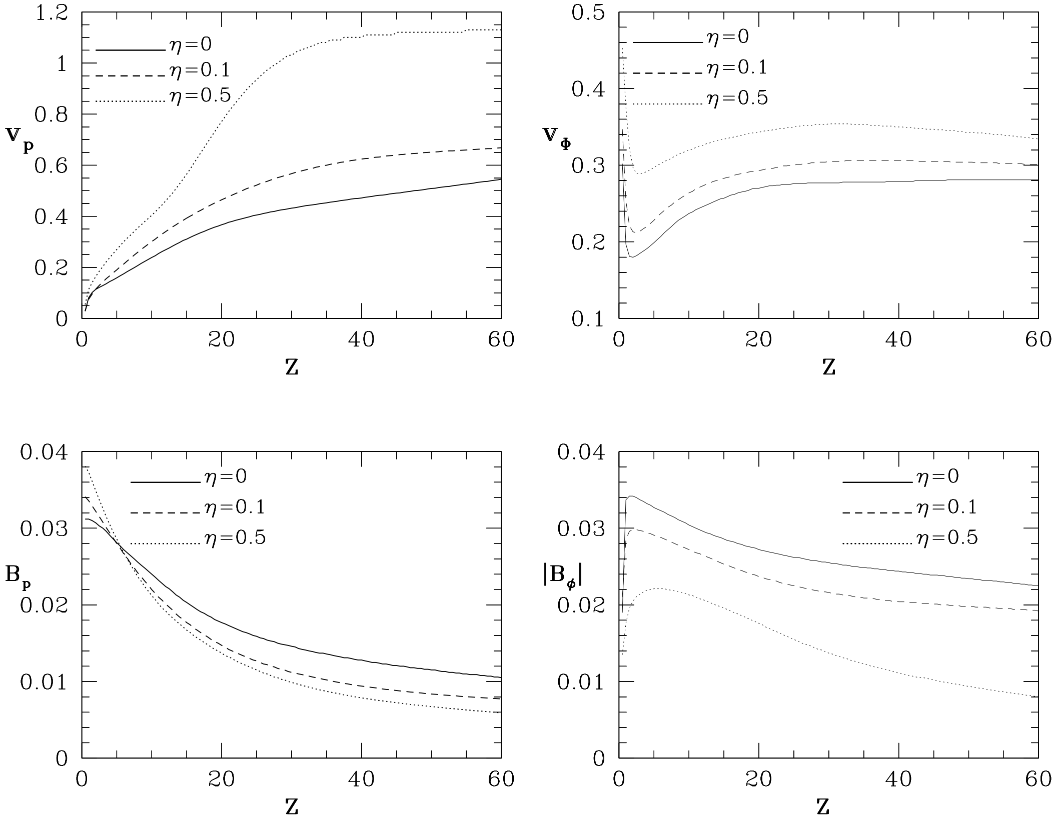

Figure 4.11: Variation of the jet velocity and magnetic field with different magnetic diffusivity, $\eta = 0$ (*solid*), $\eta = 0.1$ (*dashed*), $\eta = 0.5$ (*dotted*). Shown is the profile of the poloidal (*left*) and toroidal (*right*) components of the velocity (*top*) and the magnetic field (*bottom*) in $z$-direction at $R = 15$ at the time of quasi-stationarity. The velocity components increase, while the magnetic field strength decreases with increasing $\eta$ (except for the magnetic field just above the disk, see the end of present section). Note the different scales for $u_p$ and $u_\phi$. The boundary value for the toroidal velocity is the Keplerian value $u_\phi = 0.258$ at $R = 15$.

In Fig. 4.9 shown are the poloidal velocity vectors in the inner jet for $\eta = 0$ and $\eta = 0.1$. They are taken at time when the flow has reached the quasi-stationary state, and clearly show the self-collimating property of the MHD flow. The velocity vectors become more and more aligned with the jet axis along the flow, except for a region of low collimation close to the disk, where the velocity vectors point in radial direction (with $\simeq 45°$ half opening angle).

For very low magnetic diffusivity ($\eta < 0.05$) the apparent de-collimation of the poloidal magnetic field lines (Fig. 4.8), which is present for a weak magnetic diffusivity ($\eta = 0.01$), is not visible in the poloidal velocity (Fig. 4.9). The flow evolution has reached a quasi-stationary state in both cases at $t = 400$. This illustrates how, in contrast to the ideal MHD, in the case of diffusive MHD a miss-alignment between $u_{\rm p}$ and $B_{\rm p}$ is possible. Up to $\eta$=0.5 this mismatch between the poloidal velocity and magnetic field vector is weak for large $z$ and about $5° - 10°$ at small heights above the disk. We obtain a collimated flow along the axis, but the mass load distribution varies implying a variation of the mass flow rate through the $R$ and $z$-boundaries with $\eta$. For a larger magnetic diffusivity ($\eta > 0.1$), a de-collimation of the *mass flow* is also observed (see below).

Both the poloidal and toroidal velocity increase, and the magnetic field components decrease, with the increasing diffusivity. This is shown in Fig. 4.11, where the velocity and field components along the jet at a distance of $15R_{\rm i}$ from the jet axis are shown. A conclusion: matter in the diffusive jets is faster.

The decrease of the toroidal velocity just above the disk can be explained with the increasing of the toroidal field with height (see also Fig. 4 in OP97), and the larger slide of the matter along the field line. Namely, at some radius along the disk surface the strengths of the toroidal and poloidal magnetic fields equal, and as the matter is corotating with the field lines (foot points of which rotate with Keplerian speed), for the dominating poloidal component of the magnetic field, the toroidal velocity would *increase*. When the field components are equal, $B_\phi = B_{\rm p}$, the slide becomes larger.

The apparent non-matching of the magnetic field strength and the toroidal velocity with the given boundary condition in the resistive simulations is generated by the jump in diffusivity between the disk (in the ghost zones of the computational box) and the corona. When leaving the disk surface, the magnetic field lines are immediately affected by diffusion, and the magnetic field strength is changing.

### 4.3.4 Mass and momentum fluxes

The fluxes across the surfaces parallel to the accretion disk boundary can be defined by:

$$\dot{M} = \int_0^{R_{\rm max}} 2\pi R\rho u_{\rm z} dR \; , \quad \dot{M}u_{\rm z} = \int_0^{R_{\rm max}} 2\pi R\rho u_{\rm z}^2 dR \; . \tag{4.10}$$

These are the mass flux and the kinetic $z$-momentum (i.e. the momentum in $z$-direction) flux along the jet axis.

For the inner jet $R_{\rm max}$=20, and the integration is along $z_{\rm max}$=60. The flux away from the jet axis, in R-direction[3], is defined correspondingly by the integration along the $R_{\rm max}$-boundary from $z$=0 to $z$=$z_{\rm max}$. The corresponding flux into the jet has to be integrated along the $z = 0$ axis. This flux is prescribed by the disk boundary condition. When most of the mass and/or momentum flux in the computational box is directed along the jet axis, the jet is *collimated*. The time dependence of the mass and momentum fluxes for different diffusivity is shown in Fig. 4.12. The mass flux across $R$ and the $z$-*boundary* and the kinetic momentum flux in $R$ and the $z$-*direction* are integrated along the outflow boundaries. During the first $100 - 200$ rotations the fluxes are large, and the reason is that initially hydrostatic corona is exiting the grid of the *inner* jet.

---

[3] The momentum flux in $z$-direction across the $R_{\rm max}$-boundary is $\dot{M}u_{\rm z} = \int_0^{R_{\rm max}} 2\pi R\rho u_{\rm z} u_{\rm R} dR$

When the bow-shock leaves the inner grid, the mass flow in the jet is determined by the mass injection rate from the disk boundary condition.

The solid line (inflow condition) compared to the sum of the dotted (radial outflow) and the dashed lines (axial outflow), shows that the mass inflow from the disk boundary into the jet is equal to the mass loss across the boundaries in $R$- and the $z$-direction, as should be in the stationary state. The obtained result is in good agreement with the analytical result[4].

Similar analytical integration for the momentum flux gives a momentum flux from the disk into the jet of $\dot{M}u_{\mathrm{z}}$=$1.8 \times 10^{-4}$. This is much below the numerical value at the first active zone, and reason is that the momentum flux is not conserved as the matter becomes accelerated in the jet, because of gain of kinetic energy of the MHD flow.

The kinetic momentum flux in $z$-direction across the $z$=$z_{\mathrm{max}}$ boundary can be well estimated by the integrated mass flow rate $\dot{M}$ multiplied by the mean $u_{\mathrm{z}}$-velocity at this position. Negligible kinetic momentum flux in $R$-direction is leaving the inner box across the $z$-outflow boundary for the $\eta$=0 case (as $\dot{M}u_{\mathrm{z}} \simeq 1.5 \times 0.6$=0.9), similar to the result from our simulations.

In Fig. 4.12 presented is the run with $\eta$=0.5. A mass inflow rate in dimensionless units is 1.5, and the mass loss rate across the computational grid boundaries in $z$-direction is about 0.45 and 1.05 in $R$-direction. For the vanishing diffusivity, where about 70% of the mass flow leaves the box in $z$-direction, the mass flow for $\eta$=0.5 is less collimated[5]. For the simulations with higher diffusivity $\eta = 1.0$, when the mass injection from the disk boundary is partly super-Alfvénic, the mass flow is even less collimated, but as already commented, it is another physical sytuation.

A conclusion concerning the velocity vectors: even if they can have similar directions for the diffusivity up to $\eta$=0.5, the mass load along the stream lines can actually be different. This is due to the fact that centrifugal forces may drive the matter outwards across the magnetic field lines (because of the magnetic diffusion), enhancing the mass flow rate in a radial direction.

As already pointed out, for the degree of jet collimation defined by the mass flux across the jet boundaries, there exists a *critical value* $\eta_{\mathrm{cr}}$ of the magnetic diffusivity (see Figs. 4.12 and 4.13). In Fig. 4.13 the ratio of the mass flux leaving the grid in $z$-direction to that in $R$-direction is shown for different diffusivity for a time when the bow shock has left the inner box. For a high diffusivity ($\eta_{\mathrm{cr}} \simeq 0.3$, but the actual value depends on the plasma beta $\beta_{\mathrm{i}}$, too) that ratio becomes *less* than unity, i.e. the mass flow is weakly collimated.

If we consider the momentum flux, the picture is somewhat different, as the momentum flux in $z$-direction is *always* larger than that in $R$-direction. In our simulations a ratio

---

[4] The integrated inflow mass rate being $\dot{M}$=1.41.

[5] In support of this conclusion are also the recent results from the diffusive MHD simulations of the jet formation out of the accretion disk (Kuwabara et al. 2000), when the jet launching from the disk critically depended on the strength of diffusivity.

of the momentum fluxes in each direction is about 5 – 8. In other words, if the degree of collimation would be defined by the momentum fluxes, the jets would perfectly collimate also for higher diffusivity. This shows the big efficiency of conversion of the rotational kinetic energy into poloidal kinetic flux for a rotating MHD flows. But, the density distribution (i.e. the mass flow distribution) is, in our opinion, the best theoretical equivalent to the observed intensity, as long as there are no emission maps provided by the simulations.

## 4.4 Lorentz forces in the jet

How the jet internal structure is modified in our resistive MHD simulations by the effect of magnetic diffusivity, compared to the ideal MHD simulation (OP97)?

There are three main points:

(1) The poloidal magnetic field structure for any value of magnetic diffusivity is de-collimated;

(2) For a strong diffusion, the hydrodynamic flow is also de-collimated;

(3) The jet velocity increases with increasing diffusivity.

In the MHD simulation, as in real astrophysical flows, very complex physical effects combine (the pressure and gravity intertwined with the magnetic and inertial forces) and to make a distinction between their contributions is not straightforward. In the paradigm accepted here, the magnetic fields are the main driver for the flow acceleration and self-collimation, so investigation of the Lorentz forces in the quasi-stationary state should reveal the physical mechanism at work.

In Fig. 4.14 the results for different magnetic diffusivity are shown for the Lorentz force components ($F_{\mathrm{L},\perp}$, $F_{\mathrm{L},||}$, $F_{\mathrm{L},\phi}$). Also, computed are the corresponding accelerations ($F_{\mathrm{L}}/\rho$) along a field line (or, respectively, along the corresponding magnetic flux surface) leaving the numerical grid of the inner jet at ($R = 20, z = 60$)[6]. The foot points of these flux surfaces are between $R = 5$ and $R = 8$ along the disk surface and the Alfvén points are at about $z = 25, 15, 5$ (for $\eta$=0,0.1,0.5, respectively).

The magnitude of the Lorentz force in our simulations generally increases with increasing magnetic diffusivity, although the magnetic field strength *decreases* with increasing diffusivity (Fig. 4.11). The maximum Lorentz force is in that region *before* the Alfvén point where the curvature of the poloidal field is largest, i.e. the *magnetic acceleration* is the most important part of the mechanism here.

---

[6] Note that due to the magnetic field de-collimation with $\eta$, we compare *different* magnetic flux surfaces.

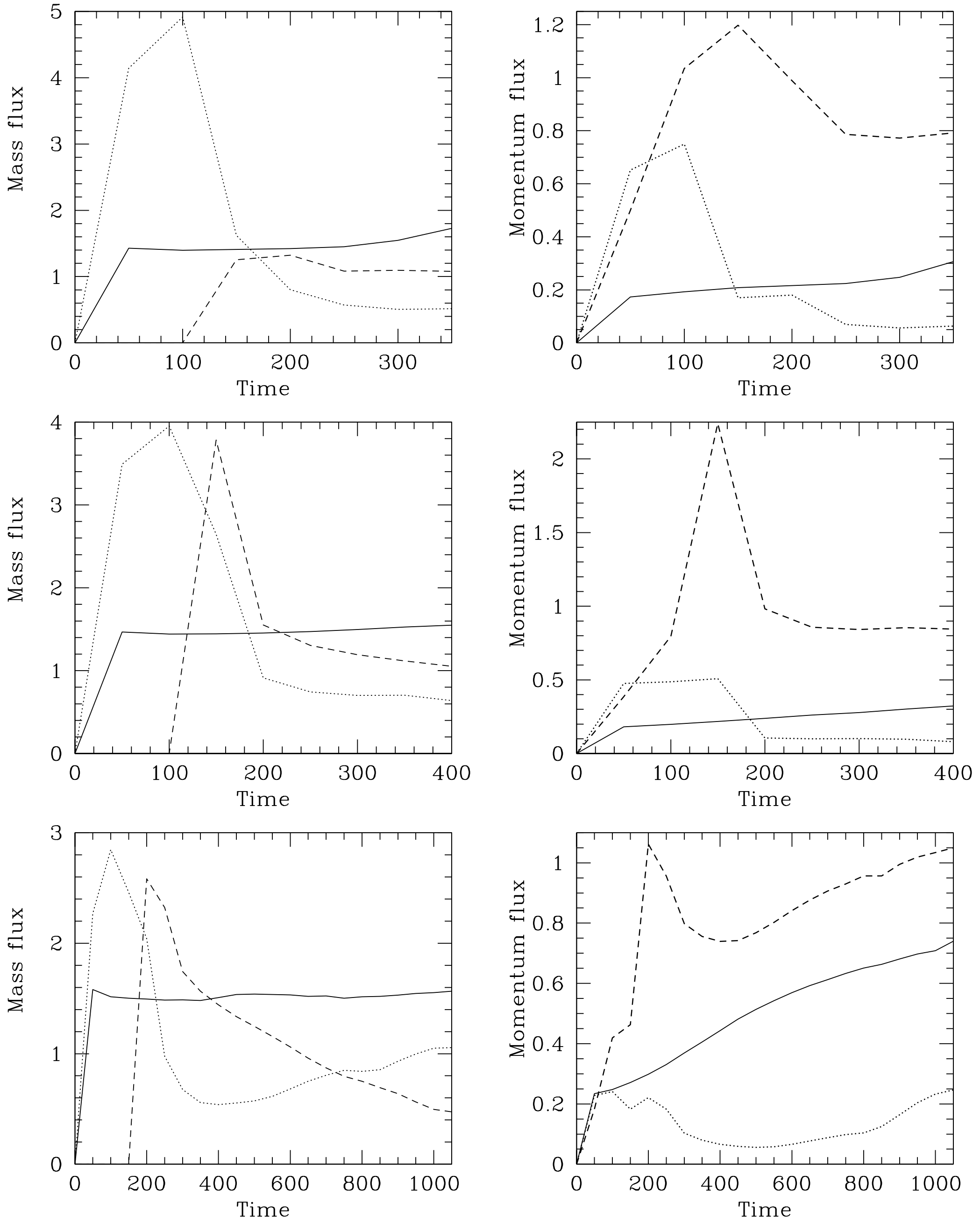

Figure 4.12: Time evolution of the mass flux and kinetic momentum flux for different magnetic diffusivity, $\eta = 0, 0.1, 0.5$ (*top*, *middle* and *bottom* figures, respectively), in the inner part of the jet, $(z \times R) = (60 \times 20)R_{\rm i}$. The final point of each line corresponds to the end of the simulation when the (quasi-) stationary state has been reached. Shown is the mass flux (*left* column) across the different boundaries. The mass inflow across the first active grid cells along the $(z = 0)$-boundary (*solid*), across the outer $(z = z_{\rm max})$ axial boundary (*dashed*), and across the outer $(R = R_{\rm max})$ radial boundary (*dotted*). Also shown is the kinetic momentum flux across the boundaries (*right* column). The *solid* line denotes the poloidal kinetic momentum flux across the first active grid cells along the $(z = 0)$-boundary. Note that this is already evolved from the value of the boundary condition. The *dashed* line denotes the momentum flux in $z$-direction integrated along the outflow boundaries. The *dotted* line denotes the momentum flux in $R$-direction integrated along the outflow boundaries.

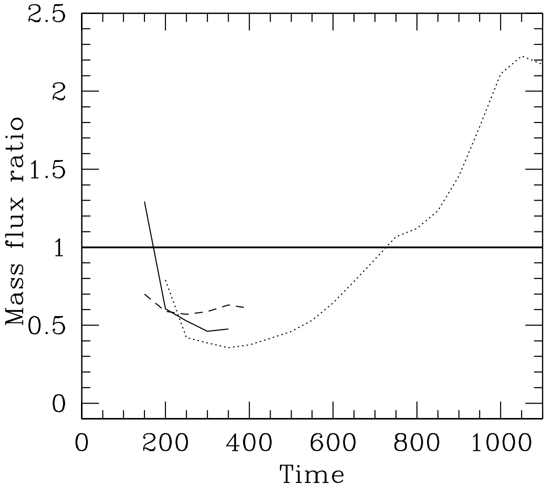

Figure 4.13: Time evolution of the mass flow ratio between the radial outflow boundary (the mass flow in $R$-direction) and the axial outflow boundary (the mass flow in $z$-direction) for different magnetic diffusivity, $\eta = 0, 0.1, 0.5$ (*solid*, *dashed* and *dotted* line, respectively), in the inner part of the jet, $(z \times R) = (60 \times 20)R_{\rm i}$. The final point of each line correspond to the end of the simulation when the (quasi-) stationary state has been reached. For a higher diffusivity, the mass flux ratio in the quasi-stationary state increases, indicating a decrease in the degree of collimation.

Such an acceleration purely by magnetic forces complies with an enhanced magneto-centrifugal effect picture. For the parallel component, with increasing magnetic diffusivity, the poloidal velocity increases – see Fig. 4.11. Because of higher velocity, the inertial forces are stronger and, for moderate heights above the disk, the (diffusive) fluid will tend to maintain the radial direction even if the field lines bend in the direction of the jet axis. The mass flow is re-distributed along the field line. As could be expected for the increasingly collimated flows, the parallel component and the toroidal Lorentz force components decrease rapidly with increasing $z$. The toroidal component accelerates the plasma in a toroidal direction, adding an additional centrifugal effect which drives the matter in a radial direction to diffuse across the magnetic field. This is why the mass flow rate increases along the outer streamlines with increasing $\eta$.

For the corresponding components of the acceleration, what one would expect from the standard MHD jet model is that, compared to the perpendicular component, the parallel and the $\phi$ components of the corresponding acceleration have a steeper maximum and decrease beyond the Alfvén point. This is confirmed in our simulations. The perpendicular components[7] are substantial throughout the whole inner jet. This indicates that also in the asymptotic regime of the collimated jet the flow is collimated

---

[7] The perpendicular components collimate the flow, so the sign for $F_{\rm L,\perp}$ is defined positive for the force vector pointing radially outwards, and the increase of $|F_{\rm L,\perp}|$ indicates an increase of the collimating Lorentz force.

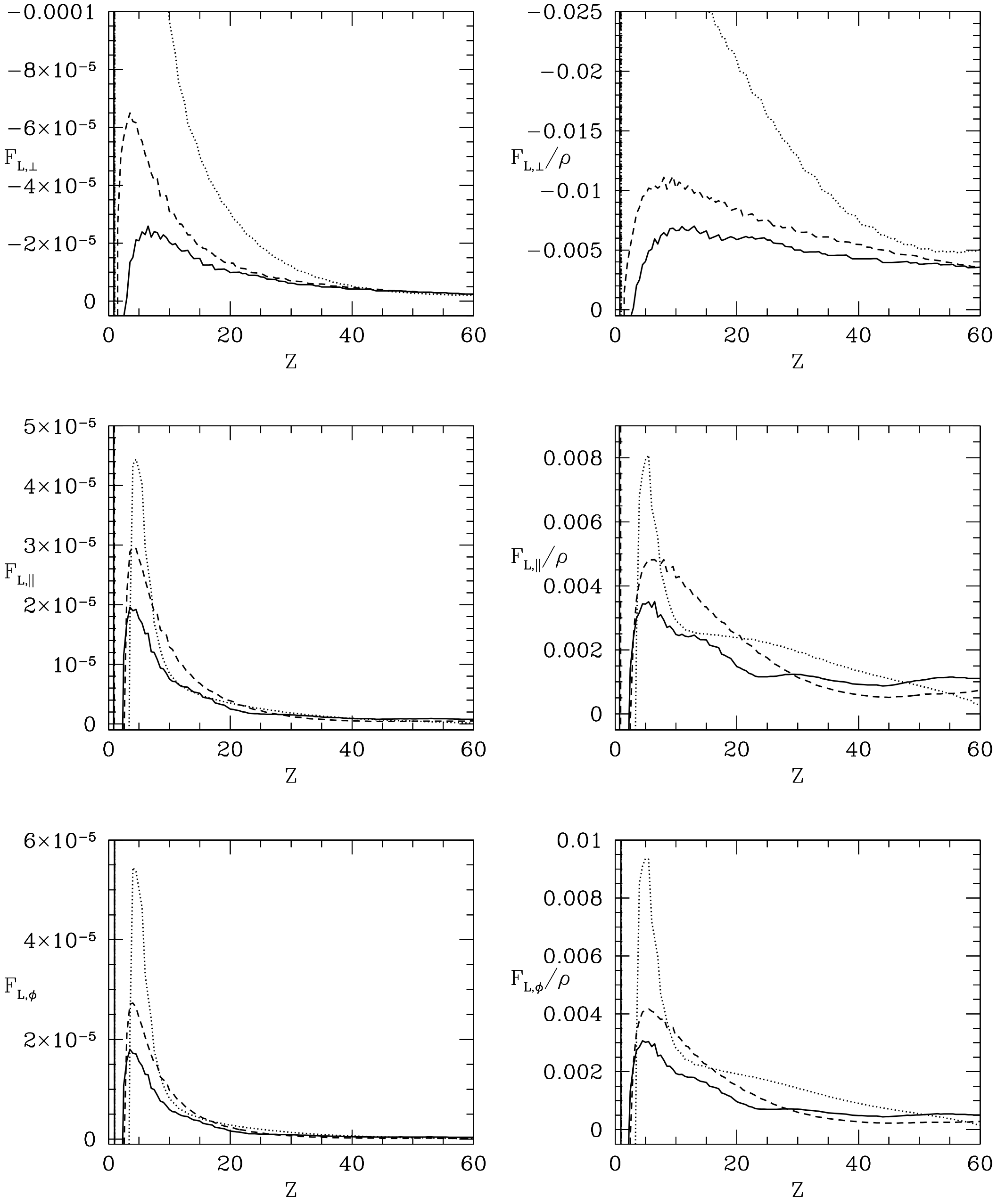

Figure 4.14: Lorentz forces in the jet for different magnetic diffusivity $\eta = 0, 0.1, 0.5$ (*solid, dashed, dotted* lines). *Left* column: (Normalized) values of the force component perpendicular (*top*) and parallel (*middle*) to the field line and the toroidal component (*bottom*), $F_{\mathrm{L},\perp}$, $F_{\mathrm{L},||}$, $F_{\mathrm{L},\phi}$, along a flux surface leaving the box of the inner jet close to $(R = 20, z = 60)$-corner (see Figs. 4.7 and Fig. 4.8). The sign is defined as follows. For $F_{\mathrm{L},\perp}$ the positive sign denotes the $r$-direction (de-collimating force). For $F_{\mathrm{L},||}$ the positive sign denotes the $z$-direction (accelerating force). For $F_{\mathrm{L},\phi}$ the positive sign denotes the $\phi$-direction. *Right* column: Corresponding values of the magnetic acceleration $(F_{\mathrm{L},\perp}/\rho)$, $(F_{\mathrm{L},||}/\rho)$, $(F_{\mathrm{L},\phi}/\rho)$.

by these forces.

As for $\eta$=0 and $\eta$=0.1 there is only a slight difference in the strength of the perpendicular components of force and acceleration at large distances, the degree of local flow collimation should be similar. This is visible in the poloidal *velocity* vectors in Fig. 4.9, which are well aligned. As for $\eta$=0.5 we are above the critical value $\eta_{\rm cr}$, the perpendicular components are more changed.

In conclusion, the perpendicular Lorentz force is shown to be essential for the collimation of the entire (inner) flow. Higher velocities in the jet flow are the result of the increasing parallel Lorentz force with increasing diffusivity, and the toroidal Lorentz force adds an (centrifugal) push to the matter in the still uncollimated parts of the flow.

## 4.5 Summary of the results

The time–dependent simulations of the formation of axisymmetric protostellar *resistive* MHD jets are performed, with investigation of the collimation and acceleration of the outflow. For this task, we implemented the physical magnetic diffusivity in the ZEUS-3D code. The accretion disk has been taken as a fixed boundary condition, and the initial setup is for a force-free magnetic field in a hydrostatic corona. An assumption of *constant* diffusivity is taken, although the diffusivity self-consistent to the turbulent Alfvénic pressure was analytically estimated and simulated, but was not found to affect the main results substantially.

The main results are:

(1) In the global scale of our simulation, the jet bow shock advances slower through the initial hydrostatic corona for the resistive jets. The reason is lower mass flux in the direction along the jet axis in these jets. As expected, the internal structure of the jet is less disturbed in the case of diffusion. The Alfvén surface comes closer to the disk surface.

(2) For our model setup we find that, similar to the case of ideal MHD jets (Ouyed & Pudritz 1997a; Krasnopolsky et al. 1999; Fendt & Elstner 2000), also resistive MHD jets can reach a quasi-stationary state. With increasing magnetic diffusivity, the quasi-stationary state of the jet is reached later.

(3) With increasing diffusivity the jet poloidal velocity increases. The direction of the velocity vectors does, however, only change weakly. At the same time the poloidal magnetic field distribution becomes increasingly de-collimated.

(4) As a proper measure of the degree of collimation we suggest the ratio of the mass flux along and perpendicular to the jet axis. If we compare the mass flow rates through the grid boundaries for different diffusivity, we find strong indication for the existence of a *critical value* for the magnetic diffusivity $\eta_{\rm cr}$ concerning the jet collimation. Beyond this value we still find an almost cylindrically collimated

stream along the jet axis, however, the bulk mass flow is in a radial direction. For our setup, the critical (normalized) diffusivity is about $\eta_{\rm cr} \approx 0.3$.

(5) We discuss a self-consistent picture where these effects of jet de-collimation and acceleration are explained in the context of Lorentz forces. The perpendicular Lorentz force is essential for the collimation throughout the entire flow along the jet axis. The parallel Lorentz force increases for increasing magnetic diffusivity and gives rise to the higher velocities in the jet flow. The toroidal Lorentz force accelerates the plasma in a toroidal direction. This leads to additional centrifugal forces re-distributing the mass flow rates across the magnetic flux surfaces towards the outer (yet un-collimated) parts of the flow. The latter two components play no role for larger distances along the flow.

Our conclusion is that the magnetic diffusivity could be substantial for the jet formation process. It is assumed that turbulence from the accretion disk will enter the disk wind and will be further advected into the jet.

# Chapter 5

# Numerical simulations of jet formation without toroidal magnetic field

A majority of the astrophysical jet models describe the collimation as due to the "hoop stress". This stress is the tension in the portion of the flow which stops corrotating with the disk. Loops of the toroidal component of the magnetic field are then added to the flow for each rotation of the foot point of the field line anchored in the disk. In such models the toroidal component of the field is essential for collimation and acceleration of the jet.

In an alternative model, the collimation of the astrophysical jet is, instead due to the "hoop stress", due to the magnetic pressure because of the poloidal field of the disk (Spruit et al. 1997, hereafter S97; see §3.6 here). The toroidal field developing in a magnetically accelerated jet is claimed to be unstable and, therefore, not to contribute much to collimation.

To verify this possibility, we performed a set of numerical simulations using the original (non-resistive) ZEUS-3D code in the 2D (axisymmetry) option, for cylindrical coordinates (R,$\phi$,z). The disk is taken as a boundary condition only, and the normalization is the same as in §4.1.1 here.

## 5.1 Instability of toroidal fields

The toroidal field, formed by the highly wound-up poloidal magnetic field beyond the Alfvén surface, is known to be unstable to non-axisymmetric instabilities (Bateman 1980). These instabilities were studied in the controlled fusion context, and the most damaging are the ideal MHD modes (kink instability), as the diffusion–related modes (e.g. tearing modes) are beyond the dynamical time scale. This scale is defined by the time in which an Alfvén wave crosses the jet radius.

In cylindrically symmetric configurations, the plasma without external stabilizing sur-

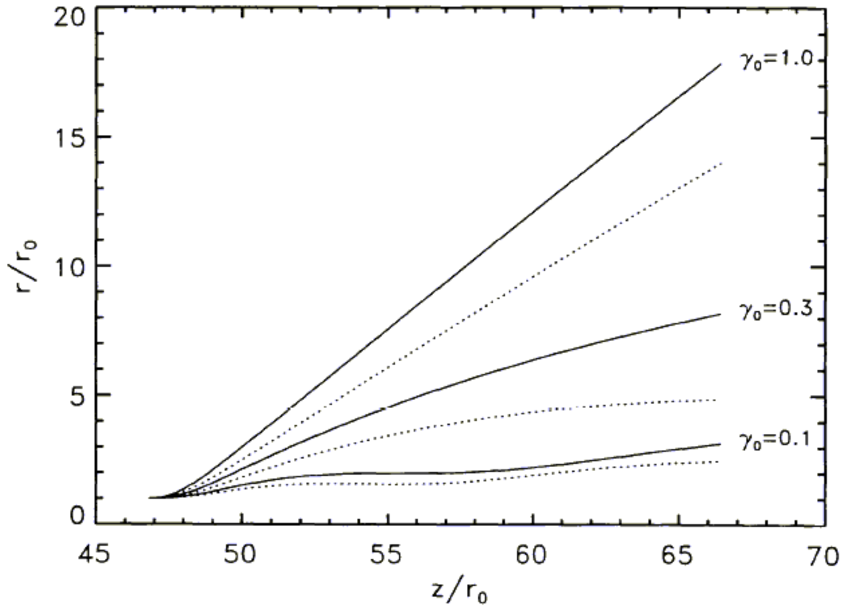

Figure 5.1: Decollimation of the jet due to instability of the toroidal field. Initially, the jet is assumed to be perfectly collimated ($\Theta_0$=0). The *solid* lines: including internal pressure generated by the instability (f=1); the *dotted* lines: without this pressure (f=0). Parameter $\gamma$ is the assumed growth rate of the instability in units of the nominal rate $u_{\mathrm{A}}/r$. Figure adopted from S97 (Fig. 2).

faces is unstable. *Kruskal–Shafranov* condition states that when the magnetic field lines in a fluid make more than one turn around the axis between two surfaces, the instability occurs if there are no such stabilizing surfaces. Typically, a $m$=1 kink mode sets in for any degree of twist. In a magnetically collimated jet a systematic twist is present, and there are not any stabilizing surfaces. This makes the astrophysical jet approximated with an ideal MHD cylindrical model subject to a kink instability.

The question is if such instability damages the jet collimation. The energy feeding the instability is the energy of the toroidal component of the magnetic field, which is proportional to $B_\phi^2$. For the jet radius $r$ and the density $\rho$, the instability growth rate is of the order $B_\phi/(r\sqrt{4\pi\rho})$ (Bateman 1980, §6.4). If a collimation is mainly by the hoop stress, the toroidal component $B_\phi$ must satisfy $B_\phi \geq B_z$. For a given $B_z$ and $\rho$, the instability grows with increasing collimation of the jet.

The effect of the instability on a collimation is investigated in S97 (§3), and is illustrated in their Fig. 2, repeated here in Fig. 5.1.

For the growth rate $\gamma$=1, which is the assumed growth rate of the instability in units of the nominal rate $u_{\mathrm{A}}/r$, an initially completely collimated jet terminates as a flow with an opening angle of order 45°. Even if the part of instability generated by the internal pressure is neglected (f=0 case in Fig. 5.1), the jet is completely decollimated. Only for $\gamma$<1, which is an arbitrary assumption, the final collimation angle becomes proportional to $\gamma$. This would imply that the highly collimated jets are impossible when the kink instability is present.

## 5.2 Collimation by poloidal magnetic field

The magnetic field configuration which enables a collimation of the astrophysical jets can still be questioned. An alternative to the hoop stress collimation could be found in the magnetic field carried by the accretion disk. This *poloidal collimation* is effective enough for realistic assumptions about the strength and distribution of the magnetic field in the disk (Blandford 1993; Spruit 1994).

The strength of the magnetic field in the disk, independent of the origin (a disk dynamo or an interstellar/intergalactic poloidal magnetic field captured by the disk) is likely to increase towards the disk center. E.g. for a vertical component of the magnetic field at the disk surface,

$$B_z \sim (\frac{R^2}{R_{\rm i}^2}+1)^{-\mu/2} \;, \tag{5.1}$$

the field strength increases towards the centre for $\mu>0$. $R_{\rm i}$ is the inner disk radius. If the Alfvén surface is positioned far enough from the disk surface, the field near the disk is approximately a potential one, completely defined by the disk surface field $B_z(R,z)$ as a boundary condition. Most of the magnetic flux crossing the disk ($\Phi \sim R^{2-\mu}$) is in the outer portions of the disk. Because of the geometrical reasons, with increasing $R$ outer field lines more influence the solution of the potential problem.

At height $z$ above the disk, the field strength is of the order $B(R=z,z=0)$, and approximately $R^2B_z=const$, i.e. $R\sim z^{\mu/2}$. For an infinite $z$, $dR/dz \to 0$, which implies a collimating shape of the field lines for $\mu<2$. The outflow changes the field of a disk, but significantly only after the Alfvén radius $R_{\rm A}$ is reached, i.e. the outflow is already highly collimated by the poloidal field of the disk.

For an *infinite* disk as above, position of the Alfvén surface determines the poloidal collimation of the outflow, and this collimation increases with increasing $R_{\rm A}$. For a *finite* disk, as all the magnetic field lines return back to the equatorial plane of the disk, the field is of dipole type, i.e. decollimating. There exists such $R_{\rm A}$ for which the maximum possible collimation is achieved.

An estimate of the collimation by the field of finite disk is sketched in S97 (§4.1). If we ignore the toroidal field, for the strong enough external field the internal pressure of the jet is in equilibrium with the external one, i.e. $B_{\rm int}=B_{\rm ext}$. For the narrow jet, as its effect on the surrounding field is small, $B_{\rm int}(z)=B_{\rm ext}(R=0,z)$. In this expression, $B_{\rm ext}(R=0,z)$ is known field distribution at the disk surface. The internal field scales with the jet radius as $r^{-2}$, and $(r/r_0)^2 = B_{\rm ext}(0,z_0)/B_{\rm ext}(0,z)$. The Alfvén surface, where the jet calculation is started in S97, is at $z_0$, and $r_0$ is the jet radius at that point. If we assume the flow speed along the jet constant, we have for the density in the jet $\rho/\rho_0 = (r_0/R)^2$, and the Alfvén speed in the jet is

$$\frac{u_{\rm A}}{u_{\rm A0}} = \frac{B_{\rm ext}(z)r}{B_0 r_0} = \sqrt{\frac{B_{\rm ext}(z)}{B_0}} \;.$$

There exists a point $z_{\rm c}$, a *collimation distance*, where the radial expansion speed $u_\perp =$

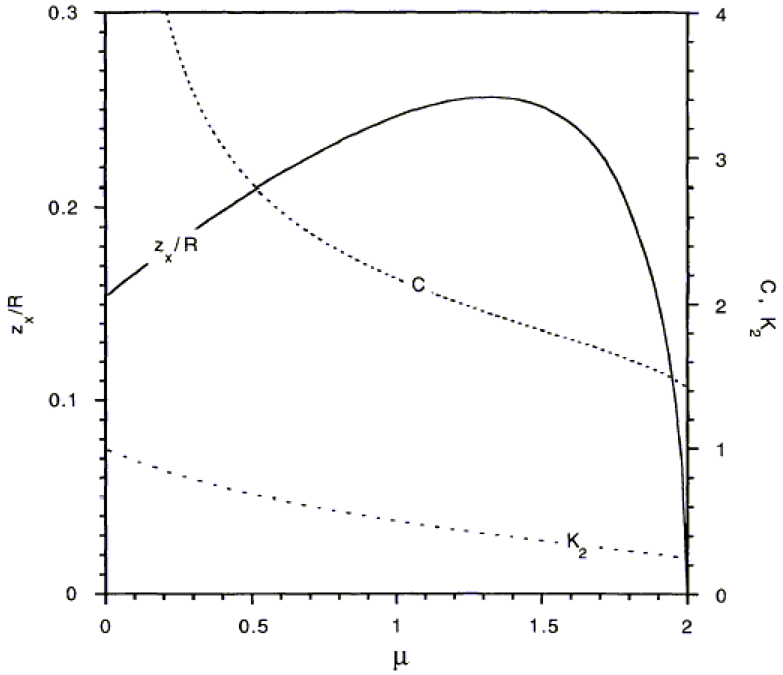

Figure 5.2: The solid line shows the height above the disk, $z_x$, of the inflection point in the field line shape. Figure adopted from S97 (Fig. 5).

$dR/dt$ becomes comparable to the Alfvén speed $u_{\rm A}$, beyond which the equilibrium of pressures is not satisfied any more. Such an equilibrium could be maintained only up to the Alfvén speed. After reaching $z_{\rm c}$, the jet expands balistically at constant opening angle $\Theta_\infty = u_\perp/u_{||}$, which is the asymptotic collimation angle. If we assume that the matter follows the poloidal field lines up to the height $z_{\rm c}$ and then decouples from the field, the collimation angle $\Theta$ is equal to the angle of the poloidal field line with respect to the axis at $z_{\rm c}$.

For a distribution of current $j(R) = J_0(r_{\rm d}/R)^\mu$, in a finite disk of radius $r_{\rm d}$ (where $0<R<r_{\rm d}$, and $j(R) = 0$ for $R>r_{\rm d}$), for a field lines close to the axis:

$$\boldsymbol{B}\cdot\nabla\tan\Theta \sim -\frac{RB_z}{z^2}\frac{\mu(2-\mu)}{4} < 0 \;\; (0<\mu<2)\,.$$

For the height $z_x$ the collimation angle is minimal for the field close to the axis. The corresponding integral equation is solved numerically in S97, and the result is shown in solid line in Fig. 5.2.

We see that the inflection point in the solution is located at $z_x \sim 0.2 r_{\rm d}$ for most values of $\mu$, and there is a steep decrease when $\mu$ reaches the value 2.

The thorough derivation of this result is given in S97. Here we are interested in the result from Fig. 5.2, as $\mu$ is the free parameter in the numerical simulation in which we check the poloidal collimation conjecture. S97 find that for $B \sim r_{\rm d}^{-\mu}$ with $\mu \lesssim 1.3$, the jet becomes collimated. Note that at intermediate distances, e.g. $r_{\rm d}/r_{\rm i} = 10^4$, the asymptotic angle $\Theta_\infty$ is only an analytical approximation of the numerical solution for the inflection point obtained in S97 (see Fig. 6 there). However, it is assumed close enough, and in our numerical simulation we set $B \sim R^{-\mu}$.

## 5.3 Initial and boundary conditions

In our numerical simulation, performed with the ZEUS-3D code in the axisymmetry option, the underlying accretion disk is prescribed as Keplerian, fixed and time-independent. The initial state is defined using the JETSET tool (Jørgensen et al. 2001).

This is the tool for setting initial states of astrophysical jet simulations. The initial set-up consists of a disk corona in hydrostatic balance with the gravitational field of central object, with a current-free magnetic field threading through the corona. An initial state generated by JETSET, if left unperturbed, remains in perferct numerical balance to within machine round-off errors.

What is actually obtained from the JETSET package is a current-free magnetic field without the toroidal component, computed as a solution of the Laplace equation,

$$\nabla^2 \varphi(R, \phi, z) = 0. \tag{5.2}$$

The solution is proportional to the hypergeometric function,

$${}_2F_1\left(\frac{\mu}{2}, \frac{\mu-1}{2}, 1, -\frac{R^2}{z^2}\right),\ 3 > \mu > 1/2\,, \tag{5.3}$$

and corresponds to the boundary condition

$$B_{R,0} = bR^{-\mu}. \tag{5.4}$$

Here, $b$ is a normalization factor, and $B_{R,z=0}$ is a radial component of the magnetic field in the disk.

In a present JETSET package, only the solutions for 3>$\mu$>1 and $\mu$=0 are allowed. We varied the parameter $\mu$ and obtained initial configurations of the poloidal magnetic field shown in Fig. 5.3. The outgoing angle of the magnetic field lines threading the underlying disk is also the angle of the initial inflow velocity $u_{inj}$, and this velocity is a free parameter in our simulations. With this initial solutions by the JETSET tool as the initial conditions in the ZEUS-3D computations, we performed the time-dependent simulations for the outflow of injected material in the magnetic field of a disk corona.

As a free parameter for the initial inflow velocity we choose $u_{\mathrm{inj}} = 0.001\ u_{\mathrm{K,i}}$. The inflow density is $\rho_{\mathrm{disk}} = \eta_{\mathrm{i}} R^{-3/2}$, with the free parameter $\eta_{\mathrm{i}}$=100, and $\delta_{\mathrm{i}}$=2.5, as described in OP97 for a hot corona case (when access to an additional source of energy is required). The toroidal magnetic field component is set to zero in every computational step in the whole computational box, and the inner edge of the disk together with the innermost part (for $R \leq R_{\mathrm{i}}$) is defined with the inflow velocity equal to zero.

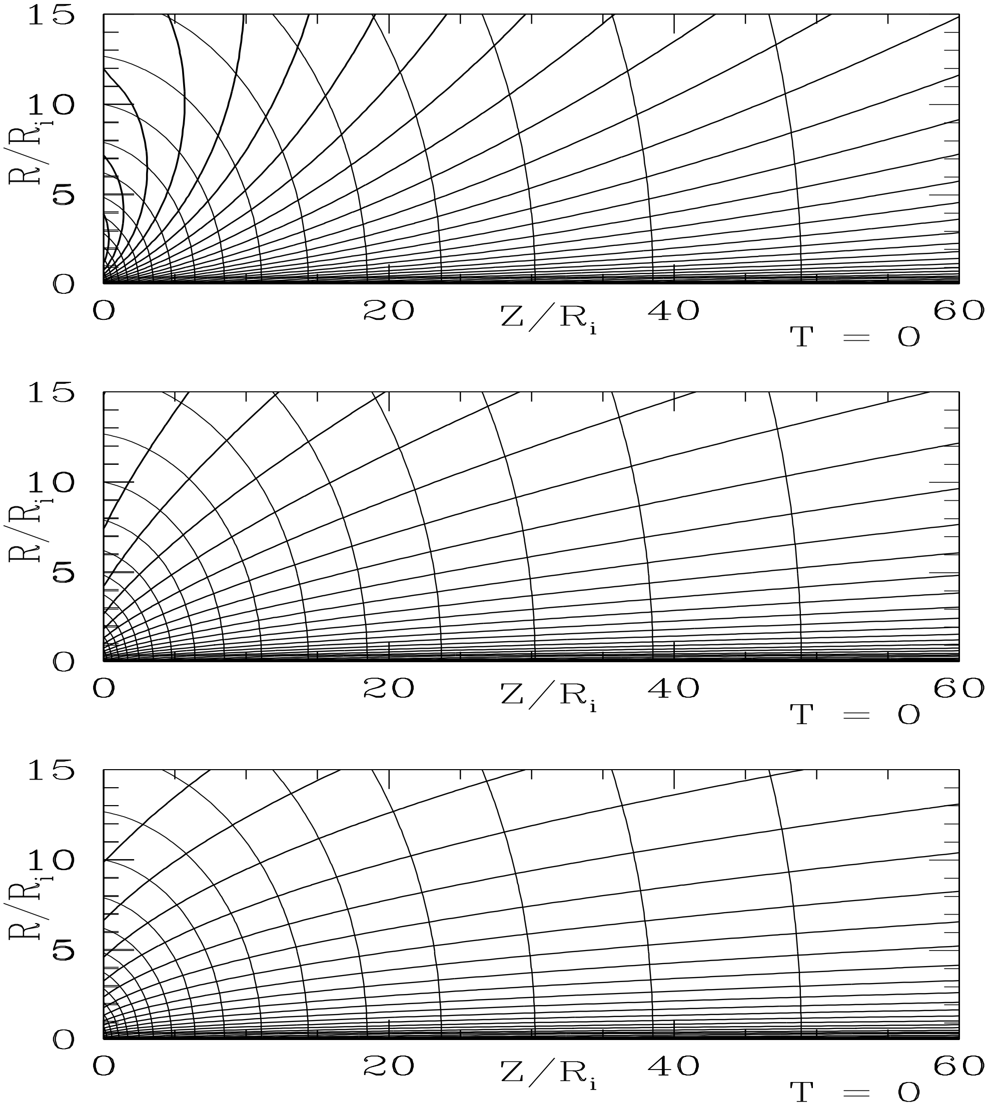

Figure 5.3: Initial setup for the simulations with various parameters $\mu$. *Thin* solid concentric lines indicate 30 logarithmically spaced isocontour lines of the initial hydrostatic density distribution. *Thick* solid lines are the field lines of initial force–free magnetic field. The parameter $\mu$ equals 2.999,1.5,1.01, i.e. an almost dipole field lines and open (split–monopole) magnetic field, respectively.

The computational box boundaries are set as "reflecting" along the symmetry axis and "outflow" along two outer boundaries (see §4.1.2 for a definition of the boundaries).

Uniform numerical mesh in the simulations contained (125×50) grid points, in a domain $(z\times R)$=$(60\times15)R_\mathrm{i}$.

### Cold disk corona

We first performed the simulations with the above described setup for a *cold* disk corona case, which is obtained for $\delta_\mathrm{i}$=100, when there is no any additional source of energy in a corona assumed. These simulations are then in the spirit of Chapter 4 here, but with the initial magnetic field numerically determined by JETSET tool, instead of analytical prescription. The toroidal component of the magnetic field was artificially destroyed in every step of the computation. The result *always* showed to be a non-collimated outflow, independent on the free parameter $\mu$, for our setup. This would support the conclusion that the collimated and accelerated outflow (i.e. the jet) from a cold corona of the accretion disk is not possible in the absence of a stable toroidal magnetic field.

## 5.4 Variation of the parameter $\mu$

For the simulations with $\delta_\mathrm{i}$=2.5, we will present the results for two open (split-monopole) magnetic field simulations from Fig. 5.3, for $\mu = 1.01$ and $\mu = 1.5$.

Changing the plasma-$\beta$ parameter provides a way to position the Alfvén surface high enough above the accretion disk surface. In S97 (§4.1) it is claimed that “Poloidal collimation by discs of finite size therefore works best if the Alfvén surface is neither too close to the disc surface, nor too far away”.

If the plasma is super-Alfvénic from the very beginning of the simulation, what occurs for some $\beta$-plasma values in our setup, we obtain a physically different case than one discussed here (see Contopoulos 1995b). For this reason we do not present the results for $\mu$=2.999, which were super-Alfvénic from the very disk surface in our setup.

The outgoing angle of the magnetic field lines defines also the inclination angle of the inflow velocity. This angle, measured from the jet axis, for the split-monopole magnetic field lines is presented in Fig. 5.4. It complies with the BP82 criterion (see §3.1.1 here) for both investigated choices of the parameter $\mu$.

Simulations are presented for a time for which they can be considered *quasi-stationary* close to the disk surface. A quasi-stationarity of the flow is assumed when inner regions of the flow, close to the central object, do not evolve significantly in time within the ±50 rotation times (see §4.3.2 here). For the different position of the Alfvén surface in the simulations with $\mu$ =1.01 (e.g. for $\beta_\mathrm{i}$ ~10, when this surface is closer to the disk surface) we obtained a radially directed outflow, similar to one in the top panel in Fig. 5.5.

The terminal poloidal velocity of the collimated outflow ($\mu = 1.01$ case) is of the order of $4u_\mathrm{K,i}$, i.e. of the order of the escape velocity of the central object. The velocity and the magnetic field strength in the slice parallel to the axis of symmetry, at half of the computational box height, are given in Figs. 5.7 and 5.8.

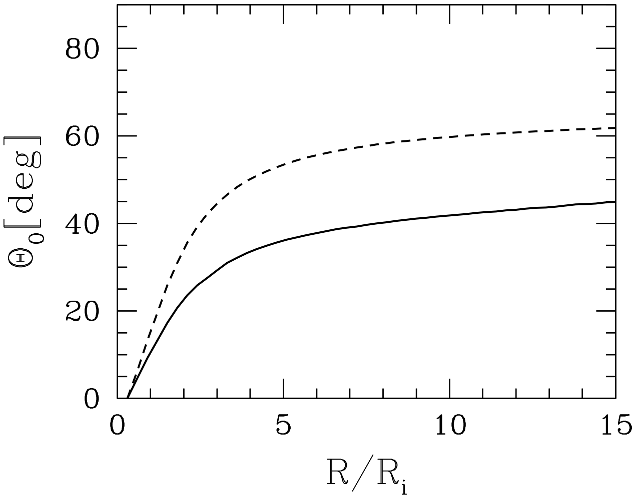

Figure 5.4: The inclination angle (measured from the jet axis) of the inflow velocity for the simulations with the different parameter $\mu$, for the open (split-monopole) magnetic field. The *solid* line represents the case when $\mu = 1.01$, and the *dashed* line is for $\mu = 1.5$.

These simulations support the claim by S97 that, for a hot corona, a poloidal magnetic field is sufficient for accelerating and collimating the outflows, if the initial field of the disk is $B \approx R^{-\mu}$, with $\mu \lesssim 1.3$ (in our simulations $\mu < 1.5$). The essential parameter was the strength of the initial poloidal magnetic field. For a too large magnetic field there was no collimation, although the outflow (then mostly radial) remained fast. Without the toroidal component of the magnetic field, there is no fast magnetosonic surface in these simulations. The acceleration of the flow stops, therefore, at the Alfvén surface.

The flow is magnetically accelerated and collimated up to the *collimation distance*, where the radial expansion speed of the jet reaches the Alfvén speed, $u_\mathrm{A}$. Beyond this distance, the flow expands ballistically, as the surrounding poloidal field can not influence it any more. Such a jet is *non-magnetic*, with a ballistic (magnetically unconfined) radial expansion and kinetic energy flux.

## 5.5 Summary of the results

We performed numerical simulations of the ideal–MHD outflow from the accretion disk for the case when the toroidal component of the magnetic field is artificially reduced to zero. The effect of a sole poloidal component of the magnetic field on the collimation of the outflow is investigated. Also, we implemented flexible initial setup tool JETSET together with the ZEUS-3D package to obtain the initial configurations which span from the straight lines of the magnetic field, perpendicular to the disk surface, and open (split–monopole) to the dipole–like magnetic field lines.

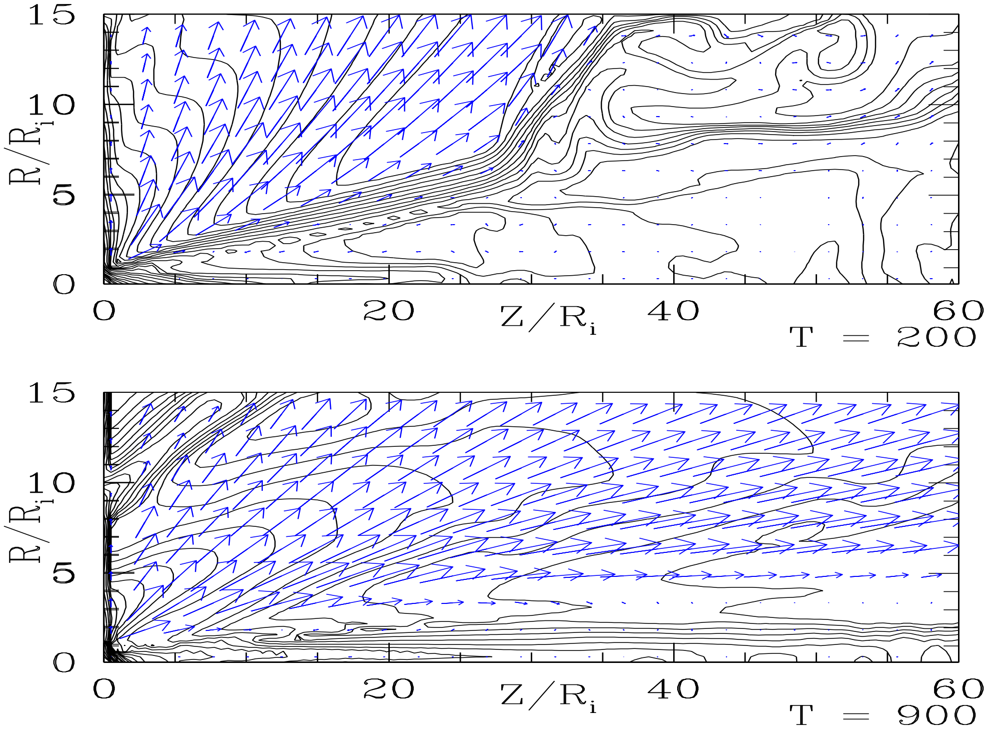

Figure 5.5: The flow evolution for the open field initial configurations from Fig. 5.3. The free parameter $\beta_i$=1. The *solid* lines represent 30 logarithmically spaced density isocontours. Vectors of poloidal velocity are shown in scale in both plots. *Top* panel is for $\mu$=1.5 case, at $t = 200$ rotations of the inner disk radius. *Bottom* panel shows $\mu$=1.01 case, at $t$=900 rotations of the inner disk radius. The disk disruption in the radial inflow boundary results from the inappropriate boundary condition. However, because of the density distribution, the mass flux of the outflow results from the inner half of the disk, when the small outflow from this top upper corner of the plot exits the top boundary immediately in the radial direction.

Results can be summarized as follows:

(1) In all investigated situations, we found no sign of the accelerated and collimated flow for the cold corona simulations in the absence of the toroidal magnetic field. The flow opening angle changes for different positions of the Alfvén surface, but resulting outflows are not accelerated.

(2) The hot corona simulations without the toroidal magnetic field present *can* result in a collimated, accelerated outflow. For the initial magnetic field of the disk $B \approx R^{-\mu}$, with $\mu < 1.5$ an outflow is collimated and accelerated.

Our conclusion is that in the ideal–MHD simulations the toroidal magnetic field plays an essential role for the acceleration and collimation of the magnetic outflows in a cold

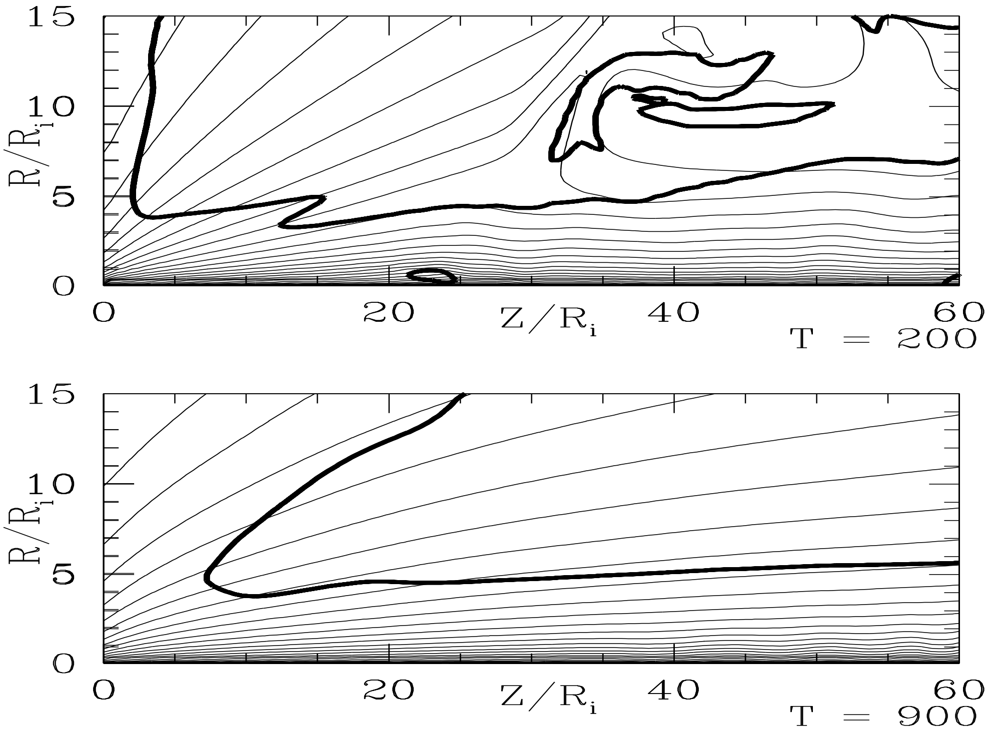

Figure 5.6: The poloidal magnetic field lines and the Alfvén surface for the simulations presented in Fig. 5.5. *Thin* solid lines denote twenty linearly spaced poloidal magnetic field lines, and *thick* solid line is the Alfvén surface.

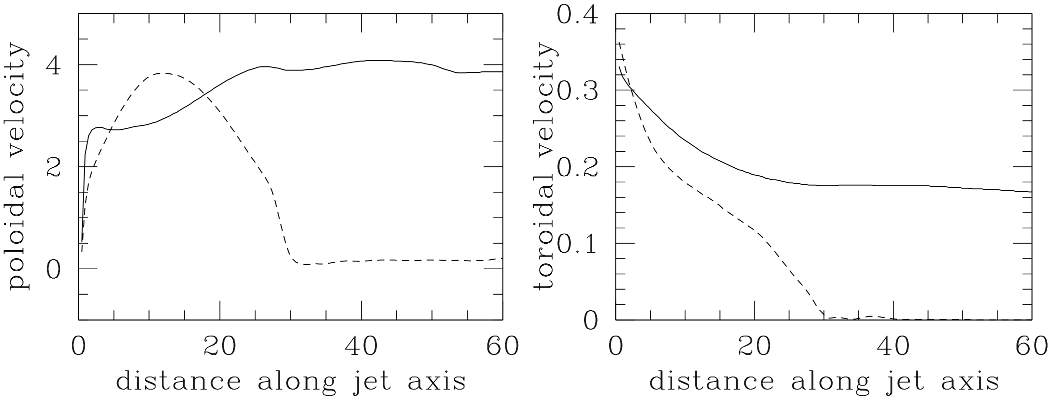

Figure 5.7: The poloidal and toroidal velocity for the investigated flows. Values are taken in a slice parallel to the axis of symmetry of the flow, at half of the computational box. The *solid* and *dashed* line represent the results for $\mu = 1.01$ and $\mu = 1.5$, respectively.

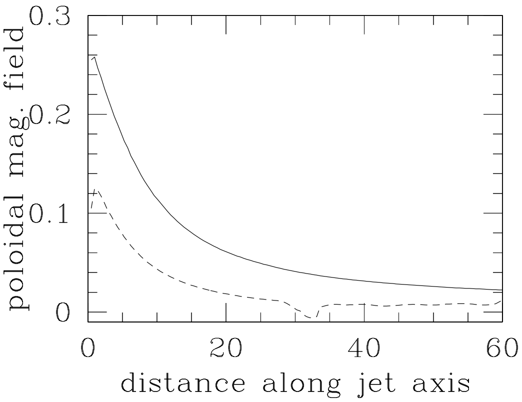

Figure 5.8: The poloidal magnetic field. The *solid* and *dashed* line represent the results for $\mu = 1.01$ and $\mu = 1.5$, respectively.

corona. The poloidal magnetic field alone is insufficient, even in the most suitable configurations, to produce and maintain the jet–like flows for such corona.

For a hot corona and $\mu < 1.5$, there exists the $\beta$-plasma parameter for which we obtain the collimated and accelerated outflow in our setup. The terminal velocity is of the order of magnitude of the escape velocity of the central object.

An important limitation in our computations is that the toroidal magnetic field was *artificially* destroyed during the computation. In the realistic model of the poloidal collimation this field, suitably damped by some physical mechanism, could play a role in the very beginning of the simulation, initially accelerating the flow.

# Chapter 6

# Numerical simulations of the disk-jet transition

A resistive accretion disk threaded by a large scale magnetic field provides a platform for a continuous MHD jet launching, when some amount of the turbulent magnetic diffusivity of the disk remains present in a disk corona. In Chapter 4 we presented our numerical simulations of the jet formation, propagation and collimation with a disk as a boundary condition. The interaction of the magnetic field in the jet with the disk magnetic field was neglected there. The next step in a numerical jet simulation is inclusion of a disk evolution in a simulation. This should provide an answer to the question if, and under which conditions, it is possible to launch a jet from a turbulent, resistive accretion disk in the presence of a large scale magnetic field.

The first numerical simulations of a rotating accretion disk in a large-scale magnetic field were performed by Uchida & Shibata (1985) and Shibata & Uchida (1985, 1986). The matter has been accelerated along the magnetic field lines mainly by the magnetic pressure gradient, and not magneto-centrifugally as in BP82 mechanism. In all successive simulations (Kudoh & Shibata (1997); Kudoh et al. (1998); see also §3.5.1 here for more references) the inner disk collapses after a few rotations. The stability of the accretion disk to MHD perturbations is mainly determined by the radial structure of the disk.

Before the numerical simulations of such systems became feasible, Ferreira (1997) and also Casse & Ferreira (2000a,b) suggested the self-similar stationary model with a resistive accretion disk and a super-Alfvénic jet. Because of the nonzero magnetic diffusivity, the accreted matter inside the disk can cross the poloidal magnetic surfaces, and be lifted into the disk corona.

Above the disk, the magnetic diffusivity is much lower than in the disk, and the outflow is effectively in the ideal MHD regime. The matter in such jet becomes "frozen" in a magnetic field, and is collimated and accelerated by the action of the Lorentz force.

The time-dependent simulations in such an approach require the disk to be evolved in time together with the corona of the disk. Therefore, we extend our numerical simulations of the jet from the Chapter 4 by including the disk evolution.

The first simulations of a resistive accretion disk launching nontransient, ideal MHD jet have been carried out by Casse & Keppens (2002, hereafter CK02) using VAC code (*Versatile Advection Code,* Tóth 1996). These are an extension of Ouyed & Pudritz (1997b) numerical simulations using the Zeus-3D code, which were also performed with a radially stratified initial corona, but including the disk as a boundary condition only. The jet obtained in CK02 simulations is persistent, with a caveat that the jet radial size is slightly dependent on a radial extension of the computational box. Simulations in a more general setup, with the initial magnetic field set as an open poloidal magnetic structure, have been carried out by Casse & Keppens (2003).

## 6.1 Model setup

In our simulations of a jet launched from a resistive accretion disk, diverse initial conditions were investigated. For reasons of comparison, we present here the calculation with a setup similar to CK02.

Schematic view of our model is presented in Fig. 4.1, and now we introduce the turbulent accretion disk into a computational box not as a boundary condition (as it was the case in Chapter 4), but in the active grid. We work in cylindrical coordinates and the axisymmetry is assumed.

A corona of the turbulent accretion disk is assumed also to be turbulent, although probably much less than the disk itself. In our simulations of the diffusive jet in a disk corona in Chapter 4, the total pressure was composed of the *thermal* and *turbulent* terms. Both components were modelled by the same polytrope ($\gamma$=5/3) and are, therefore, physically equivalent (Ouyed et al. 2003). The free parameter $\delta_{\rm i}$ defined in §4.1.2, referred to the inverse of the portion of total pressure considered to be thermal, and is chosen now to be unity instead of $\delta_{\rm i} = 100$ used there.

The Keplerian speed at the inner disk radius $R_{\rm i}$ is $u_{\rm K,i}$=$\sqrt{GM/R_{\rm i}}$. For reasons of comparison with CK02, we normalize all the velocities in our setup to the factor $\Omega_{\rm K,i}H$[1]. $\Omega_{\rm K,i}$ is the Keplerian angular velocity at $R_{\rm i}$, and $H$ is the disk height. As we choose $R_{\rm i}$ to be unity, defining the distance scale, it follows that $GM$=100. A constant of proportionality of the disk height to the radial distance in $H = \epsilon R$ is chosen to be $\epsilon$=0.1. To absorb the factor $1/\epsilon^2$, the central mass is set to $M$=100 in our computations.

The time is measured in the units of $t_{\rm i} = R_{\rm i}/u_{\rm K,i}$. It is the time needed for one rotation of the disk at $R_{\rm i}$. Compared to this, the time in CK02 is measured in the units of $\epsilon\Omega_{\rm K}$, which represent $1/(2\pi\epsilon)$=1.59 rotation periods of matter at $R_{\rm i}$[2].

---

[1] Note that afterwards in this chapter, in the presentation of results, we switch back to the definition of units from the Chapter 4, where $u_{\rm K,i}$=1 is the velocity unit.

[2] This means that t=10 in these simulations is a period of 16 rotations at the inner disk radius.

### 6.1.1 Boundary and initial conditions

The disk is now defined not as an inflow condition, as is the case in Chapters 4 and 5 here, when the disk surface is in the ghost zone of the computational grid. Instead, the disk is in the active part of the computational grid. The disk equator is defined with a reflecting boundary condition (see §2.3 for the definition of the boundaries).

For the density $\rho$ we apply a symmetric boundary condition at both the equatorial plane of the disk and the symmetry axis, as well as for the $z$ component of the magnetic field $B_z$. The radial and toroidal components of the magnetic field are taken as asymmetric at both these planes. The velocity components $u_R$, $u_z$ and $u_\phi$ are taken at the equatorial plane with symmetric, asymmetric and symmetric boundary condition, respectively, and along the symmetry axis with asymmetric, symmetric and asymmetric boundary condition, respectively (see Table 1 in CK02).

Real accretion disk is certainly larger than the part enclosed in our computational box. It is necessary to prescribe the effect of this outer part of the disk on the modelled structure. Therefore, a small amount of mass is injected along the outer disk boundary in the *negative* $R$ direction (i.e. the *inflow* boundary condition is prescribed there). All the other boundaries are defined as open.

We introduce a “sink” region near the central mass. It is a small - ($z \times R$)=(4×2) grid cells in our simulations - rectangular area where the values of all quantities are copied from the cell row $z'$ just above it (in the $z$ direction). Only for the poloidal velocity there is an additional condition in the “sink”, which ensures that no mass flux leaves it[3]:

$$u_R = \min(u_R(z'),0)\ ,\ u_z = \min(u_Z(z'),0)\ .$$

The computational domain and the boundary conditions are presented in Fig. 6.1.

We performed our simulations in an uniform grid with (125×80) grid cells in a physical domain ($z \times R$)=(60×40)$R_\mathrm{i}$. For a comparison, in the CK02 simulations the active grid is (300×150) elements in a physical domain ($z \times R$)=(80×40)$R_\mathrm{i}$. In their computations, in both radial and vertical direction stretching is applied, resulting in a higher resolution close to the disk. In another simulations, Kuwabara et al. (2000) set (256×201) grid cells in a physical domain ($z \times R$)=(13.4×5.1)$R_\mathrm{i}$, with stretching applied for $z$ and $R$ greater than $R_\mathrm{i}$=1. Compared to these, the resolution in our simulations is rather low, and this is why we characterize them as a *preliminary* results. However, a comparison with few higher resolution runs in the same setup showed no substantial changes in the jet structure. Only the disk evolution was somewhat slower in a physical time.

---

[3] The matter in the $R < R_\mathrm{i}$ and $z > 0$ zone can therefore originate only from the disk, not from the “sink”.

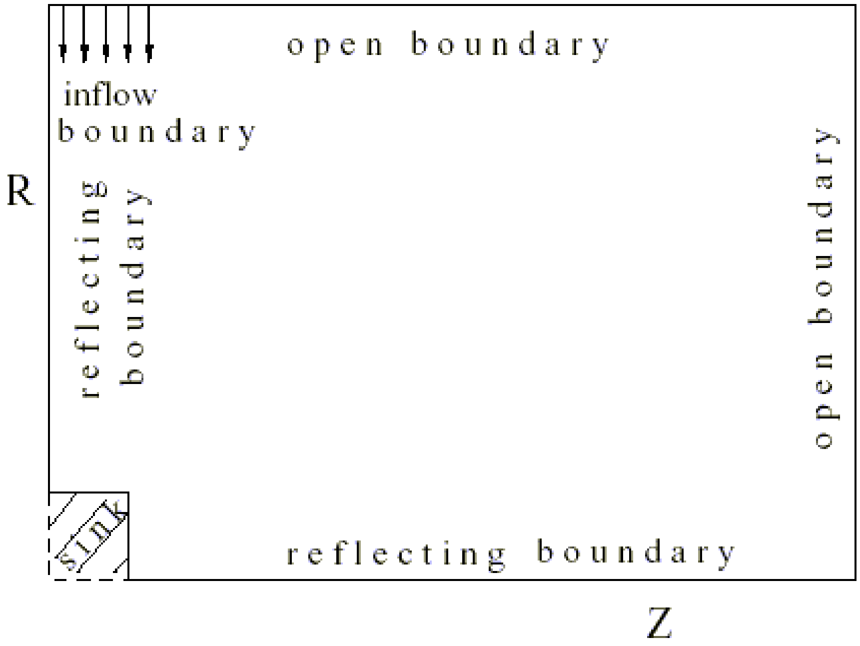

Figure 6.1: Schematic representation of the computational domain and boundary conditions for the simulations with the disk included in the computational box. The box dimensions are ($z \times R$)=(60×40)$R_{\rm i}$ in an uniform mesh of (125×80) grid cells. The "sink" region is ($z \times R$)=(4×2) grid cells.

### 6.1.2 Density profile

The simplest approach for the definition of a disk would be to define the disk height from the equatorial plane as $H$=$const$. However, then it is problematic to obtain the equilibrium between the gravitational and thermal pressure, as the gravity decreases with a radial distance. One density prescription investigated analytically and in numerical simulations is Gaussian:

$$\rho = \rho_0 \exp(-\frac{z^2}{H^2}) \, ,$$

where $\rho_0$ is the density in the equatorial plane of the disk, and $H$ is the height where the disk density reaches $1/e$ of the central density.

In a geometrically thick disk, for $H(R) \propto R$, the growth of the magnetic pressure is caused by an increasing toroidal component of the magnetic field (Ferreira & Pelletier 1993, §2.2). For increasing thickness of the disk, the thermal pressure can equal the magnetic pressure (i.e. the disk becomes optically *thin*). This is a rather unstable configuration, and to avoid it, and to allow for the jet to extract all the angular momentum from the disk, the poloidal magnetic field must change vertically substantially. However, if the magnetic field inside the disk would be vertical, an ejection of matter would not occur even if the magnetic braking would be sufficient. Therefore, the poloidal field lines should not be vertical, but *slightly* bent.

One way to set a *thin* disk in a computational box, is with the density given by a decreasing function of altitude $z$ above the disk equator. The density typical value must decrease over one disk scale height. For a disk height linearly proportional with the radial distance, $H=\epsilon R$, a natural scaling, consistent with the poloidal magnetic field lines bending at the surface of a disk is obtained.

For a thin accretion disk, the disk aspect ratio is $\epsilon$=0.1. The jet can extract all the angular momentum from the disk, if the magnetic Reynolds number $R_{\mathrm{m}}$ (see §2.1.2) is of order unity. Then the magnetic diffusivity is large enough for the matter to cross the magnetic field lines.

The vertical disk equilibrium and Keplerian rotation imposes the constraint for a radial density profile, as for the vertical balance in the disk the sound speed within the disk should be proportional to $\Omega_{\mathrm{K,i}}H$. At $t$=0, the density profile is defined with

$$\rho(R,z) = \max\left(10^{-6}, \frac{R_0^{3/2}}{(R_0^2+R^2)^{3/4}} \times \left(\max\{10^{-3}\ ,\ \left[1-\frac{(\gamma-1)z^2}{2H^2}\right]\}\right)^{1/(\gamma-1)}\right)$$

A constant offset radius $R_0$=4 is introduced to ensure the regularity of the density up to $R$=0, and the maximum function prevents the initial density in reaching non-physical values[4]. Our particular choice of the constants is, for reasons of comparison, due to CK02, but in our simulations the initial density range is smaller.

### 6.1.3 Velocity profile

In a thin accretion disk where the radiative pressure is neglected and $c_{\mathrm{s}}/u_{\mathrm{K}}\propto\epsilon$ (Shakura & Sunyaev 1973; Frank et al. 1985), $c_{\mathrm{s}} \ll u_{\mathrm{K}}$ is always satisfied.

In a radial direction, thermal and magnetic pressure gradients are of the same order, and to ensure a radial equilibrium of the disk, there should be some deviation from a Keplerian rotation profile. We define a sub-Keplerian rotation profile (see also CK02):

$$u_\phi(R,z) = (1-\epsilon^2)\frac{R_0^{1/2}}{\epsilon(R_0^2+R^2)^{1/4}}\exp\left(-2\frac{z^2}{H^2}\right)\ . \tag{6.1}$$

The initial poloidal velocity profile is to be defined only by the accretion rate in the disk, i.e. with a radially inward velocity. The angular and sound speed are both proportional to $1/\sqrt{R}$, and for the disk in an equilibrium the same is valid for the components of the poloidal velocity:

$$u_R(R,z) = -m_{\mathrm{s}}\frac{R_0^{1/2}}{(R_0^2+R^2)^{1/4}}\exp\left(-2\frac{z^2}{H^2}\right)\ , \tag{6.2}$$

$$u_z(R,z) = u_R(R,z)\frac{z}{R}\ . \tag{6.3}$$

---

[4] This density profile defines the corona which is *not* initially in hydrostatic equilibrium, but as the initial corona is swept out by the propagating bow shock, it should not influence the results in the later stages of the jet propagation.

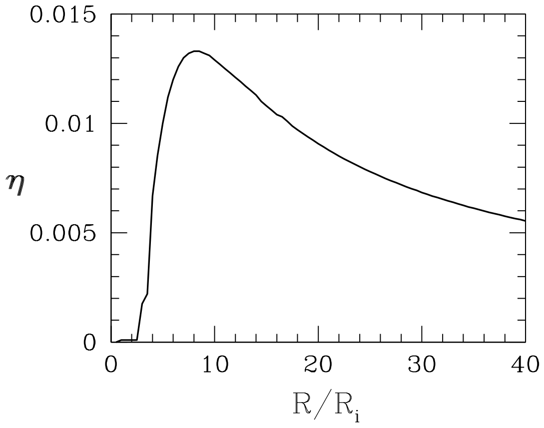

Figure 6.2: The magnetic diffusivity along the disk equatorial plane.

The constant parameter $m_{\rm s} < 1$ ensures an initially subsonic poloidal inflow and it is chosen in our simulations to be $m_{\rm s}$=0.3.

### 6.1.4 Magnetic field

In the axisymmetry approximation, the symmetry conditions for the equatorial plane of the disk and the axis of symmetry impose that $B_R(R$=0,$z)$=$B_R(R$,$z$=0)=0. Only then $\nabla \cdot \boldsymbol{B}$=0 is satisfied for the initial instant of time. Another condition is that the magnetic pressure be of the same order as the thermal pressure in the equatorial plane (Ferreira & Pelletier 1995).

The simplest configuration which satisfies both these conditions is a radially stratified vertical magnetic field with $B_{\rm R}$=$B_\phi$=0 and

$$B_{\rm z} = \frac{R_0^{5/2}}{\sqrt{\beta}(R_0^2 + R^2)^{5/4}} \ . \tag{6.4}$$

The plasma beta parameter $\beta$ is the ratio of the thermal to the magnetic pressure at $z$=0, and we choose it to be of the order of unity, with the exact value $\beta$=1.67

### 6.1.5 Magnetic diffusivity

In comparison to the pure jet simulations presented in Chapter 4, which have been calculated applying an uniform distribution for the (turbulent) magnetic diffusivity, we now have to consider a much stronger (few orders of magnitude) diffusivity in the highly turbulent disk, compared to the disk corona. The profile of the diffusivity is

$$\eta = \alpha u_{\rm A}(z=0) H \exp\left(-2\frac{z^2}{H^2}\right) \ . \tag{6.5}$$

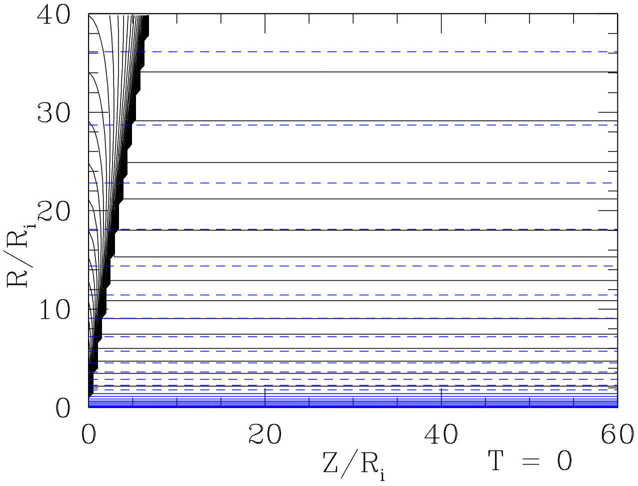

Figure 6.3: The distribution of the density and the magnetic field for the initial configuration. The *solid* lines denote 30 logarithmically spaced isocontours of density. The *dashed* lines denote 20 linearly spaced magnetic flux surfaces or, equivalently, the poloidal magnetic field lines.

The diffusivity vanishes outside the disk (i.e. everywhere in the disk corona), and varies in time with the equatorial Alfvén speed $u_{\rm A} = B/\sqrt{\rho}$. The free parameter $\alpha$ ($\alpha \leq$1, see §2.1.4) is set to $\alpha$=0.1, to ensure not too high value of the diffusivity in the disk. Plot of the diffusivity profile along the disk equatorial plane is shown in Fig.6.2.

## 6.2 Disk-jet connection

The time evolution of the disk-jet structure in our simulations is discussed in this section. Note that the simulations last for tens of rotations of the inner disk radius. Most of the previous simulations in the literature were substantially shorter, because of the problems in maintaining the disk dynamical equilibrium.

### 6.2.1 Initial configuration

The initial state in the computational box is shown in Fig. 6.3. As already mentioned, the initial corona in this setup is *not* in a hydrostatic equilibrium. Such a distribution without the disk or some mass inflow becomes unstable and disperses or collapses (towards the symmetry axis) fast. However, the time for a torsional Alfvén wave propagating from the disk to sweep through the computational box is shorter than the initial

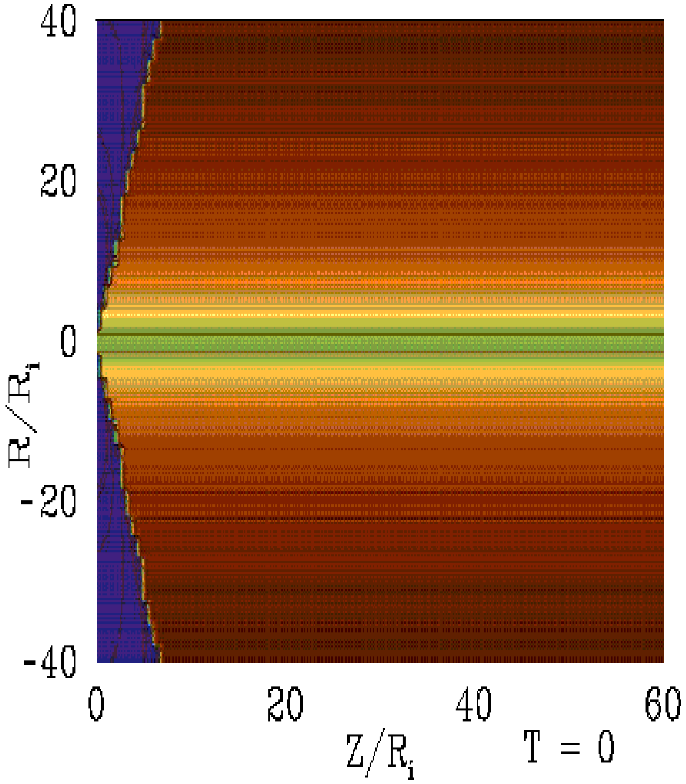

Figure 6.4: The initial setup with the density levels in a colour grading in the interval (1,$10^{-6}$). The denser levels are shown in the intensifying green colour component.

corona instability timescale (Mouschovias & Paleologou 1980). A new regime in the computational box is then dictated by the outflow, and not by the initial instabilities (Ouyed & Pudritz 1997b).

The density levels for our initial setup are shown in Fig. 6.4.

### 6.2.2 Jet launching

In the initial setup, with a *radially* inward velocity ($u_{\rm R}$<0), defined is an accretion flow. Also, for a parameter $m_{\rm S}$<1, an initial poloidal inflow occurs. To have the BP82 condition for the poloidal magnetic surfaces fulfilled (an angle between the poloidal magnetic surfaces and the disk surface to be smaller than 60°), this parameter can not be too small.

A non-vanishing resistivity is also required. This follows from the radial component of the magnetic induction equation (2.9) for a stationary case ($\partial/\partial t$=0). For a thin accretion disk, when $|u_{\rm z}| \ll |u_{\rm R}|$ and $|\partial B_{\rm z}/\partial R| \ll |\partial B_{\rm R}/\partial z|$ applies, only the part of the expression with the magnetic resistivity remains: $\eta\partial B_{\rm R}/\partial z \simeq -u_{\rm R}B_{\rm z}$. In the case of ideal MHD, when $\eta$=0, the matter infalling towards the disk centre could not cross the magnetic field lines and be lifted perpendicular to the disk surface, above the disk.

After a few rotations of the inner disk radius, an outflow forms. The launching is persistent, and it is limited only to the inner ($R$<15) portion of the disk. This is a result of the delicate balance of forces within the disk, where simultaneously with the ejection of matter, the disk itself must remain in an equilibrium. The total vertical force must be *positive* at the disk surface, and *negative* inside the disk, and most of the plasma should remain inside the disk. The mass ejected in the jet can therefore be only a small fraction of the disk mass.

A bow shock of the outflow propagates beyond the computational domain in a few tens of revolutions of the inner disk radius. However, the outflow is narrow enough that its collimation would be completed within our computational box. The density distribution in the outflow in our simulation is shown in Fig. 6.5.

We can compare this result to the numerical simulations of CK02[5]. They obtained a collimated outflow launched from the resistive accretion disk. The outflow, launching of which occurs without artificial inflow conditions, becomes collimated within the computational domain (Fig. 6.6). The launching in these simulations remains restricted to a segment of the physical domain within $R<20R_{\rm i}$. In the inner disk region, equipartition between thermal and magnetic pressure occurs, as the plasma $\beta$ and the angle of a magnetic field lines decrease for increasing radii. In their discussion, CK02 report a systematic larger jet-launching radial range for gradually extending radial box size. This indicates some influence from the open boundary.

When the jet becomes quasi-stationary, the outflow is well collimated. The angle $\Theta$ between the poloidal velocity and the axis of the jet is shown in Fig.6.7. High above the disk, but still in the computational box, this angle becomes small, less than 2°. In CK02 simulation this occured at times $t$>17, and in our at $t\gtrsim$150.

The poloidal magnetic field lines and the poloidal velocity vectors in our simulation at $t$=150 rotations of the inner disk radius, are presented in Fig.6.8. A caveat in these results is the position of the Alfvén surface, which seems to be positioned both at the disk surface and in a corona, probably because of a low resolution of the runs, or too large $\beta$ plasma and $m_{\rm s}$ parameters.

### 6.2.3 Disk-jet evolution

Occasional “outbursts” emerge irregularly from the disk in our simulations. The time scale of such events is few tens of rotations at $R_{\rm i}$. One of them is visible in Fig. 6.5, which is the snapshot of our simulation at t=150. These structures propagate outwards from the disk surface and exit the computational grid, not disturbing the overall collimated shape of the jet, formed after about hundred rotations at the inner disk radius. The radius of the collimated outflow in our simulation is $R\lesssim$20.

---

[5] Because of the different normalization, our time scale is for a factor ∼10 larger than in CK02.

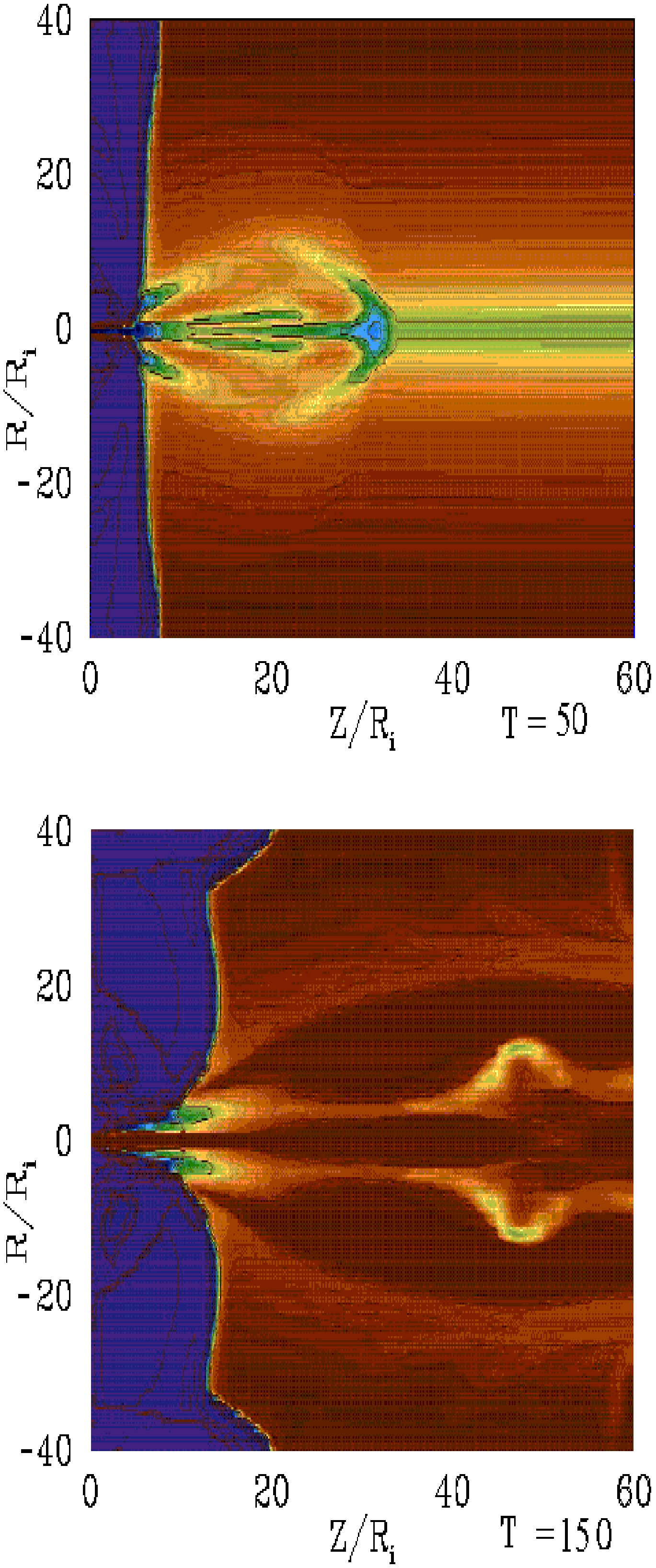

Figure 6.5: The distribution of the density in our simulation at $t$=50 (*top* panel) and at $t$=150 (*bottom* panel). The density levels are in a colour grading in the interval (1,$10^{-6}$). The denser levels are shown in the intensifying green colour component.

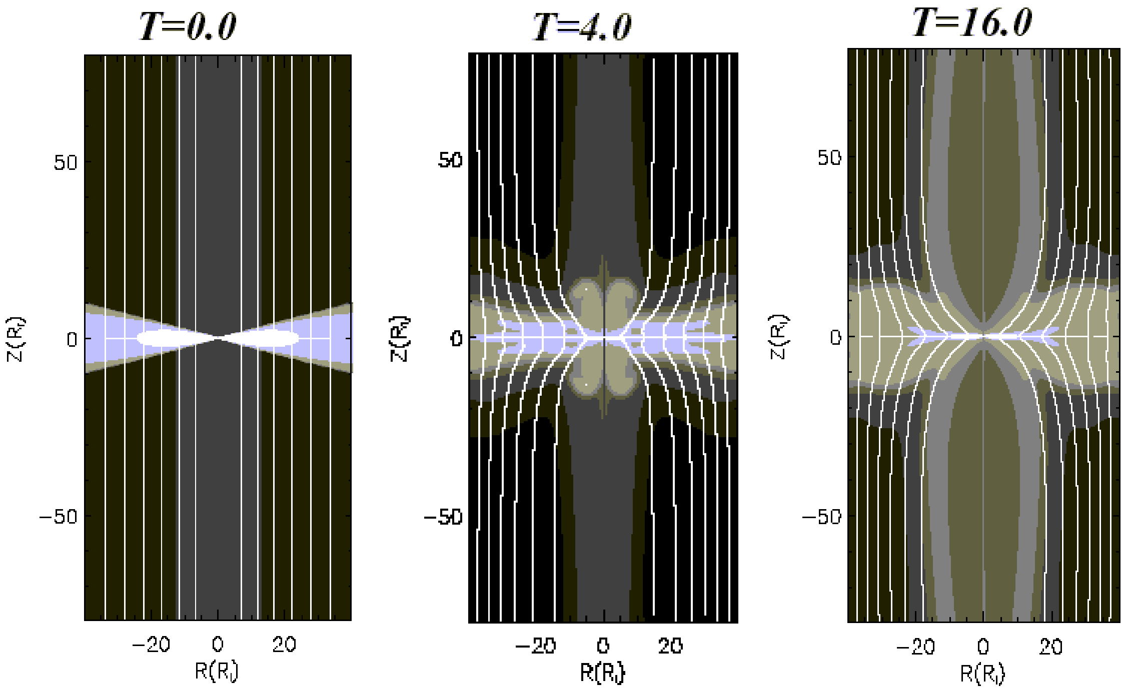

Figure 6.6: Thin accretion disk threaded by an initially decreasing vertical magnetic field. The density levels are in a gray scale (1,$10^{-6}$), where the denser levels are brighter. The white lines represent the poloidal magnetic field lines. Figure adopted from CK02, Fig. 2.

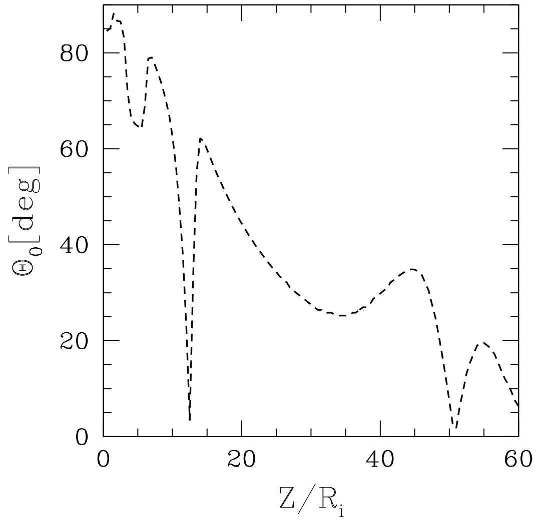

Figure 6.7: The angle between the poloidal velocity and the jet axis of symmetry at $t$=150. Slice in $z$ direction, at a given radius $R$=15. The outflow becomes well collimated inside our computational box.

After a hundred rotations, the disk piles-up by a factor two to three, compared to the initial height. The higher resolution runs are, naturally, much better in maintaining the disk equilibrium, but the machine time for the simulations increases rapidly.

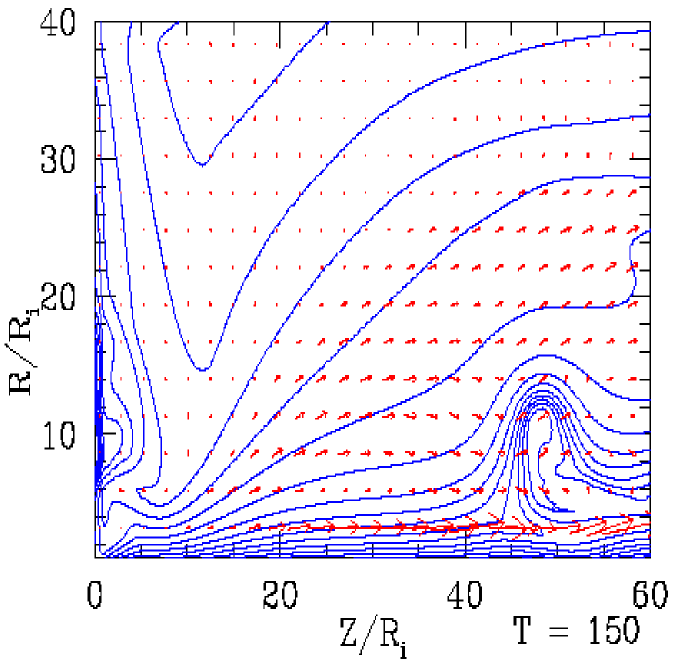

Figure 6.8: The poloidal magnetic field lines and the poloidal velocity vectors at $t$=150 in our simulation. The *solid* lines denote 20 linearly spaced magnetic flux surfaces or, equivalently, the poloidal magnetic field lines.

“Flaring” of the disk along the outer $R$-boundary at $t$>100 is one sign of disturbed equilibrium in the disk, probably because of too low resolution in the simulation. The inflow of matter into the disk from the outer part of the disk could also be the reason for such a “flaring”, if it is not matched well enough with the accretion rate in the disk.

In Fig. 6.9 we show one vertical slice of the density in $z$ direction, at a fixed radial distance $R$=15, and at $t$=150. In a disk corona the density of the matter is for a few orders of magnitude smaller than in the disk.

In the same figure presented is the jet terminal velocity, in the same slice and at the same time as for the density. Near the disk surface, the poloidal velocity changes sign. This is a consequence of the sign change of the magnetic torque $\boldsymbol{j}_{\rm p} \times \boldsymbol{B}_{\rm p}$ at these locations, which is a condition for the outflow acceleration. The terminal velocity of the outflow, which is equal to the escape velocity of the central object, is in our simulation of the order of Keplerian velocity at the inner disk radius.

In the same slice shown are also the magnetic field components (Fig.6.10). A magnetic field, which accelerates the matter in the outflow, also brakes azimuthally the matter inside the disk, by the magnetic torque, and therefore transfers the angular momentum of matter. The collimation of the flow in our model is due to magnetic tension, or the “hoop” stress, which is proportional to $B_\phi^2/R$, and is always directed toward the axis of the jet.

In Fig.6.10, shown is also a slice of the component of the Lorentz force along the jet

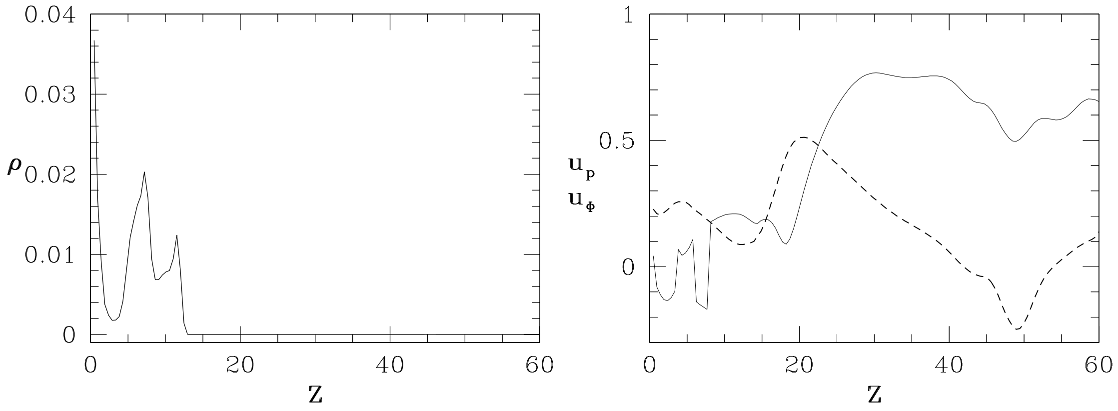

Figure 6.9: The density and the components of the velocity at $t$=150. Slice in $z$ direction, at a given radius $R$=15. The *solid* line denotes the poloidal velocity, and the *dashed* line denotes the toroidal velocity.

propagation at $t$=150. Inside the disk, the toroidal component of the Lorentz force $(\boldsymbol{j} \times \boldsymbol{B})_\phi$ is negative, and near the surface of the disk it becomes positive. This change of sign is a condition for a poloidal acceleration, which prevents the decreasing of velocity.

In our simulation, for a slice at $R\gtrsim$15, the toroidal component of the Lorentz force becomes *positive* inside the disk, and there is no launching any more. It is because of the vertical balance of the thermal and the magnetic pressure in the disk, which is a condition for the launching (Ferreira & Pelletier 1995).

In a presented setup the magnetic diffusivity is effective only inside the disk. With a minor change in the initial conditions, we performed the numerical simulations of the resistive accretion disk *and* resistive corona. The jet was affected in a way described in Chapter 4, i.e. for a more resistive corona the jet propagated more slowly.

## 6.3 Summary of the results

The numerical simulations for the setup with the turbulent, resistive thin accretion disk evolution included are performed, and the question of the jet launching from such a disk addressed. Only the presence of a large scale magnetic field is required as an initial condition. The diffusivity is effective only inside the disk.

Our results can be summarized as follows:

(1) For our model setup, a persistent outflow from the disk in equilibrium is formed.

(2) The launching of the outflow occurs from the inner ($R$<15) portion of the disk.

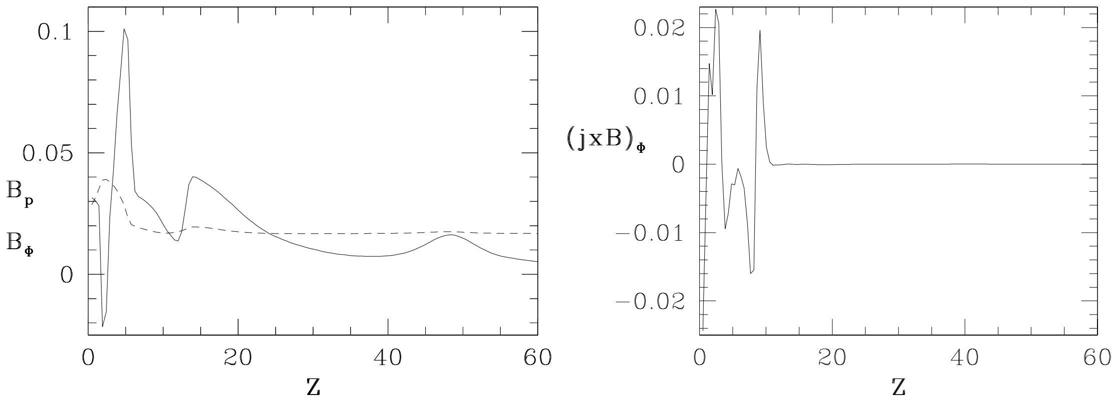

Figure 6.10: Vertical profiles of the magnetic field and the toroidal Lorentz force at a given radius $R$ and at *t*=150. *Left* panel: Components of the magnetic field; the *solid* line denotes the poloidal, and the *dashed* line denotes the toroidal component. Slice in $z$ direction, at $R$=15. *Right* panel: The toroidal component of the Lorentz force, $(\boldsymbol{j} \times \boldsymbol{B})_\phi$. Slice in $z$ direction, at $R$=5.

(3) The outflow results in a well collimated jet inside our computational box.

(4) The jet terminal velocity is of the order of Keplerian velocity at the inner disk radius.

(5) The quasi-stationary state of the outflow is reached after $t \sim 150$.

(6) The jet radius is $R_{\rm j} \lesssim 20 R_{\rm i}$.

The results summarized here indicate that in a presented scheme it is possible to obtain the quasi–stationary jets, consistent with the Ferreira (1997) self-similar solutions. The velocity, magnetic field and magnetic torque in our simulations comply with the requirements of the theory of axisymmetric, centrifugally driven disk wind.

However, the resolution in our simulations is rather low, and that is why we characterize our results as *preliminary*. Also, in three-dimensional simulations the jet becomes unstable for the super-Alfvénic speeds, subject to nonaxisymmetric Kelvin-Helmholz instability (Ouyed et al. 2003). Therefore, the conclusions (and precautions) concerning validity of two-dimensional simulations remain effective.

# Summary

In this thesis the MHD jet formation and the effects of magnetic diffusion on the formation of axisymmetric protostellar jets have been investigated in three different simulation sets. The time-dependent numerical simulations have been performed, using the ZEUS-3D code. The principal model set-up was for a jet propagation through the *resistive* disk corona of a central star surrounded by an accretion disk. In the second set of simulations we check (for the ideal MHD setup) the possibility of the jet collimation by the poloidal magnetic field only, and in the third set of simulations we include the disk in the resistive MHD simulations.

In the first step we investigated the resistive MHD simulations of jet formation, propagation and collimation with a disk as a boundary condition. Our initial setup has been for a force-free magnetic field in a hydrostatic corona, with the accretion disk included as a fixed boundary condition. For the disk to be evolved in time in our simulations it takes a considerably longer computation time, taking into account a much bigger diffusivity in the disk.

In the ideal MHD jet simulations it has been found that the disk outflow evolves into a *quasi-stationary* state after a few hundreds of disk revolutions (Ouyed & Pudritz, 1997). It is not at all obvious that the same should occur in the resistive MHD simulations. When this is the case, we can compare the results of the simulations with the stationary state computations.

On the global scale of our numerical simulations the jet bow shock advances slower through the initial hydrostatic corona for the resistive jets. However, the velocity of the matter inside the outflow is increasing with the increasing diffusivity, leaving the direction of the velocity vectors only slightly changed, when the poloidal magnetic field de-collimates increasingly.

As there exists a quasi-stationary state in our simulations for the resistive MHD jet, it is possible to develop the model which allows us to explain the jet decollimation and acceleration in the context of Lorentz forces. The *entire flow* along the jet axis is collimated by the perpendicular (to the poloidal magnetic field line) component of Lorentz force, and the parallel component accelerates the flow, increasingly with the increasing diffusivity (Fendt & Čemeljić 2002).

As a proper measure of the degree of collimation we suggest the ratio of the mass flux along and perpendicular to the jet axis. There exists a critical value for the magnetic diffusivity $\eta_{cr}$, when the mass flow becomes mostly radially directed.

In the second part of our simulations an another approach is investigated. It is generally believed that the toroidal component of the magnetic field provides substantial force for the collimation process in magnetically driven jets. However, in Spruit et al. (1997) it has been assumed that the collimation of the jet is due to the magnetic pressure of the poloidal magnetic field of the disk. In order to test this idea numerically, we performed the numerical simulations with the original, ideal MHD version of the ZEUS-3D code, setting the initial state by JETSET tool (Jørgensen et al. 2001). The toroidal component of the magnetic field has been artificially set to vanish in the simulations, and the effects of the poloidal component of the magnetic field on the outflow have been investigated. Physically, this situation is equivalent to an infinite anisotropic diffusivity in the direction perpendicular to the disk surface (Ferreira & Pelletier 1995).

In all the investigated configurations, from the straight lines of the magnetic field, perpendicular to the disk surface, via the open (split–monopole) to the dipole–like magnetic field lines, the accelerated *and* collimated flow for the *cold* corona simulations in the absence of the toroidal magnetic field has not been found.

The opposite has been found for the *hot* corona simulations, when access to an additional source of energy is required in the disk corona. In our setup, these can result in a collimated, accelerated outflow even in the absence of the toroidal magnetic field. The agreement has been stated with Spruit et al. (1997) analytically derived condition, that for the initial magnetic field of the disk given with $B \approx R^{-\mu}$, with $\mu \sim$1.3, such outflows could teminate as collimated and accelerated.

The next step in the numerical simulations of jet formation is the inclusion of the disk structure in the simulation. The self-similar solutions for a magnetized accretion disk driving jet have been given in Ferreira (1997), and the first simulations of a resistive accretion disk launching nontransient, ideal MHD jet have been carried out by Casse & Keppens (2002). Also in the third set of numerical simulations presented in this thesis, the disk-jet transition has been investigated with the disk evolved in time together with the outflow. Our results resemble the results of Casse & Keppens from the paper mentioned above.

The presence of a large scale magnetic field has been the only requirement as an initial condition, and we choose it as a radially stratified vertical magnetic field. The magnetic diffusivity profile has been taken with a Gaussian profile, vanishing outside the disk. The vertical disk equilibrium and the Keplerian rotation impose the constraint for the radial density profile. A radial equilibrium of the disk is ensured for a sub-Keplerian rotation profile, and the initial poloidal velocity profile has been defined solely by the accretion rate in the disk, i.e. with an inward radial velocity at the outer radial boundary of the disk.

The preliminary results obtained in these simulations show that the jet is launched from the inner portion of the disk (Čemeljić & Fendt 2004). The outflow becomes well collimated inside our computational box, and the quasi-stationary state of the outflow is reached after approximately 150 rotations of the disk at the inner disk radius. The jet radius is about $20R_\mathrm{i}$.

However, it is known that in three-dimensional simulations the jet becomes unstable for super-Alfvénic speeds (Ouyed et al. 2003), as it is subject to nonaxisymmetric Kelvin-Helmholz instabilities. Therefore, the precautions concerning validity of two-dimensional simulations remain effective.

Some of the numerical simulations presented in this thesis can be viewed at the
www.aip.de/∼miki/jetovi.html.

# Appendix

## A.1 Numerical Tests

As we have introduced the effect of physical magnetic diffusivity into the ideal MHD ZEUS–3D code, careful tests were necessary to prove our implementation. In particular we checked the time scales introduced by magnetic diffusion and the behavior along the boundaries. The boundary conditions for an axisymmetric jet ("outflow", "inflow "and "reflecting") are quite different from what is e.g. needed in box simulations used for other scientific questions.

We defined two numerical tests for our diffusive code. In both cases the code basically solves the diffusion equation. We obtained this limit by setting the initial density in the simulation to arbitrarily large values (here the normalized $\rho \simeq 10^9$) effectively reducing any fluid motions in our simulations. The first test example is the analytical solution of the diffusion equation in Cartesian coordinates, the second example an axisymmetric torus of purely toroidal magnetic field in cylindrical coordinates.

### A.1.1 Analytical solution to the diffusion equation

In Cartesian coordinates $(x, y, z)$ the solution of the one dimensional diffusion equation for infinite space is

$$B_z(y,t) = \frac{1}{\sqrt{t}} \exp\left(-\frac{(y-y_0)^2}{4\eta t}\right) , \tag{6.6}$$

with the magnetic diffusivity $\eta = c^2/(4\pi\sigma)$.

As a test for our code, we choose as initial condition the magnetic field $B_z(x,y) = B_z(y)$ for a certain time $t = t_0$ from Eq. (A.1). For the two-dimensional numerical grid we prescribe "free" (i.e. outflow) boundary conditions in $x$-direction and a time-varying field for the boundaries in $y$-direction.

Figure A.1 show the result of our simulations for the time steps $t = t_0 \Delta t$ ($\Delta t = 0.1, 0.2, 0.3, 0.4$) for a magnetic diffusivity $\eta = 1.0$ in comparison with the analytical results. As result, we obtain a perfect agreement between the numerical simulation and the analytical solution.

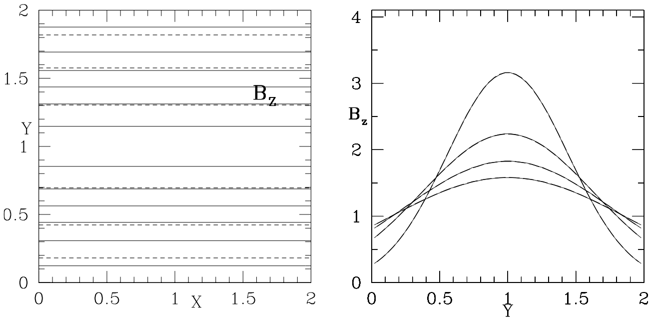

Figure A.1: Numerical test of magnetic diffusion. Grid size $50 \times 50$ elements for a normalized physical grid $2.0 \times 2.0$. *Left* Isocontours of the magnetic field strength $B_z(x, y)$ (normalized units) for different time steps $t = t_0 + \Delta t$, $\Delta t = 0.0$ (*solid line*), $\Delta t = 0.1$ (*dashed line*). *Right* Normalized intensity profile of the magnetic field strength across the two-dimensional box along $x = 1$ for different time steps $t = t_0 + \Delta t$ with $\Delta t = 0.0, 0.1, 0.2, 0.3$ (*top* to *bottom* curve). Comparison between the analytical solution *solid lines* and the numerical simulation (*dashed lines*).

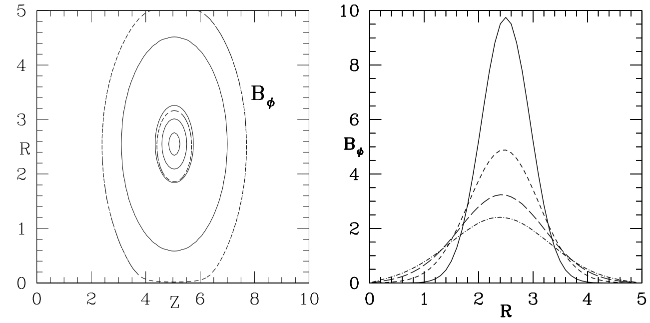

Figure A.2: Numerical test of magnetic diffusion in cylindrical coordinates. Grid size $100 \times 50$ elements for a normalized physical grid $10.0 \times 5.0$. *Left* Isocontours of the toroidal magnetic field strength for different time steps $t = t_0 + \Delta t$, $\Delta t = 0.0$ (*solid line*), $\Delta t = 0.1$ (*dashed line*). *Right* Normalized intensity profile of the magnetic field strength across the two-dimensional box along $z = 5$ for different time steps $t = t_0 + \Delta t$ with $\Delta t = 0.0, 0.1, 0.2, 0.3$ (*top* to *bottom* curve).

### A.1.2 Toroidal field torus

Here, our aim is to check, how our code treats magnetic diffusion in cylindrical coordinates, along the outflow boundary in $r$-direction and along the symmetry axis. As initial condition, we define a torus of toroidal magnetic field

$$B_\varphi(r, z, t_0 = 0.1) = \frac{1}{t_0} \exp\left( - \frac{(r - r_0)^2 + (z - z_0)^2}{4 \eta t_0} \right) . \qquad (6.7)$$

Figure A.2 show the result of our simulations for the time steps $t = t_0 \Delta t$ ($\Delta t = 0.1, 0.2, 0.3, 0.4$) for a magnetic diffusivity $\eta = 1.0$ in comparison with the analytical results. The simulation shows how the peak of the field distribution moves slightly inwards from its initial central position as the field diffuses. Note that as the field diffuses outwards the volume over which the toroidal field is distributed increases. Therefore the decrease in field strength in outward direction. Along the symmetry axis the field strength remains zero, whereas the field strength along the outflow boundaries increases. No boundary condition is prescribed here.

Although there is no analytical solution to compare with, this simulation gives again convincing evidence that we properly incorporated the magnetic diffusion in the ZEUS-3D code.

# Bibliography

André P., Phillips R.B., Lestrade J.F., Klein K.L., 1991, *Direct VLBI detection of the magnetosphere surrounding the young star S1 in Rho Ophiuchi*, ApJ **376**, 630

Ambartsumian V.A., 1954, Comm. Burakan Obs. No. 13

Ambartsumian V.A., 1957, in IAU Symp. No.3, ed. G.H. Herbig, Cambridge Univ. press, p.177

Balbus S.A., Hawley J.F., 1991, *A powerful local shear instability in weakly magnetized disks. I - Linear analysis. II - Nonlinear evolution*, ApJ **376**, 214

Bally J., Devine D., 1994, *A parsec-scale 'superjet' and quasi-periodic structure in the HH 34 outflow?*, ApJ **428**, 65

Bateman G., 1980, *MHD Instabilities*, Cambridge, MIT Press

Bell A.R., Lucek S.G., 1995, *Magnetohydrodynamic jet formation*, MNRAS **277**, 1327

Blandford R.D., Rees M.J., 1974, *A 'twin-exhaust' model for double radio sources*, MNRAS **169**, 395

Blandford R.D., Znajek R.L., 1977, *Electromagnetic extraction of energy from Kerr black holes*, MNRAS **179**, 433

Blandford R.D., Payne D.G., 1982, *Hydromagnetic flows from accretion discs and the production of radio jets*, MNRAS **199**, 883 (BP82)

Blandford R.D., 1993, *Black Holes, Accretion Disks, and Relativistic Jets in Active Galactic Nuclei*, In: Relativistic Astrophysics and Particle Cosmology, Akerlof C.W., Srednicki M.A. (eds.), Annals of the New York Academy of Sciences, New York, New York Academy of Sciences, **688**, 311

Blondin J.M., Königl A., Fryxell B.A., 1989, *Herbig-Haro objects as the heads of radiative jets*, ApJ **337**, 37

Bond H.E., Livio M., 1990, *Morphologies of planetary nebulae ejected by close-binary nuclei*, ApJ **355**, 568

Brandenburg A., Nordlund Å., Stein R.F.,Torkelsson U., 1995, *Dynamo-generated Turbulence and Large-Scale Magnetic Fields in a Keplerian Shear Flow*, ApJ **446**, 741

Bridle A.H., Perley R.A., 1984, *Extragalactic Radio Jets*, ARA&A **22**, 319

Burgarela D., Paresce F., 1992, *The structure of the inner arcsecond of R Aquarii observed with the Hubble Space Telescope*, ApJ **389**, L29

Burnham S.W., 1890, *Note on Hind's Variable Nebula in Taurus*, MNRAS **51**, 94

Burnham S.W., 1894, Pub. Lick Obs. **2**, 175

Cabrit S., Edwards S., Strom S.E., Strom K.M., 1990, *Forbidden-line emission and infrared excesses in T Tauri stars - Evidence for accretion-driven mass loss?*, ApJ **354**, 687

Cabrit S., André P., 1991, *An observational connection between circumstellar disk mass and molecular outflows*, ApJ **379**, L25

Camenzind M., 1986, *Centrifugally driven MHD-winds in active galactic nuclei*, A&A **156**, 137

Camenzind M., 1990, *Magnetized disk-winds and the origin of bipolar outflows*, RvMA **3**, 234

Campbell C., G., 1997, *Magnetohydrodynamics in binary stars*, Astrophysics and Space Science Library, Vol 216, Kluwer Academic Publishers, Dordrecht

Canto J., Tenorio-Tagle G., Różyczka M., 1988, *The formation of interstellar jets by the convergence of supersonic conical flows*, A&A **192**, 287

Casse F., Ferreira J., 2000a, *Magnetized accretion-ejection structures. IV. Magnetically-driven jets from resistive, viscous, Keplerian discs*, A&A **353**, 1115

Casse F., Ferreira J., 2000b, *Magnetized accretion-ejection structures. V. Effects of entropy generation inside the disc*, A&A **361**, 1178

Casse F., Keppens R., 2002, *Magnetized Accretion-Ejection Structures: 2.5-dimensional Magnetohydrodynamic Simulations of Continuous Ideal Jet Launching from Resistive Accretion Disks*, ApJ **581**, 988

Casse F., Keppens R., 2003, *Radiatively inefficient MHD Accretion-Ejection Structures*, ApJ, in press, astro-ph/0310322

Čemeljić M., Fendt Ch., 2004, *Launching of resistive magnetic protostellar jets*, Stars as Suns: Activity, Evolution and Planets, eds. A.K. Dupree A.K., Benz A., IAU Symposium no. 219 Proceedings, in press, astro-ph/0311057

Chandrasekhar S., 1956, *Axisymmetric Magnetic Fields and Fluid Motions*, ApJ **124**, 232

Chiueh T., Li Z.-Y., Begelman M.C.S., 1991, *Asymptotic structure of hydromagnetically driven relativistic winds*, ApJ **377**, 462

Clarke D.A., Norman M.L., Fiedler R.A., 1994, *ZEUS-3D User Manual*, http://zeus.ncsa.uiuc.edu:8080/lca/zeus3d/zeus32.ps

Contopoulos J., 1994, *Magnetically driven relativistic jets and winds: exact solutions*, ApJ **432**, 508

Contopoulos J., 1995a, *Force-free Self-similar Magnetically Driven Relativistic Jets*, ApJ **446**, 67

Contopoulos J., 1995b, *A Simple Type of Magnetically Driven Jets: an Astrophysical Plasma*

*Gun*, ApJ **450**, 616

Courant R., Friedrichs K.O., 1948, *Supersonic flow and shock waves*, Pure and Applied Mathematics, New York, Interscience

Crampton D., Hutchings J.B., Cowley A.P., Schmidtke P.C., McGrath T.K., O'Donoghue D., Harrop-Allin M. K., 1996, *The Large Magellanic Cloud Supersoft X-Ray Binary RX J0513.9-6951*, ApJ **456**, 320

Cudworth K.M., Herbig G., 1979, *Two large-proper-motion Herbig-Haro objects*, AJ **84**, 548

Curtis H.D., 1918, *The planetary nebulae*, Publ. Lick Observatories **13**, 55

DeCampli W.M., 1981, *T Tauri winds*, ApJ **244**, 124

Dewar R.L., 1970, *Interaction Between Hydromagnetic Waves and a Time-Dependent Inhomogeneous Medium*, Phys. Fluids **13**, 2710

Dopita M.A., Evans I., Schwartz R.D., 1982, *Herbig-Haro Objects 46 and 47 - Evidence for bipolar ejection from a young star*, ApJ **263**, L73-L77

Dopita A., 1978, *The Herbig-Haro objects in the GUM Nebula*, A&A **63**, 237

Dopita A., 2002, *Spectral Signatures of Jet-Driven Shocks in Active Galactic Nuclei*, In: Emission Lines From Jet Rows, eds. R.J. Henney, W. Steffen, A.C. Raga and L. Binette, RevMexAA (Serie de Conferencias) **13**, 177

Edwards S., Cabrit S., Strom S.E., Heyer I., Strom K.M., Anderson E., 1987, *Forbidden line and H-alpha profiles in T Tauri star spectra - A probe of anisotropic mass outflows and circumstellar disks*, ApJ, **321**, 473

Edwards S., Ray T., Mundt R., 1993, *Energetic mass outflows from young stars*, In: Protostars and planets III, eds. E. Levy & J.C. Lunine, Tucson, Univ. of Arizona Press), p. 567

Eikenberry S.S., Matthews K., Morgan E.H., Remillard R.A., Nelson R.W., 1998, *Evidence for a Disk-Jet Interaction in the Microquasar GRS 1915+105*, ApJ, **494**, L61

Eislöffel J., Mundt R., 1997, *Parsec-Scale Jets From Young Stars*, AJ, **114**, 280

Eichler D., 1993, *Magnetic Confinement of Jets*, ApJ, **419**, 111

Evans C.R., Hawley J.F., 1988, *Simulation of magnetohydrodynamic flows - A constrained transport method*, ApJ, **332**, 659

Fender R. P., Pooley G.G., Brocksopp C., Newell S.J., 1997, *Rapid infrared flares in GRS 1915+105: evidence for infrared synchrotron emission*, MNRAS **290**, L65

Fendt Ch., Elstner D., 2000, *Long-term evolution of a dipole type magnetosphere interacting with an accretion disk. II. Transition into a quasi-stationary spherically radial outflow*, A&A **363**, 208 (FE00)

Fendt Ch., Čemeljić M., 2002, *Formation of protostellar jets - effects of magnetic diffusion*, A&A **395**, 1045 (FC02)

Ferrari A, Melrose D.B., 1997, *Particle acceleration and energy spectra in extragalactic radiosources*, Vistas in Astronomy **41**, 259

Ferraro V.C.A, 1937, *The non-uniform rotation of the Sun and its magnetic field*, MNRAS **97**, 458

Ferreira J., Pelletier G., 1993a, *Magnetized accretion-ejection structures. I. General statements*, A&A **276**, 625

Ferreira J., Pelletier G., 1993b, *Magnetized accretion-ejection structures. II. Magnetic channeling around compact objects*, A&A **276**, 637

Ferreira J., Pelletier G., 1995, *Magnetized accretion-ejection structures. III. Stellar and extragalactic jets as weakly dissipative disk outflows*, A&A **295**, 807

Ferreira J., 1997, *Magnetically-driven jets from Keplerian accretion discs*, A&A **319**, 340

Fleming T.P., Stone J.M., Hawley J.F., 2000, *The Effects of Resistivity on the Nonlinear Stage of the Magnetorotational Instability in Accretion Disks*, ApJ **530**, 464

Frank J., King A.R., Raine D.J., 1985, *Accretion Power in Astrophysics*, Cambridge Univ. Press

Frank A., Mellema G., 1996, *Hydrodynamical Models of Outflow Collimation in Young Stellar Objects*, ApJ **472**, 684

Frank A., Gardiner T.A., Delemarter G., Lery T., Betti R., 1999, *Ambipolar Diffusion in Young Stellar Object Jets*, ApJ **524**, 947

Gammie C.F., Balbus S.A., 1994, *Quasi-Global Linear Analysis of a Magnetized Disc*, MNRAS **270**, 138

Gilham S., 1981, *Scale-free axisymmetric accretion with weak viscosity*, MNRAS **195**, 755

Greiner J., Morgan E.H., Remillard R.A., 1996, *Rossi X-Ray Timing Explorer Observations of GRS 1915+105*, ApJ **473**, L107

Goodson A.P., Winglee R.M., Böhm K.-H., 1997, *Time-dependent Accretion by Magnetic Young Stellar Objects as a Launching Mechanism for Stellar Jets*, ApJ **489**, 199

Goodson A.P., Böhm K.-H., Winglee R.M., 1999, *Jets from Accreting Magnetic Young Stellar Objects. I. Comparison of Observations and High-Resolution Simulation Results*, ApJ **524**, 142

Goodson A.P., Winglee R.M., 1999, *Jets from Accreting Magnetic Young Stellar Objects. II. Mechanism Physics*, ApJ **524**, 159

Haro G., 1952, *Herbig's Nebulous Objects Near NGC 1999*, ApJ **115**, 572

Haro G., 1953, *H$\alpha$; Emission Stars and Peculiar Objects in the Orion Nebula*, ApJ **117**, 73

Hartigan P., Morse J.A., Raymond J, 1994, *Mass-loss rates, ionization fractions, shock velocities, and magnetic fields of stellar jets*, ApJ **436**, 125

Hasinger G., 1994, *Supersoft X-Ray Sources*, RvMA **7**, 129

Hawley J.F., 1995, *Local Three-dimensional Magnetohydrodynamic Simulations of Accretion Disks*, ApJ **440**, 742

Hawley J.F., Stone J.M., 1995, *MOCCT: A numerical technique for astrophysical MHD*, CoPhC **89**, 127

Hayashi M.R., Shibata K., Matsumoto R., 1996, *X-Ray Flares and Mass Outflows Driven by Magnetic Interaction between a Protostar and Its Surrounding Disk* ApJ **468**, L37

Heathcote S., Reipurth B., 1992, *Kinematics and evolution of the HH 34 complex*, AJ, **104**, 2193

Henriksen R.N., Rayburn D.R., 1971, *Relativistic stellar wind theory: 'Near'zone solutions*, MNRAS, **152**, 353

Herbig G.H., 1950, *The Spectrum of the Nebulosity Surrounding T Tauri*, ApJ, **111**, 11

Herbig G.H., 1951, *The Spectra of Two Nebulous Objects Near NGC 1999*, ApJ, **113**, 697

Herbig G.H., 1974, Lick Obs. Bull. No. 658

Herbig G.H., Jones B.F., 1981, *Large proper motions of the Herbig-Haro objects HH 1 and HH 2*, AJ, **86**, 1232

Heyvaerts J., Norman C.A., 1989, *The collimation of magnetized winds*, ApJ, **347**, 1055

Hollenbach D.J., 1997, *The Physics of Molecular Shocks in YSO Outflows*, In: Herbig-Haro Flows and the Birth of Stars; IAU Symposium No. 182, Eds. Bo Reipurth and Claude Bertout, Kluwer Academic Publishers, 1997 IAUS, **182**, 181

Jørgensen M.A.S.G., Ouyed R., Christensen M., 2001, *Initial magnetic field configurations for 3-dimensional simulations of astrophysical jets*, A&A, **379**, 1170

Junor W., Biretta J.A. J., 1995, *The radio jet in 3C274 at 0.01 PC resolution*, AJ, **109**, 500

Kahabka P., Trumper J., 1996, *Supersoft ROSAT Sources in the Galaxies*, In: van den Heuvel E.P.J., van Paradijs J. (eds.), IAU symposium 165 proceedings, Kluwer Academic Publishers, Dordrecht, IAUS **165**, 425

Kato S.X., Kudoh T., Shibata K., 2002, *2.5-dimensional Nonsteady Magnetohydrodynamic Simulations of Magnetically Driven Jets from Geometrically Thin Disks*, ApJ, **565**, 1035

Kepner J., Hartigan P., Yang C., 1993, *Hubble Space Telescope Images of the Subarcsecond Jet in DG Tauri*, ApJ, **415**, L119

Königl A., 1986, *Stellar and galactic jets - Theoretical issues*, Can. J. Phys., **64**, 362

Königl A., 1989, *Self-similar models of magnetized accretion disks*, ApJ, **342**, 208

Königl A., Ruden S.P., 1993, *Origin of outflows and winds*, In: Protostars and planets III, Levy E.H, Lunine J.I. (eds.), Univ. of Arizona Press, 641

Krasnolpolsky R., Li Z.-Y., Blandford R., 1999, *Magnetocentrifugal Launching of Jets from Accretion Disks. I. Cold Axisymmetric Flows*, ApJ, **526**, 631

Kudoh T., Shibata K., 1997, *Magnetically Driven Jets from Accretion Disks. II. Nonsteady Solutions and Comparison with Steady Solutions*, ApJ, **476**, 632

Kudoh T., Matsumoto R., Shibata K., 1998, *Magnetically Driven Jets from Accretion Disks.*

*III. 2.5-dimensional Nonsteady Simulations for Thick Disk Case*, ApJ, **508**, 186

Küker M., Henning T., Rüdiger G., 2003, *Magnetic star-disk coupling in classical T Tauri systems*, ApJ, **589**, 397

Kuwabara T., Shibata K., Kudoh T., Matsumoto R., 2000, *Resistive Magnetohydrodynamics of Jet Formation and Magnetically Driven Accretion*, PASJ, **52**, 1109

Lada C.J., 1985, *Cold outflows, energetic winds, and enigmatic jets around young stellar objects*, ARA&A, **23**, 267

Li Z.Y., Chiueh T., Begelman M.C., 1992, *Electromagnetically driven relativistic jets - A class of self-similar solutions*, ApJ **394**, 459

Li Z.Y., 1995, *Magnetohydrodynamic disk-wind connection: Self-similar solutions*, ApJ **444**, 848

Li Z.Y., Chevalier R.A., 2001, *Wind Interaction Models for the Afterglows of GRB 991208 and GRB 000301C*, ApJ **551**, 940

Livio M., Pringle J.E., 1996, *The Formation of Point-symmetric Nebulae*, ApJ **465**, L55

Livio M., 1997, *The Formation of Astrophysical Jets*, In: Accretion Phenomena and Related Outflows, eds. D. T. Wickramasinghe, G. V. Bicknell, and L. Ferrario, IAU Colloquium 163. ASP Conference Series, **121**, 845

Livio M., 1999, *Astrophysical jets: a phenomenological examination of acceleration and collimation*, PhR, **311**, 225

López R., Raga A., Riera A., Anglada G., Estalella R., 1995, *The extended structure of the HH 30 jet and other Herbig-Haro objects in the HL Tauri region*, MNRAS, **274**, L19

Lovelace R.V.E., 1976, *Dynamo model of double radio sources*, Nature, **262**, 649

Lovelace R.V.E., Mehanian C., Mobarry C.M., Sulkanen M.E., 1986, *Theory of axisymmetric magneto-hydrodynamic flows*, In: Magnetospheric phenomena in astrophysics, New York, American Institute of Physics, 291

Lovelace R.V.E., Wang J.C.L., Sulkanen M.E., 1987, *Self-collimated electromagnetic jets from magnetized accretion disks*, ApJ, **315**, 504

Lovelace R.V.E., Berk H.L., Contopoulos J., 1991, *Magnetically driven jets and winds*, ApJ, **379**, 696

Lüst R., Schlüter A., 1954, *Kraftfreie Magnetfelder. Mit 4 Textabbildungen*, Zeitschrift für Astrophysik, **34**, 263

Lynden-Bell D., Pringle J.E., 1974, *The evolution of viscous discs and the origin of the nebular variables.*, MNRAS, **168**, 603

Lynden-Bell D., 1978, *Gravity power*, PhyS, **17**, 185

Margon B., 1984, *Observations of SS 433*, ARA&A, **22**, 507

Martí J., Rodriguez L.F., Reipurth B., 1993, *HH 80-81: A Highly Collimated Herbig-Haro Complex Powered by a Massive Young Star*, ApJ, **416**, 208

Matsumoto R., Tajima T., 1995, *Magnetic viscosity by localized shear flow instability in magnetized accretion disks*, ApJ, **445**, 767

Matsumoto R., Uchida Y., Hirose S., Shibata K., Hayashi M.R., Ferrari A., Bodo G., Norman C., 1996, *Radio Jets and the Formation of Active Galaxies: Accretion Avalanches on the Torus by the Effect of a Large-Scale Magnetic Field*, ApJ, **461**, 115

McKee C.F., Hollenbach D.J., 1980, *Interstellar shock waves*, ARA&A, **18**, 219

Mestel L., 1961, *A note on equatorial acceleration in a magnetic star*, MNRAS, **122**, 473

Mestel L., 1968, *Magnetic braking by a stellar wind-I*, MNRAS, **138**, 359

Michel F.C., 1969, *Relativistic stellar-wind torques*, ApJ **158**, 727

Miller K.A., Stone J.M., 1997, *Magnetohydrodynamic Simulations of Stellar Magnetosphere–Accretion Disk Interaction*, ApJ, **489**, 890

Miller K.A., Stone J.M., 2000, *The Formation and Structure of a Strongly Magnetized Corona above a Weakly Magnetized Accretion Disk*, ApJ, **534**, 398

Mirabel I.F., Rodríguez L.F., 1995, *Superluminal motions in our Galaxy*, In: Böhringer H, Morfill G.E., Trümper (eds.), 17th Texas Symposium on Relativistic Astrophysics and Cosmology, Annals of the New York Academy of Science, **759**, 21

Morse J.A., Hartigan P., Cecil G., Raymond J.C.; Heathcote S., 1992, *The bow shock and Mach disk of HH 34*, ApJ, **399**, 231

Morse J.A., Hartigan P., Heathcote S., Raymond J.C., Cecil G., 1994, *Farby-Perot observations and new models of the HH 47A and HH 47D bow shocks*,ApJ, **425**, 738

Mouschovias T.Ch., Paleologou E.V., 1980, *Magnetic braking of an aligned rotator during star formation: an exact, time-dependent solution*, ApJ, **237**, 877

Mundt R., 1985, In: Protostars and Planets II, ed. D. Black. Tucson, Univ. Ariz. Press, 1985

Mundt R., Brugel E.W., Buehrke T., 1987, *Jets from young stars - CCD imaging, long-slit spectroscopy, and interpretation of existing data*, ApJ, **319**, 275

Mundt R., Bührke T., Solf J., Ray T.P., Raga A.C., 1990, *Optical jets and outflows in the HL Tauri region*, A& A, **232**, 37

Narayan R., Yi I., 1995, *Advection-dominated accretion: Self-similarity and bipolar outflows*, ApJ, **444**, 231

Norman M.L., Winkler K.-H.A., Smarr L., Smith M.D., 1982, *Structure and dynamics of supersonic jets*, A&A, **113**, 285

Ogura K., 1995, *Giant bow shock pairs associated with Herbig-haro jets*, Ap& SS, **224**, 151

Ouyed R., Pudritz R.E., 1997a, *Numerical simulations of astrophysical jets from Keplerian disks. I. Stationary models*, ApJ, **482**, 712 (OP97)

Ouyed R., Pudritz R.E., 1997b, *Numerical Simulations of Astrophysical Jets from Keplerian Disks. II. Episodic Outflows*, ApJ, **484**, 794

Ouyed R., Clarke D.E., Pudritz R.E., 2003, *Three-dimensional simulations of jets from Keplerian disks: Self-regulatory stability*, ApJ, **582**, 292

Padman R., Lasenby A.N., Green D.A., 1991, in P.A. Hughes (ed.), Beams and Jets in Astrophysics, Cambridge Univ. Press (Cambridge Astrophysics Series, **19**)

Pakull M.W., 1994, private communication, referenced in Livio (1999).

Pelletier G., Pudritz R.E., 1992, *Hydromagnetic disk winds in young stellar objects and active galactic nuclei*, ApJ, **394**, 117

Pitts E., Tayler R.J., 1985, *The adiabatic stability of stars containing magnetic fields. IV - The influence of rotation*, ApJ, **216**, 139

Poetzel R., Mundt R., Ray T.P., 1989, *Z CMa - A large-scale high velocity bipolar outflow traced by Herbig-Haro objects and a jet*, A&A, **224**, L13

Pollacco D.L., Bell S.A., 1996, private communication, cyted in Livio 1999.

Pooley G.G., Fender R.P., 1997, *The variable radio emission from GRS 1915+105*, MNRAS, **292**, 925

Pudritz R.E., Norman C.A., 1983, *Centrifugally driven winds from contracting molecular disks*, ApJ, **274**, 677

Pudritz R.E., 1985, *Star formation in rotating, magnetized molecular disks*, ApJ, **293**, 216

Pudritz R.E., Norman C.A., 1986, *Bipolar hydromagnetic winds from disks around protostellar objects*, ApJ, **301**, 571

Ray T.P., Mundt R., Dyson J.E., Falle S.A.E.G., Raga A.C., 1996, *HST observations of jets from young stars*,ApJ, **468**, L103

Ray T.P., Muxlow T.W.B., Axon D.J., Brown A., Corcoran D., Dyson R., Mundt R., 1996, *Large scale magnetic fields in the outflow from the young stellar object T Tauri S*,Nature, **385**, 415

Raga A.C., Canto J., Cabrit S., 1998, *Working surfaces in radiative, non-top hat jets*, A&A, **332**, 714

Reipurth B., Heathcote S., 1997, In: Herbig-Haro flows and the birth of low mass stars, IAU 182, eds. B. Reipurth & C. Bertout, 3

Reipurth B., Heathcote S., 1992, *Multiple bow shocks in the HH 34 system*, A&A, **257**, 693

Romanova M.M., Ustyugova G.V., Koldoba A.V., Chechetkin V.M., Lovelace R.V.E., 1997, *Formation of Stationary Magnetohydrodynamic Outflows from a Disk by Time-dependent Simulations*, ApJ, **482**, 708

Safier P.N., 1998, *A Critique of Current Magnetic-Accretion Models for Classical T Tauri Stars*, ApJ, **494**, 336

Safier P.N., 1999, *A Physical Limit to the Magnetic Fields of T Tauri Stars*, ApJ, **510**, L127

Sakurai T., 1985, *Magnetic stellar winds - A 2-D generalization of the Weber-Davis model*, A&A, **152**, 121

Schwartz R.D., 1975, *T Tauri Nebulae and Herbig-Haro Nebulae - Evidence for excitation by a strong stellar wind*, ApJ, **195**, 631

Shakura N.I., Sunyaev R.A., 1973, *Black holes in binary systems. Observational appearance*, A&A, **24**, 337

Shibata K., Uchida Y., 1985, *A magnetodynamic mechanism for the formation of astrophysical jets. I - Dynamical effects of the relaxation of nonlinear magnetic twists*, PASJ, **37**, 31

Shibata K., Uchida Y., 1986, *A magnetodynamic mechanism for the formation of astrophysical jets. II - Dynamical processes in the accretion of magnetized mass in rotation*, PASJ, **38**, 631

Shu F., Najita J., Ostriker E., Wilkin F., Ruden S., Lizano S., 1994, *Magnetocentrifugally driven flows from young stars and disks. 1: A generalized model*, ApJ, **429**, 781

Southwell K.A., Livio M., Charles P.A., O'Donoghue D., Sutherland W.J., 1996, *The Nature of the Supersoft X-Ray Source RX J0513-69*, ApJ, **470**, 1065

Spruit H.C., 1994, In: Cosmical Magnetism, Lynden-Bell D. (ed.), Kluwer, Dordrecht, p.33

Spruit H.C., Foglizzo T., Stehle R., 1997, *Collimation of magnetically driven jets from accretion discs*, MNRAS, **288**, 333 (S97)

Stanke T., McCaughrean M.J., Zinnecker H., 1999, *HH 46/47: Also a parsec scale flow*, A&A, **350**, L43

Stewart J.M., 1975, *The Hydrodynamics of Accretion Discs I*, A&A, **42**, 95

Stewart R.T., Caswell J.L., Haynes R.F., Nelson G.J., 1993, *Circinus X-1 - A runaway binary with curved radio jets*, MNRAS, **261**, 593

Stone J.M., Norman M.L., 1992a, *ZEUS-2D: A radiation magnetohydrodynamics code for astrophysical flows in two space dimensions. I - The hydrodynamic algorithms and tests.*, ApJS, **80**, 753

Stone J.M., Norman M.L., 1992b, *ZEUS-2D: A Radiation Magnetohydrodynamics Code for Astrophysical Flows in Two Space Dimensions. II. The Magnetohydrodynamic Algorithms and Tests.*, ApJS, **80**, 791

Stone J.M., Norman M.L., 1994a, *Numerical simulations of magnetic accretion disks*, ApJ, **433**, 746

Stone J.M., Norman M.L., 1994b, *Numerical simulations of protostellar jets with nonequilibrium cooling. 3: Three-dimensional results*, ApJ, **420**, 237

Strom J.M., van Paradijs J., van der Klis M., 1989, *Discovery of a double radio source associated with Cygnus X-3*, Nature, **337**, 234

Suttner G., Smith M.D., Yorke H.W., Zinnecker H., 1997, *Multi-dimensional numerical simulations of molecular jets*, A&A, **318**, 595

Tayler R.J., 1980, *The adiabatic stability of stars containing magnetic fields. IV - Mixed poloidal and toroidal fields*, MNRAS, **191**, 151

Tóth G., 1996, *A General Code for Modeling MHD Flows on Parallel Computers: Versatile Advection Code*, Astrophys. Lett., **34**, 245

Tout C.A., Pringle J.E., 1996, *Can a disc dynamo generate large-scale magnetic fields?*, MNRAS, **281**, 219

Trammell S.R, Goodrich R.W., 1996, *Hubble Space Telescope and Ground-based Imaging of the Bipolar Proto–Planetary Nebula M1-92: Evidence for a Collimated Outflow*, ApJ, **468**, L107

Uchida Y., Shibata K., 1985, *Magnetodynamical acceleration of CO and optical bipolar flows from the region of star formation*, PASJ, **37**, 515

Ustyugova G.V., Koldoba A.V., Romanova M.M., Chechetkin V.M., Lovelace R.V.E., 1995, *Magnetohydrodynamic simulations of outflows from accretion disks*, ApJ, **439**, L39

van Leer B., 1974, *Towards the ultimate conservative difference scheme: 2) monotonicity and conservation combined in a second-order scheme* J. Comput. Phys., **14**, 361

v.Rekowski M., Rüdiger G., Elstner D., 2000, *Structure and magnetic configurations of accretion disk-dynamo models*, A&A, **353**, 813

Wardle M., Königl A., 1993, *The structure of protostellar accretion disks and the origin of bipolar flows*, ApJ, **410**, 218

Wang J.C.L., Sulkanen M.E., Lovelace R.V.E., 1990, *Self-collimated electromagnetic jets from magnetized accretion disks - The even-symmetry case*, ApJ, **355**, 38

Wang J.C.L., Sulkanen M.E., Lovelace R.V.E., 1992, *Intrinsically asymmetric astrophysical jets*, ApJ, **390**, 46

# Acknowledgments

It is my pleasure to thank, once again, the people who made this work possible. Dr. Ch. Fendt and Prof. G. Rüdiger in the first place, for giving me the opportunity for it.

Ms. Andrea Trettin, the good spirit of haus B6, “Direktorengebaude” in AIP, and all the MHD group were always ready to help.

All the friends from the beautiful international room 21 in B6, and friends such as Christian Fendt, Rainer Arlt and Karl-Heinz Böning managed to transpose the time in AIP into a private dimension. Over three and half years they helped to make Potsdam one of “my” cities.

Friends and family from all around the world are an important part of my Universe. Without their support my playing the Science game would simply and interminably be a fail.